國立臺灣大學電機資訊學院光電工程學研究所

碩士論文

Graduate Institute of Photonics and Optoelectronics
College of Electrical Engineering and Computer Science
National Taiwan University

Master Thesis

應用於生物感測的表面電漿共振光纖探針之大量製作方法與其功效初步檢驗

Method for Mass Production of Surface Plasmon Resonance Fiber Probes for Label-Free Biosensing and Preliminary Test of Efficacy

鄭偉弘

Wei-Hong Jheng

指導教授：王倫 博士

Advisor: Lon A. Wang, Ph.D.

中華民國 105 年 1 月

January, 2016

誌謝

能完成這本論文與三年半的碩士學業，首先必須要感謝我的父母親，從小到大我的父母總是為了我不辭辛勞地打理我生活上的大小事，更讓我能無後顧之憂地專心於課業學習與實驗研究，感謝家人無悔的付出與精神支持。同時，我也要特別感謝王倫老師的指導，不僅是實驗上的建議與鼓勵包括了人生態度與對未來生涯的建議，我都會謹記在心。

在碩士班期間，我也認識了許多好夥伴，尤其子軒學長雖然畢業了，卻仍不厭其煩地解答我的問題，讓我更清楚知道各項實驗方法的原理;奕鈞學長也很樂於和我討論，在許多儀器的使用上也是很細心的教導;我的同期同學，方向，提供我大量製程方面的資訊與建議，使我的實驗製程能夠不斷修正錯誤並順利執行;學弟永泰、健甫、建霖更是實驗上的得力助手，常常幫忙樣品的準備與製作，協助實驗進行;另外，很榮幸能夠與黃念祖老師的實驗室合作，黃老師與兩位學生，筌凱與柏承，感謝他們願意花時間在我不熟悉的領域上幫助我許多。當然其他同學學弟們也幫忙了很多，像是繁雜的行政事務的處理，使我減輕不少負擔。很慶幸實驗室就像一個和樂的大家庭一樣，一塊打球談天，同甘共苦，一起成長。

最後感謝我的朋友們，因為你們的支持與鼓勵我才能撐到今天。很感謝老天爺的安排讓我在這輩子有機會與他們相遇，也希望未來我有能力能夠回報每個照顧我的人。

中文摘要

近來，在光纖端面製作次微米金屬結構並應用於表面電漿共振感測十分受到矚目，到目前為止已經發展了許多應用。因此，表面電漿共振光纖探針的需求與日俱增。其中表面電漿共振光纖探針的大量製作方法，是我們在本篇論文的主要焦點。

在此論文中，我們先介紹表面電漿共振光纖探針的製作過程。光纖探針的大量製作由光纖集束來實現，但由於此光纖集束即使在研磨後，仍然無法得到適合阻劑旋塗的平面，我們應用了奈米轉印技術來克服這項問題，此技術靠著材料之間表面能的差異來轉移金屬結構。我們選用聚二甲基矽氧烷做為轉印過程中印章的材料。在製作含有週期結構的印章的過程中，圖案的設計是藉由我們實驗室特有的雙光干涉曝光系統來完成。然而在將複製圖案至印章時，我們發現印章圖案在次微米的尺度下會有結構黏合的問題，此問題是因未固化的小分子而起並可由一些有機溶液或加長固化時間來減緩。將處理過後的印章鍍上金屬後，我們先於玻璃基板上進行奈米轉印並優化參數，而後才將優化的參數應用於光纖集束上。經由一系列量測結果顯示轉印結果良好，並且製作的結構為一三維結構。

為研究表面電漿共振光纖探針的光學特性，我們引用了 FDTD Solutions 與 Comsol 兩套商業軟體。模擬結果預測了反射與穿透頻譜的趨勢，同時表面電漿共振的位置與特性也被探討與證實。在外界環境的模擬當中發現到，穿透頻譜中的共振位置隨著環境改變而飄移，但另一方面，由於三維結構製作完整，反射頻譜並不隨環境而改變。在實驗量測的部分，頻譜量測結果與模擬結果有高度的相似性，證實了模擬模組的可靠性。藉由多重頻譜的重疊，暗示了利用奈米轉印技術達成表面電漿共振光纖探針大量製作的潛力。穿透頻譜在折射率感測方面亦有良好的表現，在共振位置之靈敏度為 265.7 nm/RIU。本論文最後則示範以該光纖探針進行牛血清蛋白之生物感測。

關鍵字：奈米轉印、光纖、表面電漿共振、光纖集束、大量製作

ABSTRACT

To date, fabricating metallic submicron structures on an optical fiber facet and applying to the surface plasmon resonance (SPR) sensing have drawn a lot of attentions, and have led to many applications. Therefore, the need of SPR fiber probes increases steadily. The method for mass production of the SPR fiber probes is the main focus of this work.

In this work, we first introduced the processes for the fabrication of the SPR fiber probes. The mass production of the probes was realized by fiber bundles. However, even if the bundle was polished, it could not generate a suitable plane for the spin-coating process of the resists. The nanotransfer printing (nTP) technique was adopted to overcome this problem. The technique relied on the different surface energies between the materials to transfer the metallic structures. PDMS was chosen as the material for the stamps used in nTP process. In the process of the fabrication of the stamps patterned with periodic structures, the patterns were designed by our unique two-beam interference lithography (IL) system. Nevertheless, it was found that the patterns on the stamps buckled up during the replication of the patterns to the stamps. The problem resulted from the uncured low molecular weight (LMW) chains, which could be removed by some organic solutions or a longer curing time. After a metallic layer was deposited on the treated stamps, we first applied the nTP process on the glass substrates and optimized the parameters. Then the optimized parameters were applied on the fiber bundles.

To study the optical characteristics of the SPR fiber probes, two commercial software, FDTD Solutions and Comsol, were used in this study. The simulated results

revealed the trends of the reflection and transmission spectra and the characteristics of SPR were also confirmed and discussed. In the simulation of different surroundings, the resonant position in the transmission spectrum shifted as the surroundings changed while the resonant position in the reflection spectrum remained still due to the structures' insensitivity to the surroundings. In experiment, the measured results showed very good consistency with the simulated, which verified the reliability of the models used in the simulation. Based on the spectra obtained from different probes, the potential for mass production of the SPR fiber probes is found by utilizing fiber bundles and nTP technique. The transmission spectra showed good performance in refractive index sensing with a sensitivity of 265.7 nm/RIU for the resonant position. Finally, biosensing of bovine serum albumin (BSA) with the SPR fiber probes was demonstrated.

Key words: nanotransfer printing, optical fiber, surface plasmon resonance, fiber bundle, mass production.

Statement of Contributions

1. Development of SPR fiber probes by applying nTP on the fiber bundle.
2. Calculation of phase-matching conditions for the excitation of surface plasmons by Matlab.
3. Establishment of simulation models

   RSoft: periodic gold structures on a glass substrate (2D)

   FDTD Solutions: periodic gold structures on a glass substrate (3D)

   Comsol: periodic gold structures on a glass substrate (2D & 3D), plasmonic nanolaser, optical modes in a silicon-cored fiber

CONTENTS

LIST OF FIGURES

LIST OF TABLES

Chapter 1 Introduction

1.1 Motivation

Sensors based on surface plasmon resonance (SPR) have been developed for different applications [1]. This can be attributed to the unique character of surface plasmons. To speak more clearly, surface plasmons strongly enhance the electric field near the surface of metal in a distance of tens of nanometers to hundreds of nanometers, depending on the material used and wavelength chosen to excite. Thus, by the enhancement of electric field in the short range, many SPR sensors are applied in molecule scale research such as surface-enhanced Raman scattering (SERS) sensors, biosensors and chemical sensors.

SPR sensor chips are usually fabricated on glass substrates and integrated with measurement systems. Surface plasmons can also be excited via thin metal films or metal structures on the sides or on the end faces of the optical fibers [2-4]. Such fiber sensors offer the advantages of system miniaturization, optical alignment-free and remote sensing. The real SPR sensor based on fiber was first proposed in 1993 by Jorgenson and Yee [5]. The cladding layers of a multimode fiber were removed several millimeters in length. Then a 55 nm silver film was deposited symmetrically on the fiber core. Therefore, the Kretschmann configuration formed and the light reflected at the core-silver interface. Surface plasmon polariton (SPP) excitation took place at the silver-sensed medium interface (as depicted in Fig. 1-1) so that the SPR fiber sensors was able to detect the change of the sensed medium such as air, water, high-fructose corn syrup solutions and so on [6].

Actually, it can be more flexible. Depositing metal films on the sides of fiber cores

is not the only way to develop SPR fiber sensors. Many patterning methods were proposed to fabricate periodic nanostructures or place metallic nanoparticles either on the sides or on the facets of fiber cores. Chen et al. produced the fiber probe modified with gold nanoparticles for surface-enhanced Raman scattering (SERS) detection. The tapered fiber was immersed in the gold solution and the gold nanoparticles were deposited on its tip surface through electrostatic self-assembly. As the laser light was injected into the fiber, the so called localized surface plasmons (LSPs) would be excited to detect the Raman spectra of the R6G solution [7].Ding et al. fabricated metallic gratings of period 511 nm on the sides of the tapered fiber by interference lithography (IL) and lift-off technique. They believed that the transmission dips with sensitivity 500 nm/RIU at the specific resonant wavelengths arised from the radiation coupling to surface plasmon modes by the metallic gratings [8]. Dhawan et al. employed focused ion beam (FIB) milling to develop a periodic nanohole array on the facet of a fiber, where the hole diameter and the period of the nanoholes were 200 nm and 600 nm respectively. The excitation of the propagating SPPs was achieved by the two-dimensional periodic structures on the continuous gold film and the sensitivity was measured 533 nm/RIU. Different shapes of the holes and other structures such as nanopillars were also applied in their researches [9, 10]. Scheerlinck et al. demonstrated how to use the nanoimprint lithography (NIL) to fabricate gold grating fiber probes. The SOI mold with grating patterns was prepared first and it was also treated with antistickting layer. Then, gold was deposited on the mold but the gold on top of the grating lines was removed by microcontact printing. Next, the fiber coated with UV-curable resist was brought close to the mold to fill the grating trenches. When the resist was cured by UV light, the fiber was lifted from the mold [11].

However, among those designs described above, grating-coupled SPR probes are

desired because the resonant wavelengths can be adjusted. On the other hand, to generate a large quantity of such probes is an issue. Generally, optical fibers are collected to form fiber bundles for processing [12-14]. Though electron-beam lithography (EBL) or FIB milling provides good definition of structures with a resolution of several nanometers, these techniques suffer from time consuming, high cost and low throughput. In the previous work, high-throughput and fast patterning of optical fiber ends by utilizing IL or NIL was studied [13, 14]. A series of process was demonstrated, including projecting interference patterns on the filmed PR, transferring patterns onto the fiber facets, and applying the optical fiber ends patterned with binary phase gratings (BPGs) to interference lithography. Nevertheless, spin coating of resists is needed in the processes of photolithography and NIL, but this process would hardly generate a planar resist film on the fiber bundle. Due to the different hardness of the fibers and the filling material among them, steps are formed at the fiber/filling material interfaces after polishing. Using acid-soluble glass as the filling material can overcome this problem. However, the optical fibers will be damaged during the removal process.

In this work, gold nanostructures are preferred due to their relatively low absorption in the infrared and inertness to oxidation when exposed in air. Besides, we adopt nanotransfer printing (nTP) technique which is a resist-free printing technique to produce optical fiber probes. It relies on the stamps with low surface energy for pattern transfer [15]. Zaumseil et al. and Menard et al. used this technique to generate two-dimensional (2D) or three-dimensional (3D) structures on the substrates. The procedures are depicted in Fig. 1-2 [16, 17]. For 2D structures (see Fig. 1-2 (a)), gold was first deposited on a PDMS stamp. Then the stamp was directly imprinted on the GaAs substrate coated with an adhesion layer and the 2D pattern was transferred. As for 3D structures (see Fig. 1-2 (b)), the procedures were similar to those in Fig. 1-2 (a) but

the 3D structures formed because of the sloping sidewalls of the stamps. We will show how to apply this technique to the fiber bundle and the technique has the potential for high-throughput and fast fabrication of SPR fiber probes.

As we mentioned at the beginning, the SPR fiber probes can be used as biosensors by modifying the metal surface with ligands and antibodies (or biotins) as depicted in Fig. 1-3. Camara et al. and Lin et al. demonstrated the biosensing of dengue virus NS1 antigens and streptavidins, respectively [18, 19]. We will also show the ability to do biosensing with our SPR fiber probes.

1.2 Organization of the Thesis

In Chapter 2, the fabrication processes of SPR fiber probes will be described in detail. The processes start from the fabrication of fiber bundles. Then, the fabrication of the *polydimethylsiloxane* (PDMS) stamps used in nTP by IL is introduced. It is also important to extract the low molecule weight (LMW) PDMS chains to maintain the pattern on the stamps. When the stamps are ready, the nTP process will be first tested on glass substrates to simulate the situation on fiber bundles and to optimize the parameters, including temperature, pressure, and time. The optimized parameters are used later in the nTP process of fiber bundles. Finally, separation of the fibers from the fiber bundle will be demonstrated. All final fabrication results of the metallic nanostructures are shown in the Section 2.4 and Section 2.5.

In Chapter 3, the theory of SPPs and methods of excitation will be introduced. Finite-difference time-domain (FDTD) method and finite element method (FEM) are used to predict the spectra of the SPR fiber probes and the distribution of the electric field near the gold nanostructures. Therefore, the theories and model buildings will also be described. The results of the simulation will be discussed in Section 3.5.

In Chapter 4, the characterization of the SPR fiber probes will be described, including the resonant wavelength and sensitivity in bulk refractive index after the set-up of the measurement system. Then the demonstration of biosensing with SPR fiber probes will be shown.

In Chapter 5, we will conclude these two fabrication procedures. The necessary improvements and the potential to the future development will also be described.

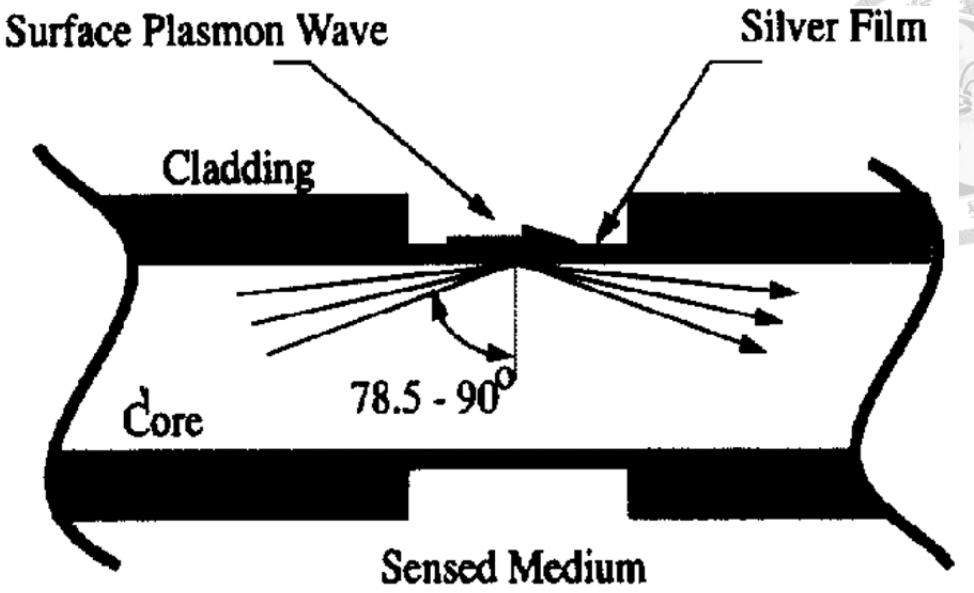

Fig. 1-1 The Kretschmann configuration [6].

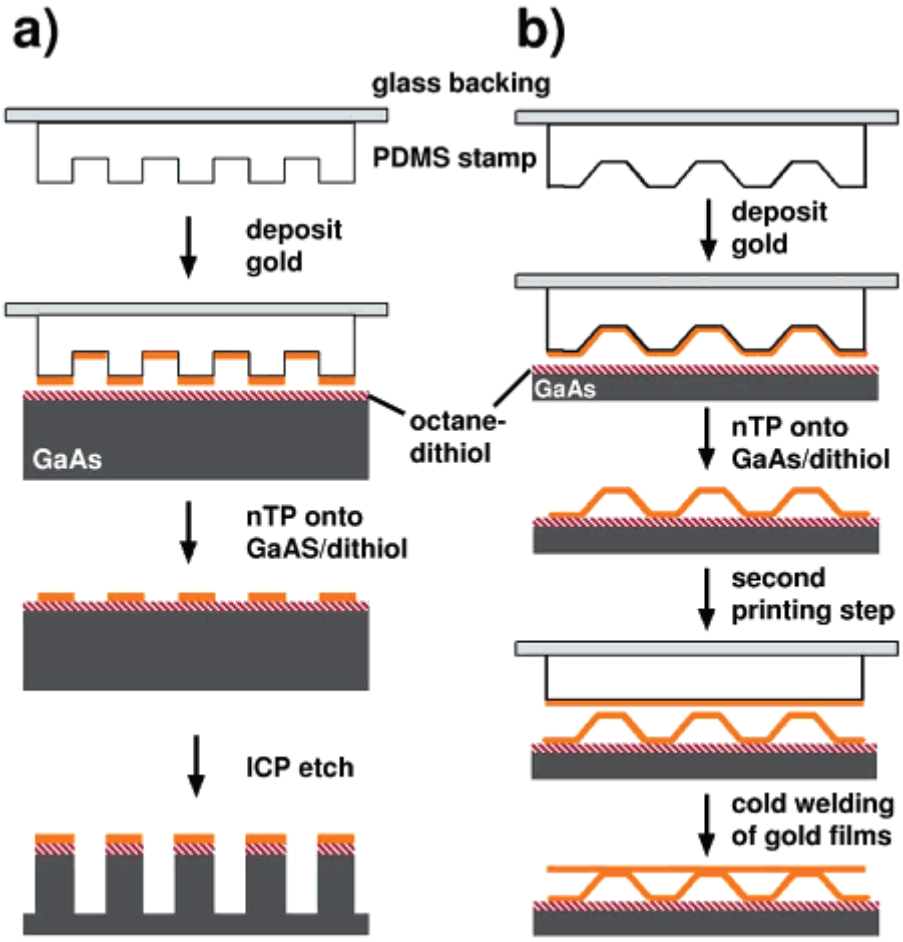

Fig. 1-2 Schematic illustration of routes to two-dimensional (a) or three-dimensional (b) structures by nanotransfer printing [16].

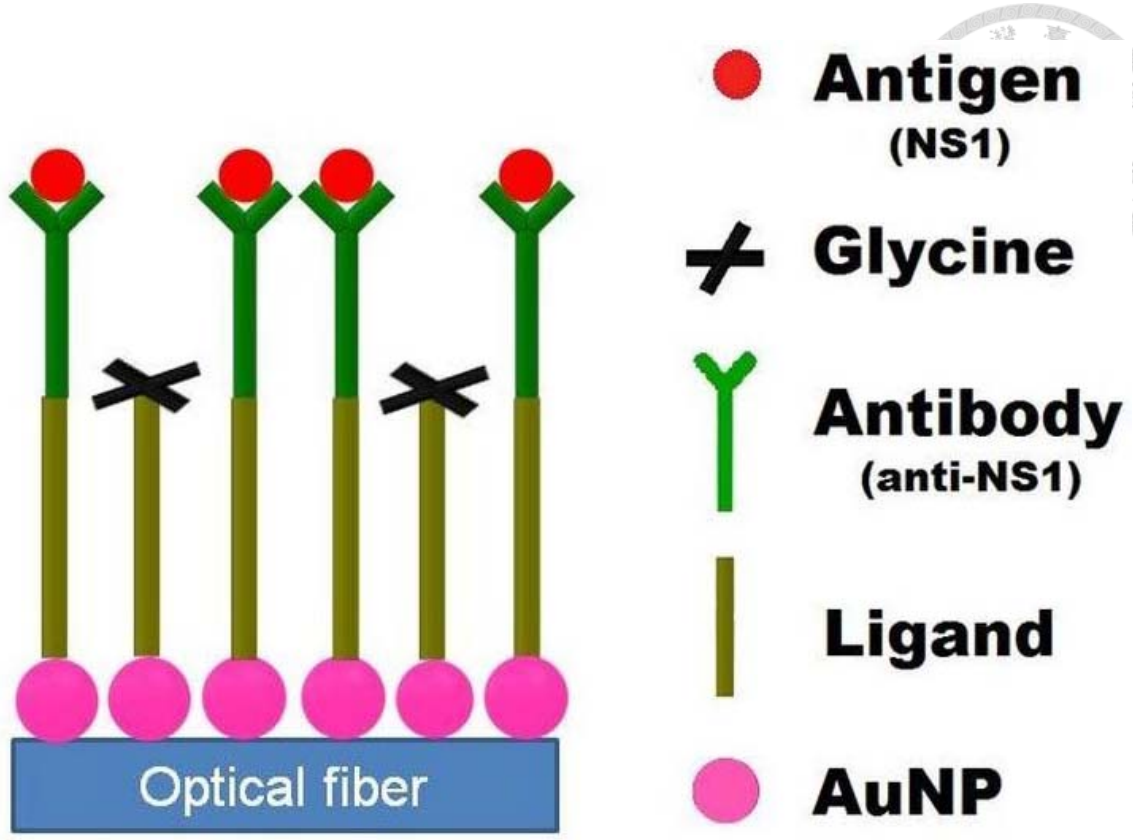

Fig. 1-3 Schematic diagram of the AuNPs modified with ligand, antibody (anti-NS1), block (Glycine) and adsorbed antigen (NS1) [18].

Chapter 2 Fabrication of Three-Dimensional Metallic Structures on Optical Fiber Ends by Nanotransfer Printing

2.1 Fabrication of fiber bundle

Inserting fibers into a silica capillary to increase the effective surface area for processing has been reported before [13, 14, 20]. And the fiber bundle has also been developed more than twenty years [21]. Generally, the purpose of making fiber bundle was for a flexible endoscope. The fiber bundle needed be separated in hydrochloric acid in gastric juice, so the adhesive was an acid-soluble glass. The acid-soluble glass was also an ideal adhesive for fabrication of fiber bundle in this work. To avoid damage in the processes of BPG fabrication on the top of a fiber bundle, we need such acid-soluble glass with enough hardness and high temperature and acid-alkali resistant. Because of the hardness close to that of fiber, one can get a relatively flat plane after polish. However, the acid-soluble glass was not easy to obtain and the fibers would be damaged during the separating process due to the ions in the acid-soluble glass diffused into the fibers at high temperature. Therefore, we chose easily accessible epoxy as adhesive, which was often applied for fabrication of fiber connectors.

The process of fabrication of a fiber bundle is fully depicted in Fig. 2-1 and described as follows:

(a) Prepare epoxy (EpoxyBound 110, ©Allied High Tech Products), dozens of a few centimeters long 62.5/125 μm multimode fibers (MMFs), an aluminum cylinder, which was a two-piece ferrule, as depicted in Fig. 2-2. MMF was chose for much

light capturing. For successful splicing and coupling, strip the coater of fiber and let each fiber end flat by using a conventional cleaver. The fibers were inserted into the aluminum cylinder until fibers was packed tightly as shown in Fig. 2-1 (a). The flat fiber ends and the aluminum cylinder end were placed in the same plane.

(b) Cut the portion of the other fiber ends (we call uneven fiber ends) over end of the aluminum cylinder as shown in Fig. 2-1 (b).

(c) Let the uneven fiber ends and the aluminum cylinder end at a same level. Mix epoxy A and epoxy B at the ratio 10:1, and then drop a few drops of epoxy on the uneven fiber ends. The epoxy would infiltrate into the gaps among the fibers by siphoning as shown in Fig. 2-1 (c).

(d) As shown in Fig. 2-1 (d), the bottom silicon substrate was put between the hotplate and the fiber bundle for escaping fiber ends contacted the rough surface of the hotplate directly. To avoid the firm sticking between the silicon substrate and the fiber bundle, PDMS was spin coated on the silicon substrate. It is well known that PDMS is a hydrophobic polymer and PDMS could be used for anti-adhesion. By adding two silicon wafers between the aluminum cylinder and the PDMS film, the fibers can extrude over the aluminum cylinder by about hundreds microns. Then, we could confirm the fibers would not be hidden by epoxy after polishing. As all set ready, the epoxy was cured at 120℃ by using a hotplate for 1.5 hours.

(e) Finally, we sent the fiber bundle to some service provider, and the uneven fiber bundle ends could be polished. Fig. 2-3 shows the optical microscope (OM) photo of the fiber bundle after polish and height distribution by laser confocal scanning microscope.

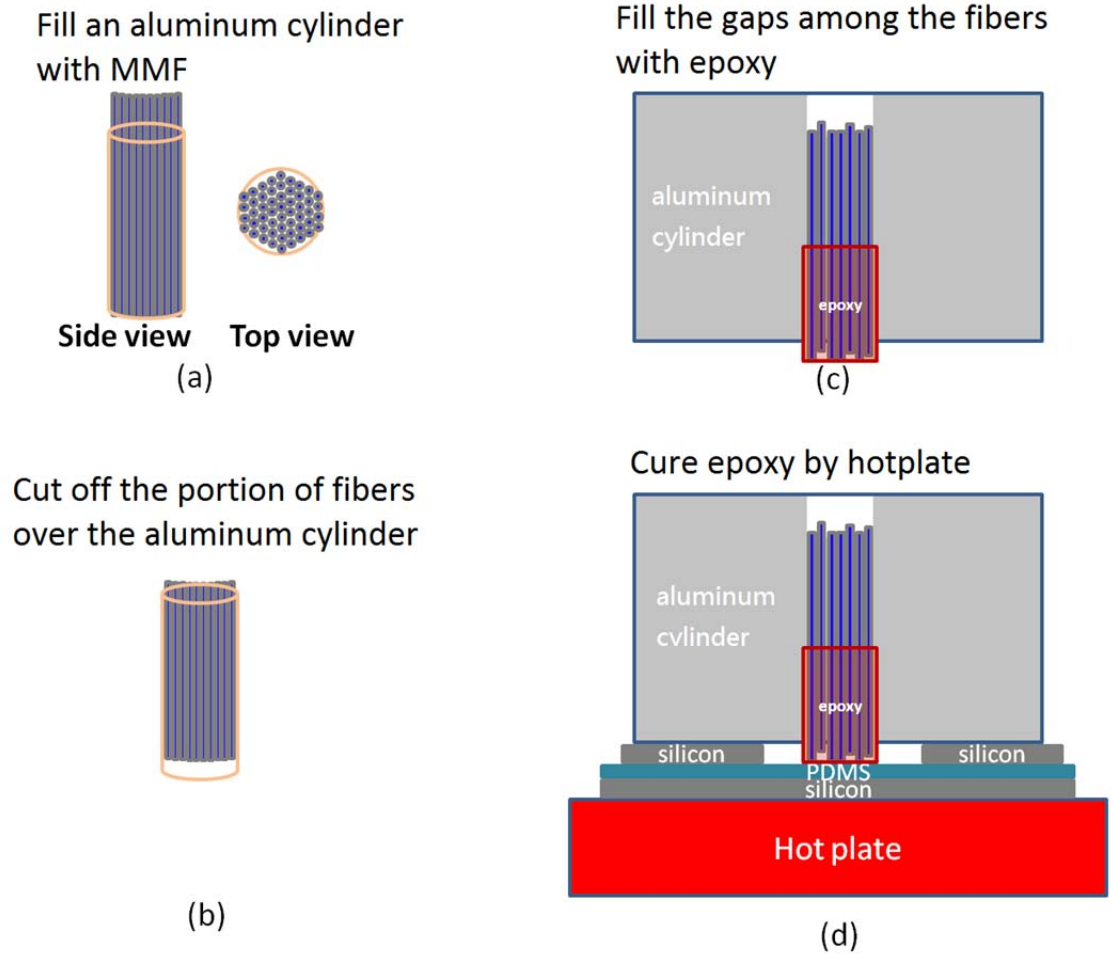

Fig. 2-1 Schematic diagram of fiber bundle fabrication.

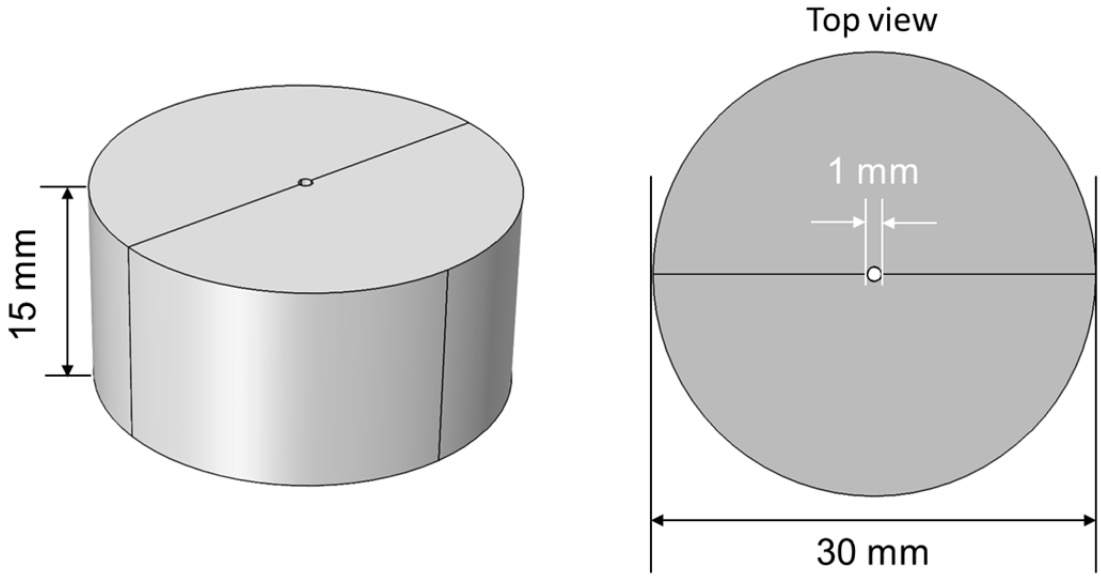

Fig. 2-2 The drawing of an aluminum cylinder designed for fabrication of fiber bundle.

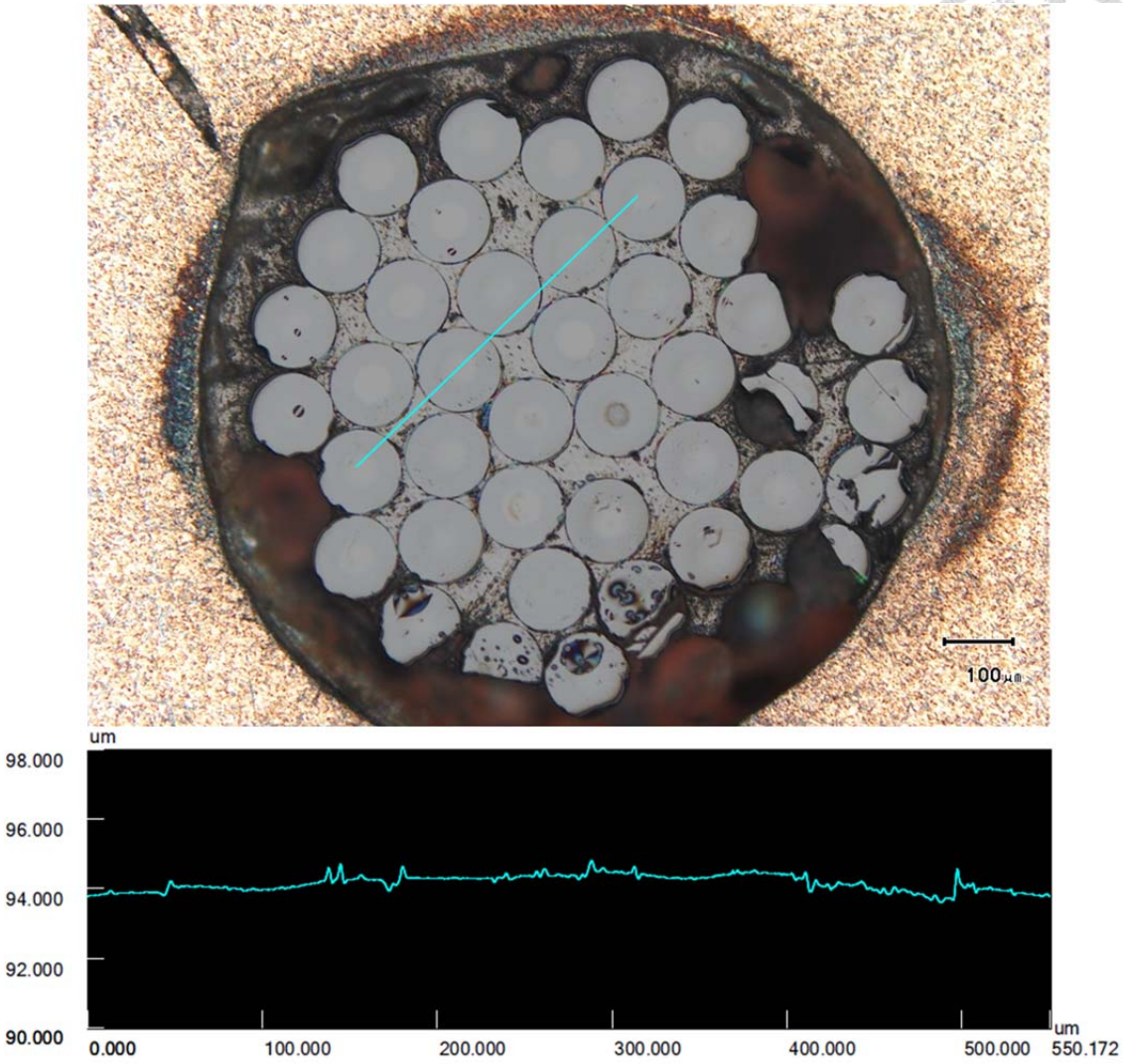

Fig. 2-3 OM photo of the fiber bundle polished facet and diagram of height distribution by laser confocal scanning microscope.

2.2 Fabrication of the stamps for nTP

To obtain the stamps for nanotransfer printing (nTP), we have to fabricate the mold with patterns designed and replicate the patterns to the stamps. In our lab, two-beam inteference lithography (IL) has been studied for several years. Besides the advantages of low cost, high throughput, two-beam IL can define regular patterns easily on the photoresist (PR) film. The material chosen here for the stamps is PDMS (Sylgard 184, ©Dow Corning), which is widely used in NIL or other applications for replication. In this section, we introduce the concept and the system of two-beam IL. Then, the following procedures for the fabrication of the PDMS stamps are listed.

2.2.1 Two-beam inteference lithography

The schematic system layout of our vertical exposure system is shown in Fig. 2-4. Based on the interference theory, the use of s-polarized beams to form interference fringes is better than that of p-polarized, because the contrast of the interference fringes will be varied by the incident angles in the latter case. Therefore, a polarization beam splitter (PBS) is utilized to increase the extinction ratio of s-to p-polarization wave in the exposure beam. The next three elements of objective lens, pinhole, and a collimated lens act as a spatial filter for eliminating the unwanted diffraction signals formed in the previous optical route and collimate the expansion beam to have a size of 50 mm in diameter. After the spatial filter, a right-angle prism will bend the beam upward to propagate over an optical bench that is standing on the optical table vertically. A beam splitter is used to separate the expanded beam into two beams, and the Mirror 1 and Mirror 2 are used to overlap two beams to form interference fringes on the stage.

The contrast of the interference fringes, C, is defined as

$$C = \frac{2\sqrt{I_1 I_2}}{I_1 + I_2} \tag{2.1}$$

where I_1 and I_2 are the laser intensity of the two split beams. When the contrast is equal to 1 which means the perfect contrast, the contrast of two split beams are controlled equal to 1 to obtain the clear pattern over the entire exposing area.

Based on the basic principle of two beam interference, the period of grating could be determined by the incident wavelength and incident angle of incident light. The period of grating pattern could be expressed as

$$\Lambda = \frac{\lambda}{2\sin\theta} \tag{2.2}$$

where Λ is the period of grating, λ is the wavelength of incident light, and θ is the angle of incident light. By varying the incident angles, different periods of gratings can be obtained. The schematic diagram of the two-beam IL is depicted in Fig. 2-5.

In our experiment, the wavelength of incident light was 364 nm (i-line). We adjusted the Mirror 1 and Mirror 2 with the same incident angle which was about 21.35 degree. From Eq. (2.2), the period of gratings was close to 500 nm. Then we could produce the gratings over about 1 inch × 1 inch with proper exposure dosages.

For the grating patterns, just one single-exposure is needed. However, to fabricate the pattern suitable for hole or post arrays, the double-exposure method is introduced. After the first exposure with half of the designed exposure dose, the substrate is rotated by 90 degree. Then the second exposure with the same dose is applied. Since the margin of PR pattern will form a wave-like curve after post-exposure bake (PEB) due to the different exposure doses at the overlapped and the non-overlapped regions, the hole-array pattern shown in Fig. 2-6 can be fabricated. Actually, we can control the

linewidth of PR pattern by changing the exposure dose. Fig. 2-7 shows the shape variation of different doses. The shape changes from hole to rod as the exposure dose increases from 45 mJ/cm^2 to 98 mJ/cm^2 as the holes expand.

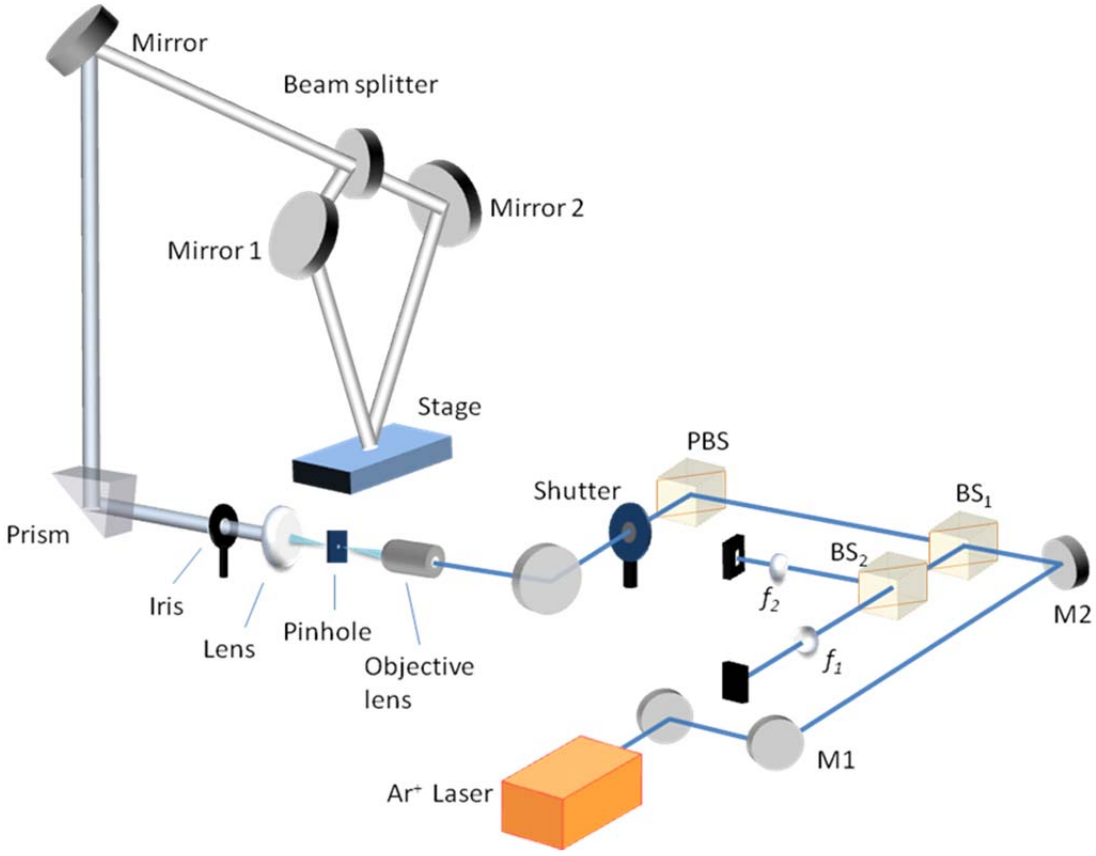

Fig. 2-4 Schematic of the two-beam IL system in our lab [22].

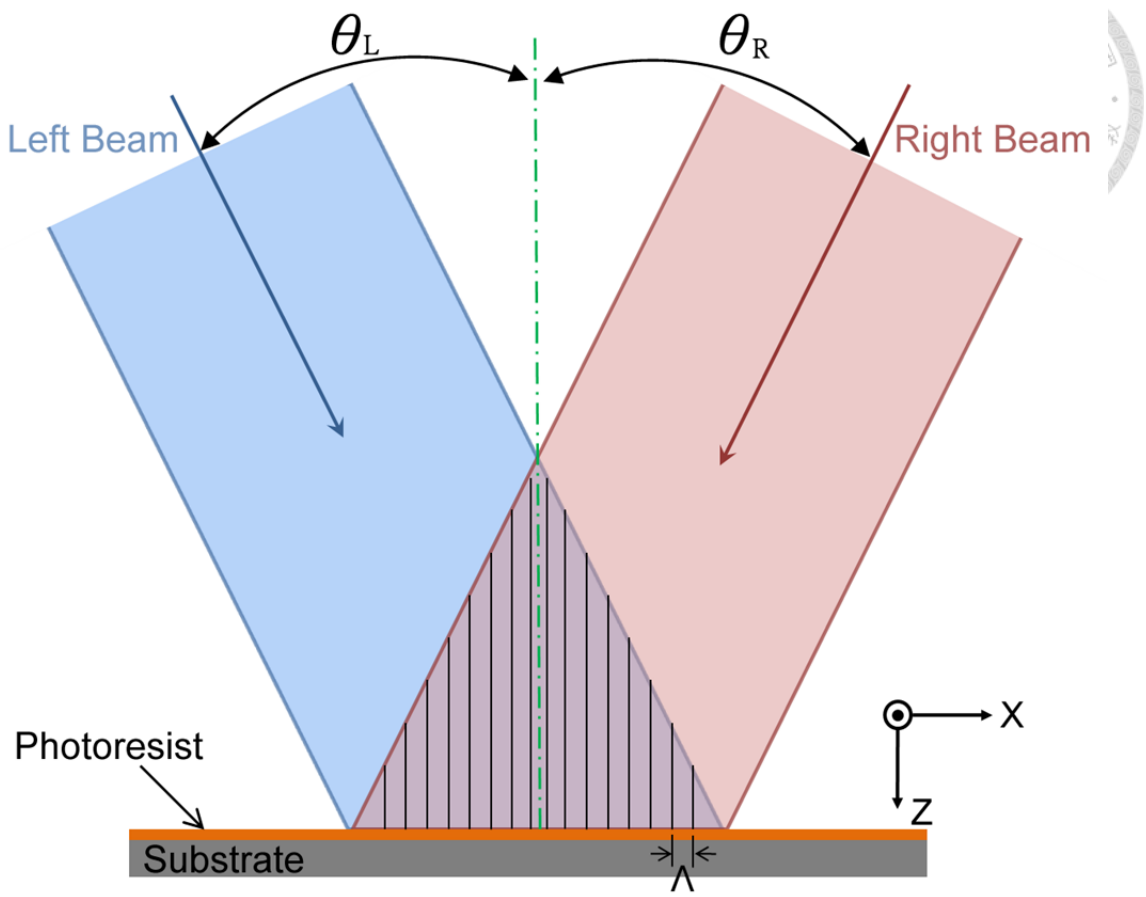

Fig. 2-5 Schematic of two-beam IL [23].

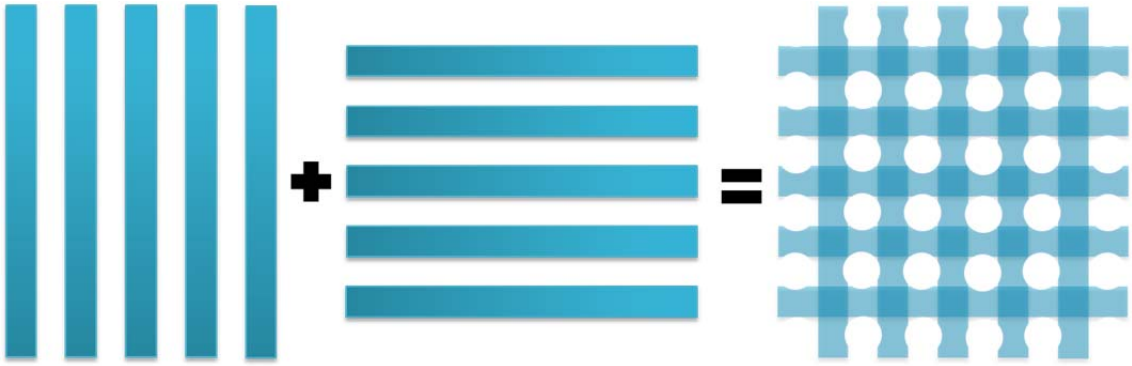

Fig. 2-6 Hole-array PR pattern generated by double-exposure [24].

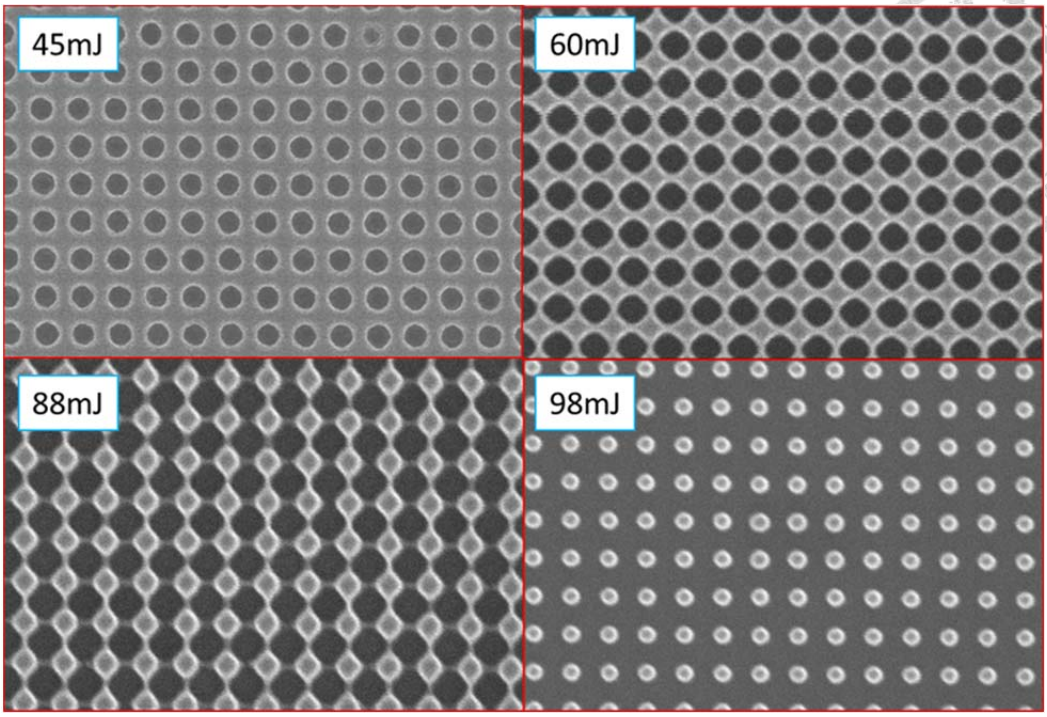

Fig. 2-7 PR patterns with different exposure dose [24].

2.2.2 Fabrication and stability of the PDMS stamps

The procedures of fabrication of the PDMS stamps are simply described as follows:

(a) Put the molds with PR patterns in a petri dish, then pour the PDMS in the petri dish.

(b) Place the petri dish in the chamber to make the molds closed with the bottom of the petri dish by vacuumizing. After the vacuumizing, the petri dish filled with PDMS is baked at 65℃ for 6.5 hours.

(c) Release the PDMS from the molds by hands after the PDMS is solidified and the negative patterns of the PR structures are replicated on the PDMS stamps.

Fig. 2-8 shows the scanning electron microscope (SEM) photo of rod array pattern on the PDMS stamps replicated from the hole array PR pattern of period 500 nm.

Nevertheless, this simple procedure can be unstable for the PDMS nanostructures of period 500 nm. In the step (b) and (c) mentioned above, the low molecule weight (LMW) chains and the stresses applied on the stamps cause the deformation of the nanostructures with aspect ratio bigger than 1 with time. For the case of aspect ratio ~ 1 (our case), the deformation is mainly due to the LMW chains on the surface of PDMS [25]. The LMW chains, which are either uncrosslinked linear PDMS chains or residual crosslinking agent, cause the adhesion of two PDMS surfaces by van der waals forces between them [25, 26]. The dynamic deformation of paired grating lines on the stamps could be clearly seen by OM with time as shown in Fig. 2-9. The situation became terrible after the stamps placed for 1 day as shown in Fig. 2-10. The cross-like deformation also occurred for rod array pattern but moderately relative to the grating pattern as shown in Fig. 2-11. We thought the reason was that the van der waals forces on the side walls between two rods were smaller than that between two grating lines.

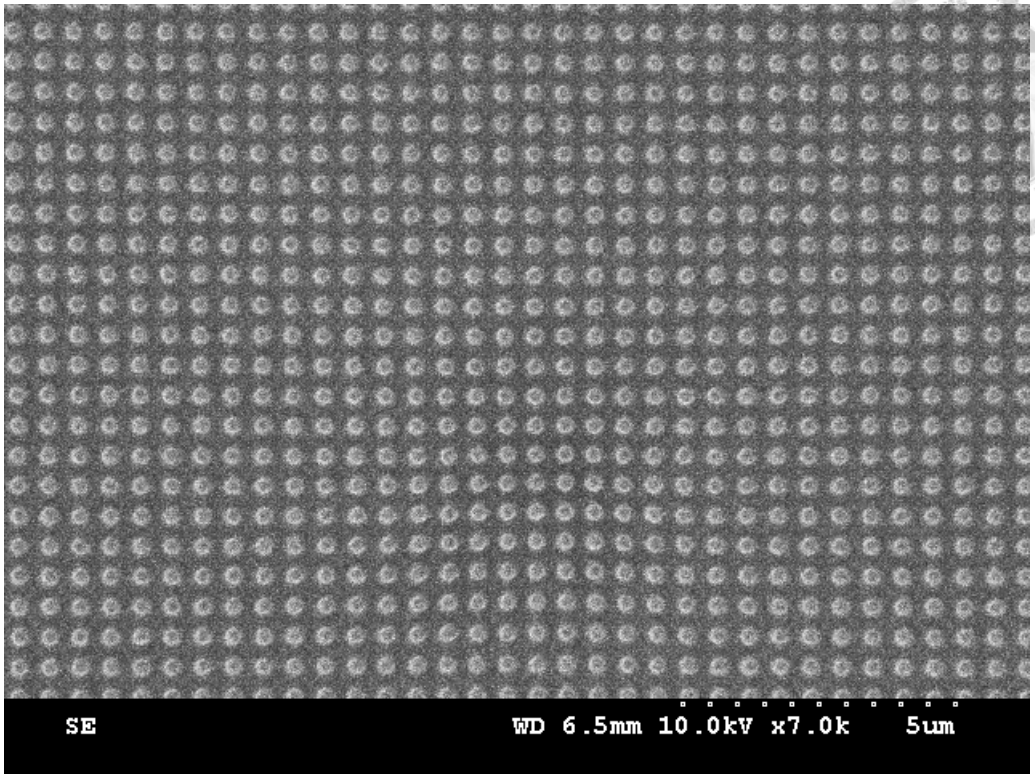

Fig. 2-8　SEM photo of rod array pattern of period 500 nm on the PDMS stamps.

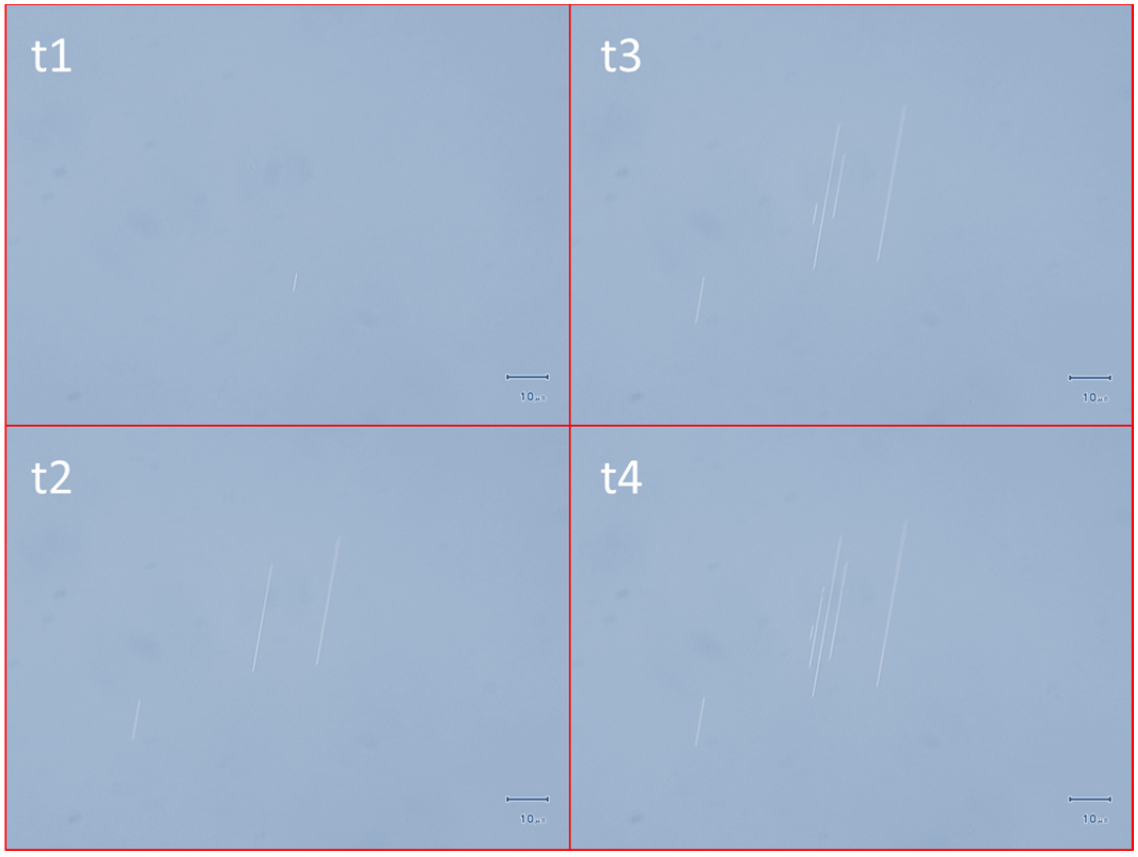

Fig. 2-9　OM photos of paired grating lines on the PDMS stamps in a series of time.

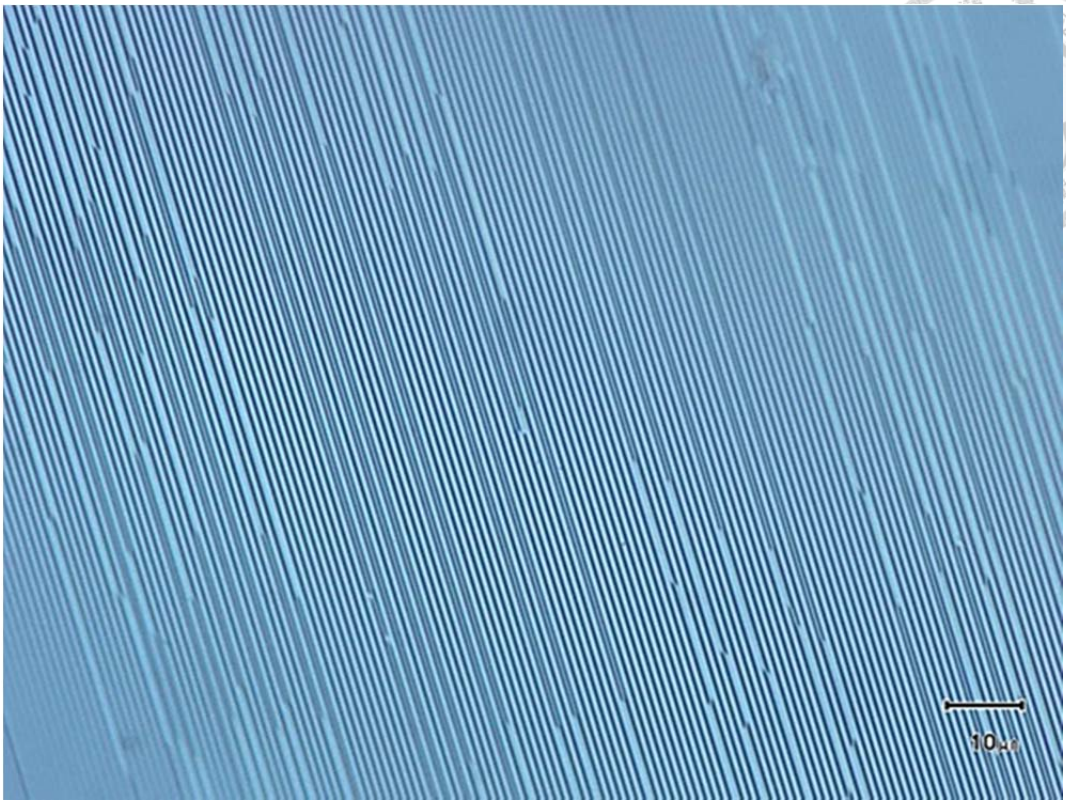

Fig. 2-10 OM photo of paired grating lines on the PDMS stamps placed after 1 day.

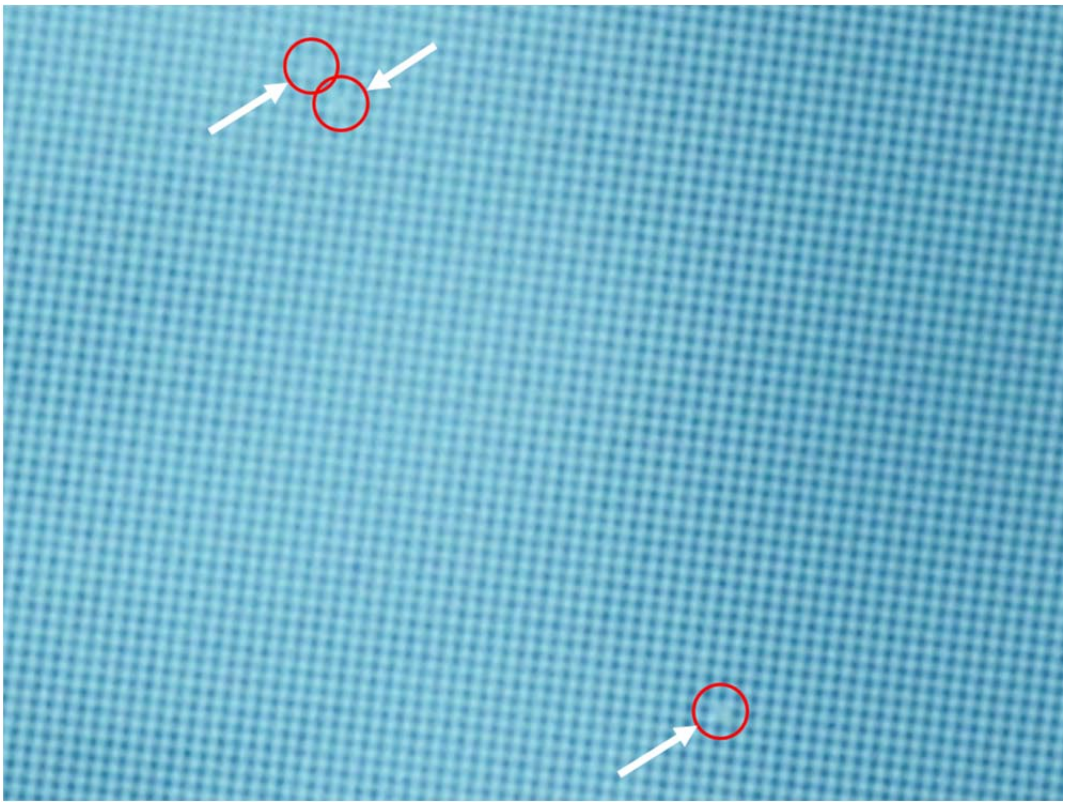

Fig. 2-11 Magnified OM photo of cross-like deformation on the PDMS stamps.

2.3 Extraction of low molecular weight PDMS chains

The existence of the deformations as described in the last section is a serious problem in any printing process. We may obtain totally wrong pattern after printing process if the stamps with deformations are used. As mentioned, the deformations are mainly due to the LMW PDMS chains. That is to say, if the LMW chains are removed, the deformations will disappear. In this section, two extraction ways of LMW chains are introced. Because the defects for grating patterns are relatively clear, we use the stamps with gratings to test the extraction here. The two ways are also compared at the end.

2.3.1 Extraction by organic solvents

Many works has been reported that LMW PDMS chains can be extracted by organic solvents, such as hexane and trimethylamine [27-29]. It is concerned with the solvent compatibility of PDMS. Generally, high solvent compatibility of PDMS has to be avoided for PDMS based devices, such as microfluidic. It can cause the serious swelling of the devices [30]. However, here we take the advantage of the high solvent compatibility to extract the LMW chains. We first explain the principle of this extraction method by the solubility parameter, δ, of the solvents. The solubility parameters of some solvents used in organic synthesis are listed in Table 2-1.

According to Ref. 30, solvents that have δ similar to that of PDMS ($\delta = 7.3$ $cal^{1/2}$ $cm^{-3/2}$) generally swell PDMS more than solvents that have δ substantially different from that of PDMS. Fig. 2-12 shows the relationship between the swelling ratio, S, of PDMS in various solvents and δ. However, one can observe that the swelling ratios can be somewhat different even if the solvents have the same values of δ.

Actually, the solubility parameter can be expressed as

$$\delta^2 = \delta_d^2 + \delta_p^2 + \delta_h^2 \quad (2.3)$$

where δ_d is the dispersion forces, δ_p is the polar forces, and δ_h is the hydrogen-bonding forces. Two solvents with same δ but a different proportioning of the values among δ_d, δ_p, and δ_h may show substantial differences in swelling of PDMS. Despite the fact that values of the three parameters are not yet available for PDMS and for many organic solvents, we can consider the readily available dipole moment, μ, of the solvent to help explain that trends. The dipole moments of the solvents in Table 2-1 are also listed. For example, in the case of trimethylamine (μ = 0.7) and ether (μ = 1.1), trimethylamine swelled PDMS more than ether for μ of the trimethylamine is more similar to that of PDMS as shown in Fig. 2-12.

For extraction, the procedures used in Ref. 28 are described as follows:

(a) Immerse the PDMS stamps in hexane solution at room temperature and stir for 4 hours. The solution was refreshed each hour.

(b) Remove the stamps to ethanol solution at room temperature and stir for 4 hours. The solution was refreshed each hour.

(c) Remove the ethanol solution and bake the stamps at 80℃ for 1 hour.

It should be clarified that step (a) was the only extraction process. The purpose of ethanol solution used in step (b) was to prevent a violent shrink of PDM, which would damage the stamp. In Fig. 2-13, no paired lines were observed on the stamps and the gratings were clearly displayed after the extraction.

solvent	δ(cal1/2cm-3/2)	μ(D)
PDMS	7.3	0.6-0.9
hexanes	7.3	0.0
triethylamine	7.5	0.7
ether	7.5	1.1
toluene	8.9	0.4
ethyl acetate	9.0	1.8
acetone	9.9	2.9
ethylene alcohol (ethanol)	12.7	1.7
methanol	14.5	1.7
water	23.4	1.9

Table 2-1 Solubility parameters, δ, and dipole moments, μ, of various solvents used in organic synthesis [30]

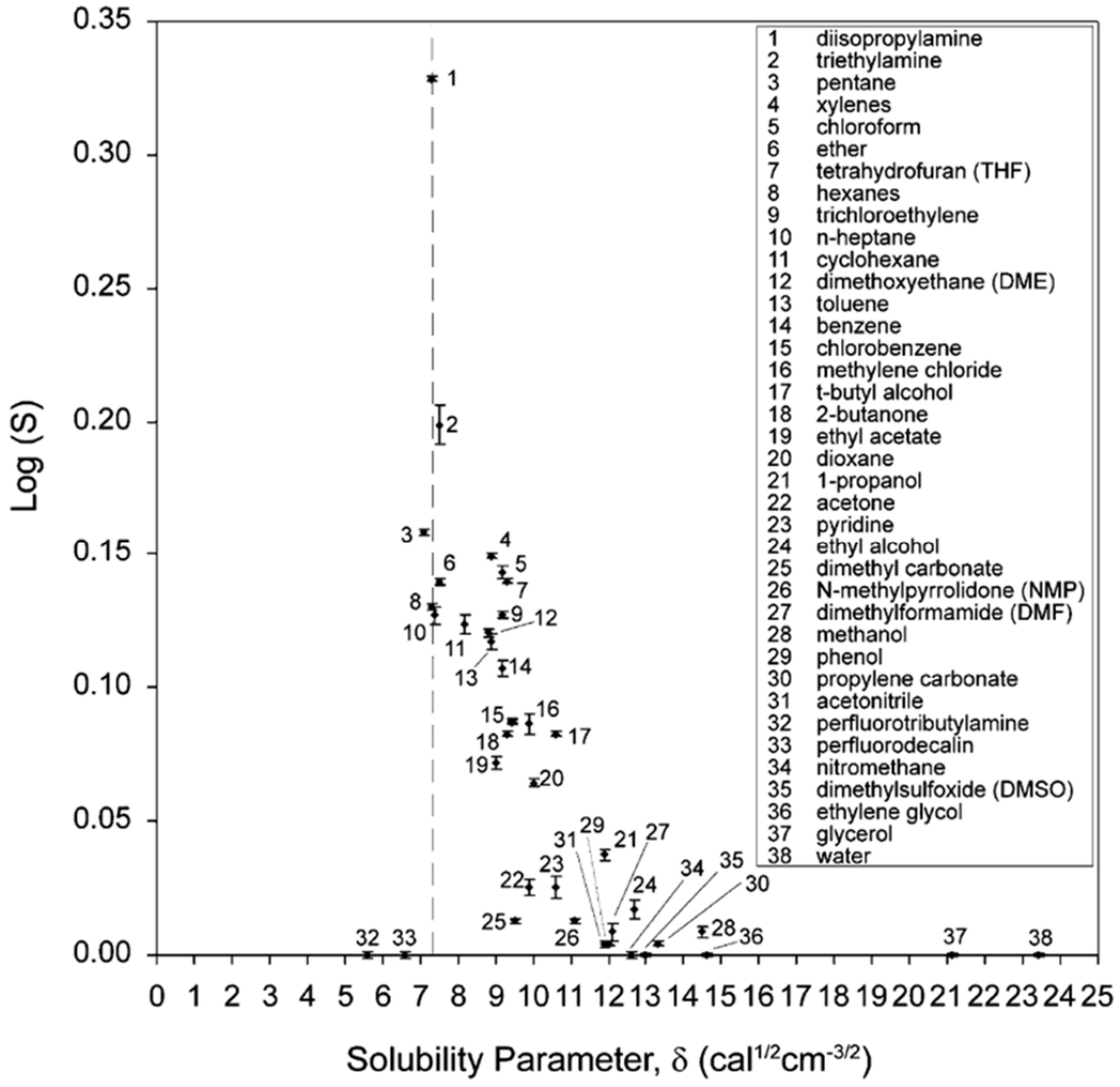

Fig. 2-12 Relationship between swelling ratio, S, shown as Log (S) of PDMS in various solvents and the solubility parameter, δ. The dashed line indicates δ of PDMS [30].

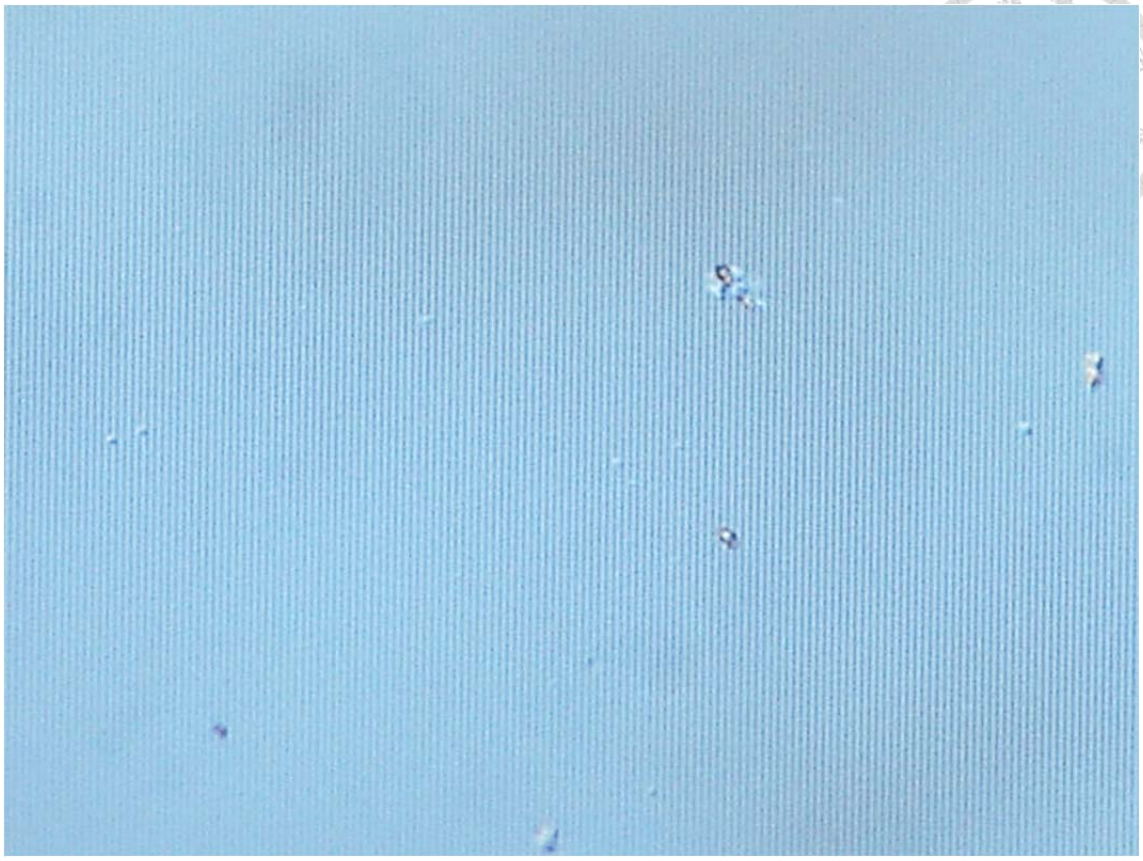

Fig. 2-13 Magnified OM photo of gratings on PDMS stamps after extraction by organic solvents.

2.3.2 Extraction by thermal aging

Besides the method of extraction by organic solvents, another extraction method by thermal aging was also reported [31]. This method just extends the curing time of the PDMS stamps. We take a long curing time at 65℃ for 2 days as a test. The conditions looked good on the stamps with gratings first, but similarly a great deal of paired lines still existed on the stamps. Thermal aging seemed to be an inefficient method for extraction of LMW PDMS chains.

Fortunately, we can make thermal aging more efficient by some simple skills. The improved procedures are described below:

(a) Spin coat a few PDMS on the mold with PR patterns with the first spin rate, 500

rpm, for 10 sec and the second spin rate, 1750 rpm, for 60 sec.

(b) Bake the molds with PDMS films at 65℃ for 6.5 hours.

(c) Put the molds in a petri dish, then pour the PDMS in the petri dish. After the vacuumizing, the petri dish filled with PDMS is baked at 65℃ for 6.5 hours.

(d) Release the PDMS from the molds by hands after the PDMS is solidified.

Different from the general procedures for fabricating PDMS stamps, we added a spin-coating process at the beginning. In step (b), in contrast to the thick PDMS stamp, the PDMS film was thin enough to absorb the thermal energy efficiently so the long curing time could be shortened to only 6.5 hours. The gratings were clearly displayed after the extraction as shown in Fig. 2-14.

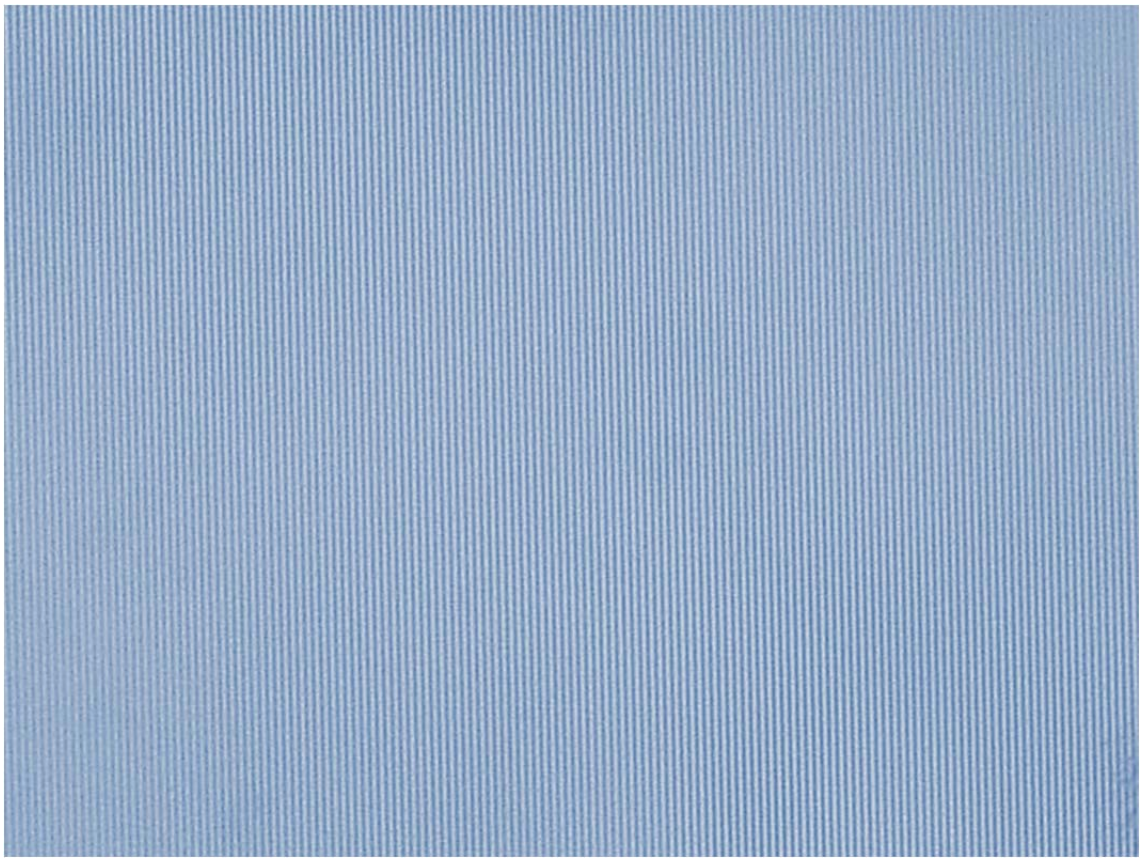

Fig. 2-14 Magnified OM photo of gratings on PDMS stamps after extraction by thermal aging.

2.3.3 Comparison of the two extraction methods

We have introduced the two extraction methods. Here we are going to compare the pros and cons of the two methods.

Both the methods could eliminate the paired lines on the PDMS stamps. The organic solvents worked indeed, but many defects, which was not observed in the case of thermal aging, still existed in fact. We thought the still violent shrink of PDMS and the rude behavior of stirring crumpled and damaged the surface of the gratings as shown in Fig. 2-13 and Fig. 2-15. The surface was too rough to be used in the later process. Besides, the procedures of the extraction by organic solvents were more complex and took a longer time than the extraction by thermal aging. Apparently, thermal aging is a better method for the extraction of LMW chains on the PDMS stamps. We will choose the stamps treated with thermal aging in the later nTP. The comparisons of the two extraction methods were listed in Table 2-2.

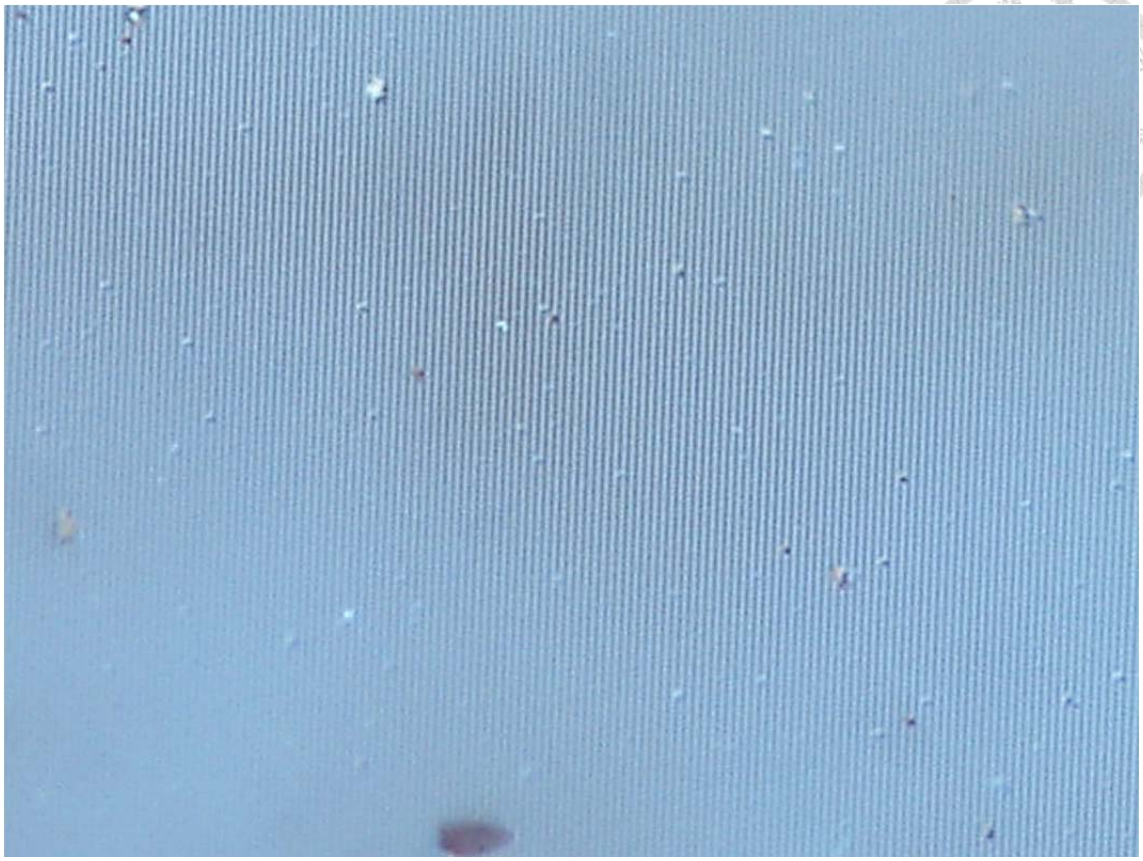

Fig. 2-15 Magnified OM photo of gratings on PDMS stamps after extraction by organic solvents.

	Organic solvents	Thermal aging
Complexity of the procedures	complex	simple
Paired lines	not observed	not observed
Surface of the gratings	rough	smooth
Total time consumed	9 hours	6.5 hours

Table 2-2 Comparisons of the two extraction methods

2.4 Applying nTP on the glass substrate

About the principle of nTP, as mentioned before, it relies on the stamps with low surface energy for pattern transferring to the substrates with relatively high surface energy [15]. Generally, the surface energy of glass is larger than that of PDMS stamp [32-35]. To simulate the condition on the fiber bundle and to optimize the parameters used in nTP process, we used glass slides as the substrate. The set-up of the process is depicted in Fig. 2-16 and the procedures are described below:

(a) First heat the upper and the lower plates of the imprint machine to a temperature of 100℃ to further lower the surface energy of PDMS.

(b) After put a PDMS stamp (LMW chains were extracted by thermal aging) coated with 50 nm gold film by E-gun evaporator on the glass substrate, put a same-sized silicone on the stamp. Then, put the whole set between the upper and the lower plates. The silicone served as a buffer. It could not only retard the abrupt pressure but also help make the pressure on the stamp more uniform.

(c) Apply a pressure of 425 psi on the set-up for 55 seconds and then release the stamp and the silicone on the substrate. At the same time, the gold nanostructures were transferred onto the glass substrate.

The results of the transferred gold nanostructures of gratings and hole array near the center of the glass substrates are shown in Fig. 2-17 and Fig. 2-18, respectively. The patterns looked uniform and remained intact. The 514 nm period and the 317 nm width of the gratings are shown in the inset of Fig. 2-17. The 506 nm period and the 348 nm diameter of the holes are shown in the inset of Fig. 2-18. The two values of the periods were very close to the period designed in the two-beam IL. Interestingly, by examining the defects on the patterns as shown in Fig. 2-19, the structure was found to be a

continuous 3D film which was attributed to sloping sidewalls of the stamps and the cohesion of the gold [16, 17]. Apparently, the darkest region stood for the glass substrate. Actually, we thought the continuous gold film resulted from both the sloping sidewalls and the scattering of the gold vapor particles in the deposition process. In addition, since the cohesion of the gold is stronger than its adhesion to the PDMS stamp, the regions of the continuous gold film that are not in contact with the substrate can form free-standing structures.

Though there are three parameters referred in the nTP process, only time can influence the results significantly. Generally, high temperatures lower the surface energy. The surface energy of PDMS is about 20 mN/m at room temperature. However, it can be barely reduced to about 8 mN/m at 300℃ as depicted in Fig. 2-20. As for the pressure, to prevent from the severe deformation of the patterns on the stamps, low pressure is preferred, but over low pressure is also harmful to the imprint machine. Based on the reasons above, time is the only one parameter we cared. Fig. 2-21 shows the influence on the transferred patterns with different times for imprinting. Intuitively, the longer the time for imprinting, the more intimate the contact and the more uniform the pressure applied on the stamps. The coverage of each transferred pattern directly reflected this concept. Unfortunately, an increase of contact time also aggravated the deformation of the stamp. Many cracks existed on the pattern as shown in Fig. 2-22 and the gold nanostructures were flattened so the intensities of the diffraction light reduced. There was a trade-off between the coverage and the completeness of the transferred pattern.

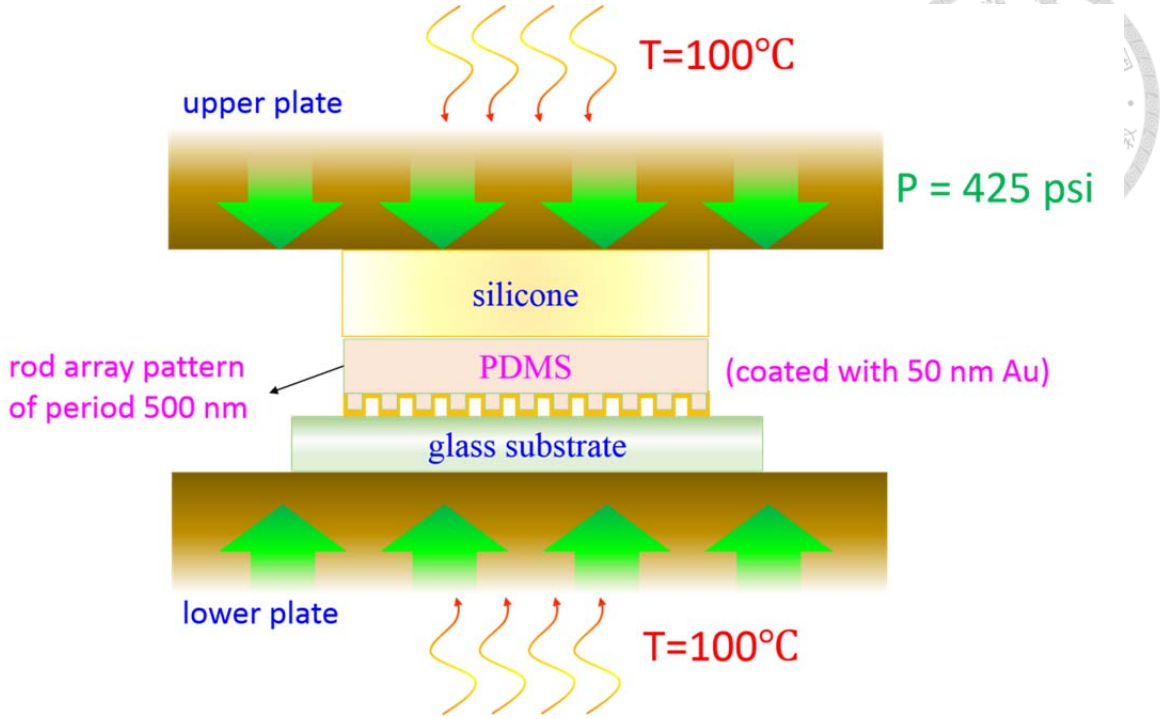

Fig. 2-16 Schematic set-up of the nTP process.

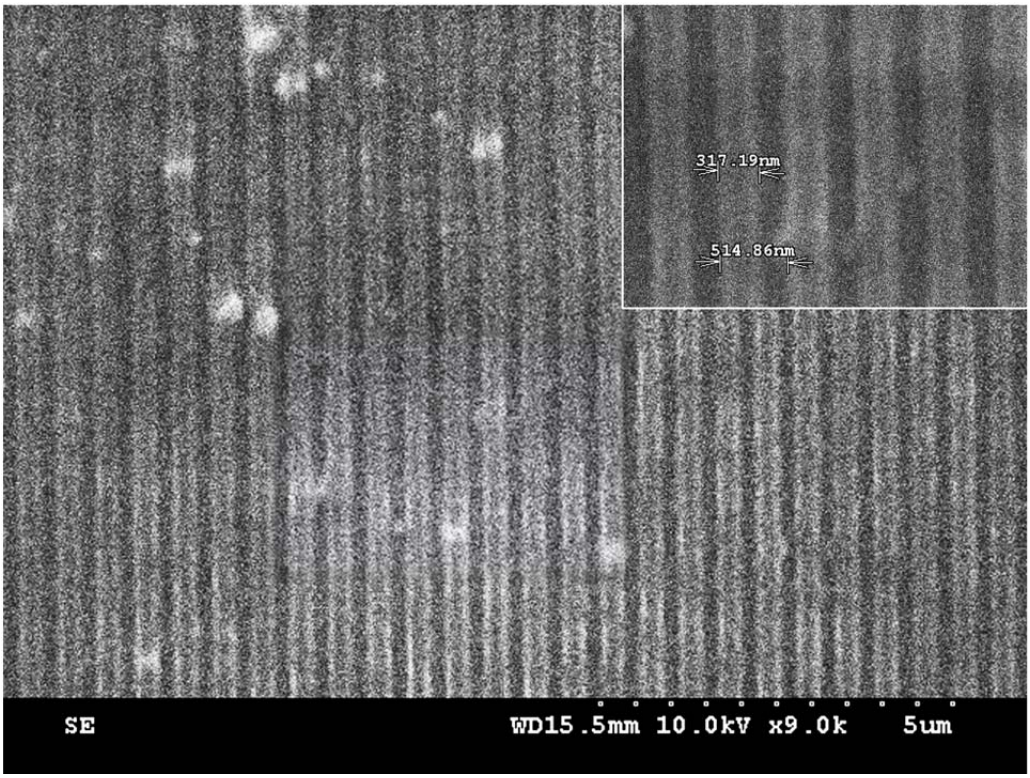

Fig. 2-17 SEM photo of gold gratings transferred onto the glass substrate. The inset shows the 514 nm period and the 317 nm linewidth of the gratings.

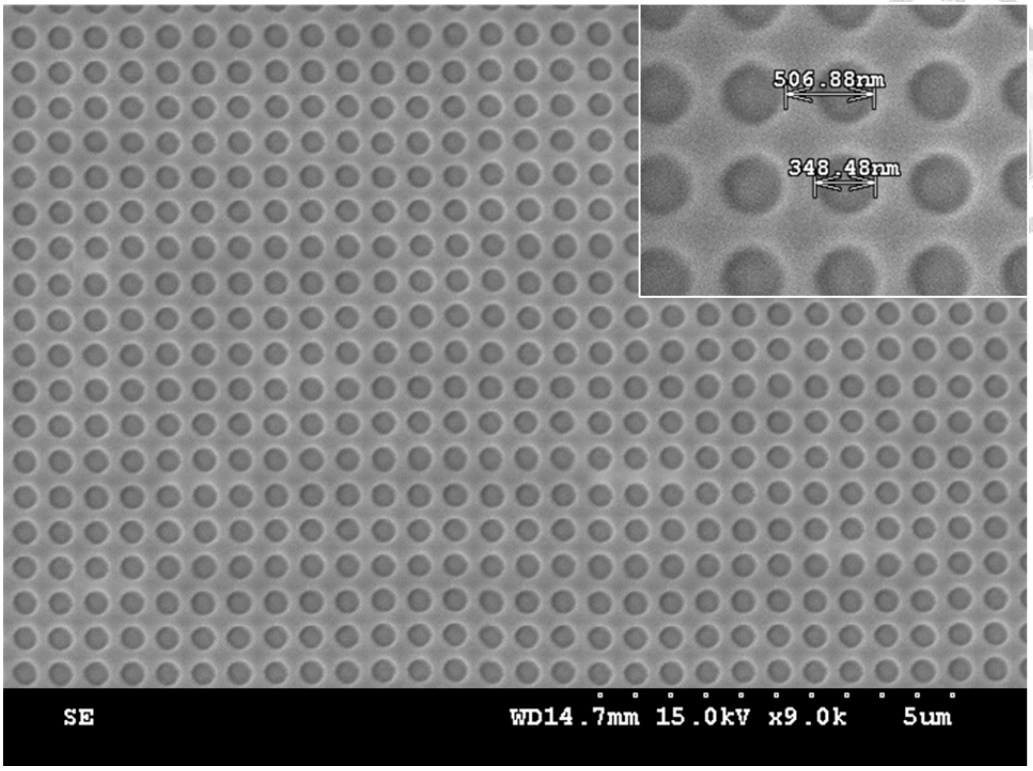

Fig. 2-18 SEM photo of gold hole array transferred onto the glass substrate. The inset shows the 506 nm period and the 348 nm diameter of the holes.

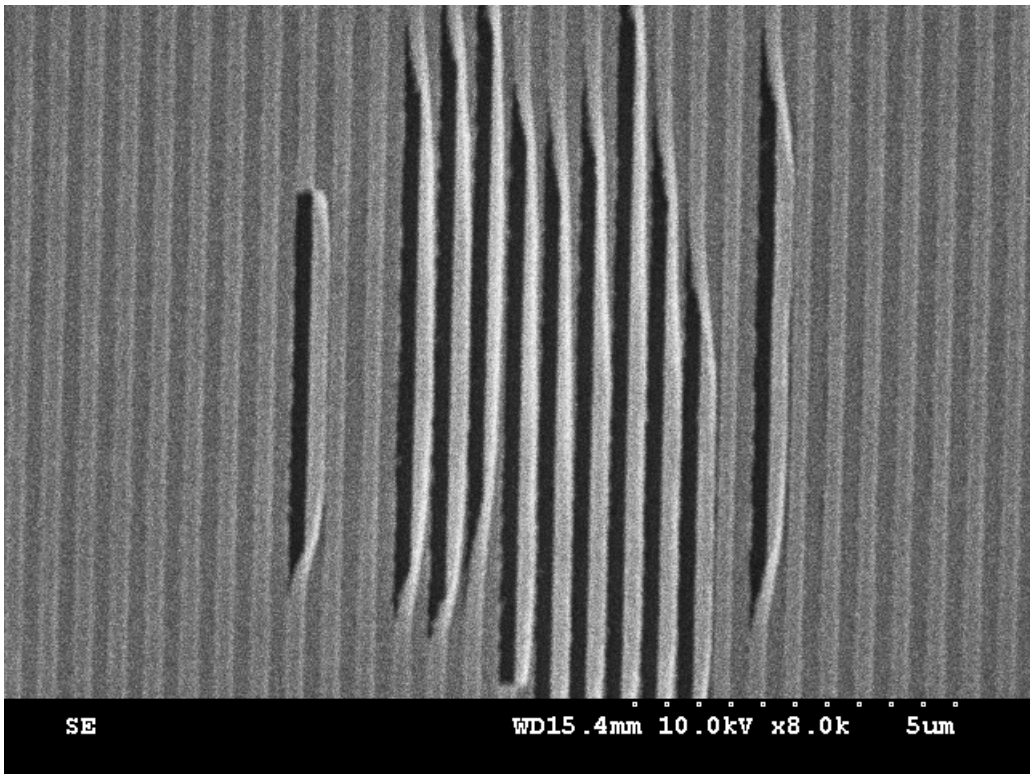

Fig. 2-19 SEM photo of the defects of the gold gratings.

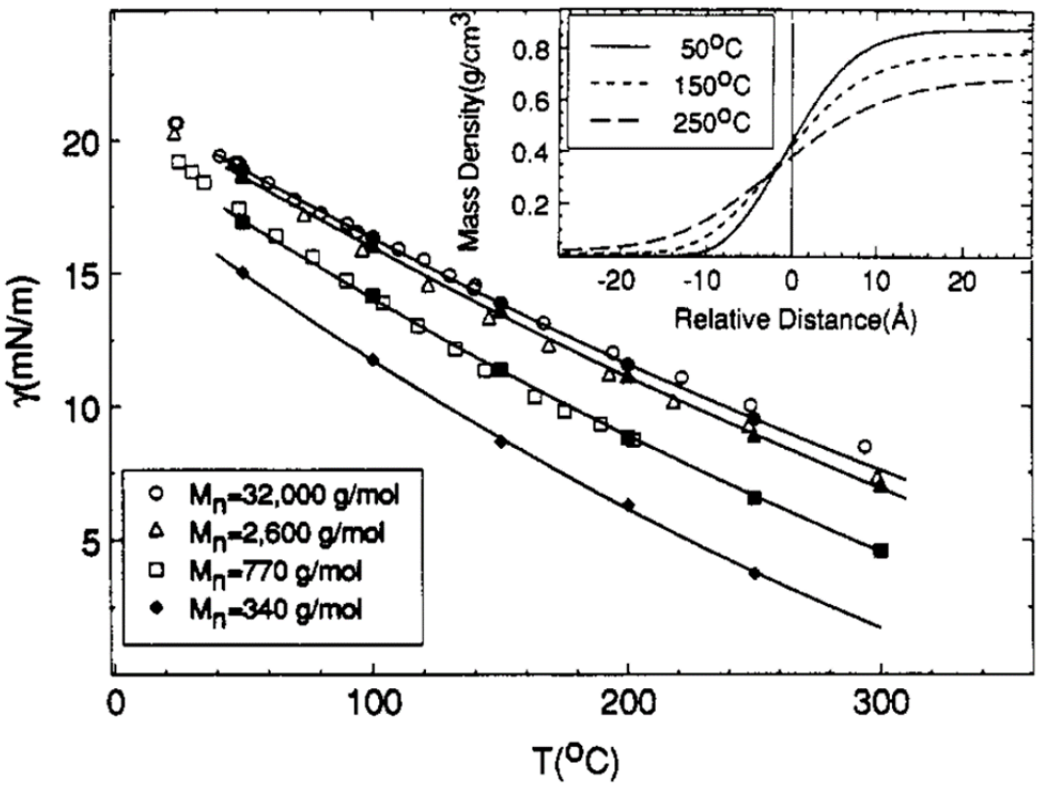

Fig. 2-20 Temperature dependence of PDMS surface energy [32].

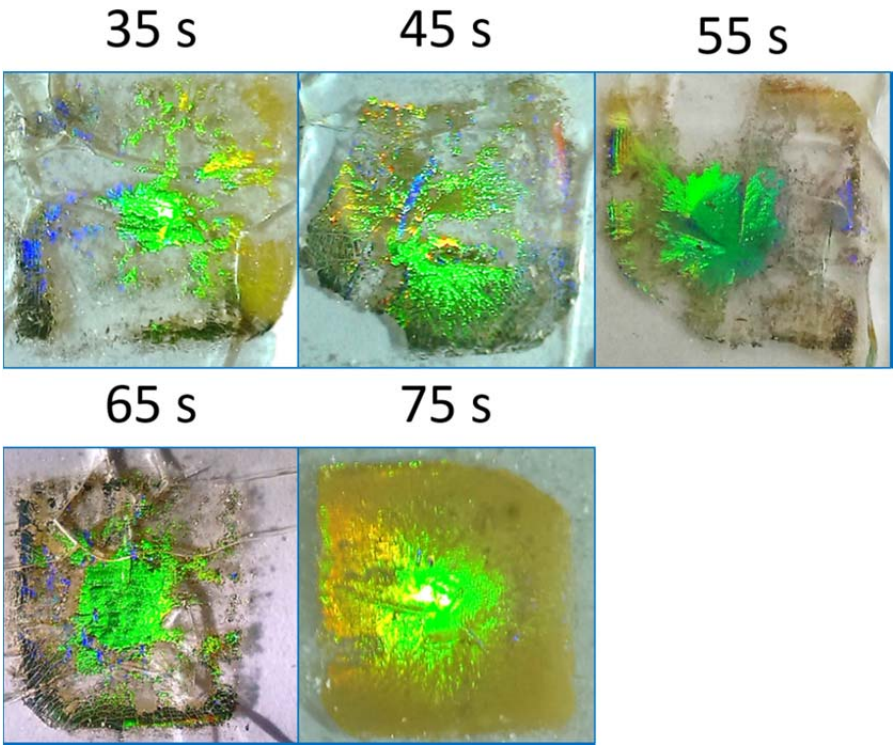

Fig. 2-21 Time dependence of the pattern coverage on glass substrates at a pressure of 425 psi in the nTP process.

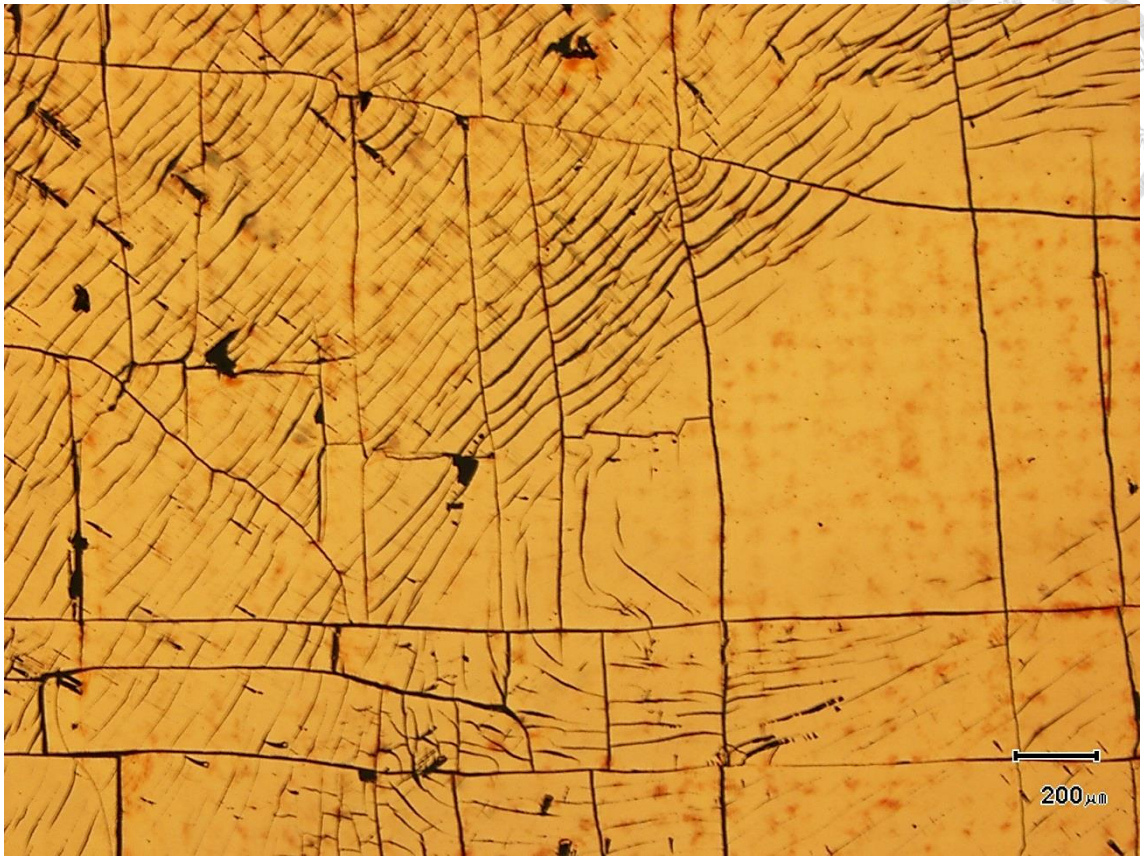

Fig. 2-22 OM photo of the transferred pattern imprinted for over 75 seconds.

2.5 Applying nTP on the fiber bundle and separating SPR fiber probes

Similarly, we applied the procedures described in the last section on the fiber bundle. The set-up of the process is depicted in Fig. 2-23. The fiber bundle was just substituted for the glass substrate. To transfer hole array pattern onto the bundle, we chose the stamps with rod array pattern in this case. It can be realized intuitively that an array pattern can offer the interaction between the gold nanostructures and light in the second direction relative to a grating pattern.

Fig. 2-24 shows the picture of a fiber bundle after nTP process. Visible light diffraction caused by the gold hole array on the bundle is clearly seen, which indicates a successful pattern transfer from the stamp. The pattern coverage on the bundle also looks in good condition and reaches almost 90% as shown in Fig. 2-25. The detailed structures near the center of the fiber core were examined by SEM as shown in Fig. 2-26. This figure shows a fine pattern in an about 20 μm × 20 μm area of the fiber core. The difference between the values of the diameters of the holes shown in the insets of Fig. 2-18 and Fig. 2-26 might result from the slight difference between the pressures on the stamps in the case of glass substrate and fiber bundle.

For practicality, the fiber bundle with the patterns should be separated into the SPR fiber probes. The separating process is depicted in Fig. 2-27. First, because the 3D gold film covered the whole bundle absolutely, there was no channel for the etchant to flow into. Therefore, the two-piece aluminum cylinder must be taken apart. Then each part was put in the etchant for epoxy (DY-711, ©Dynaloy Engineered Chemistries), which was heated to 100℃ to speed up the etching process. The temperature higher than the boiling point (120℃) should be avoided to prevent the evaporation of the etchant and

the instability of the liquid level, which could damage the patterns on the fiber probes. The condition of the process should be checked every 20 minutes until the fiber probes could be totally removed from the aluminum cylinder.

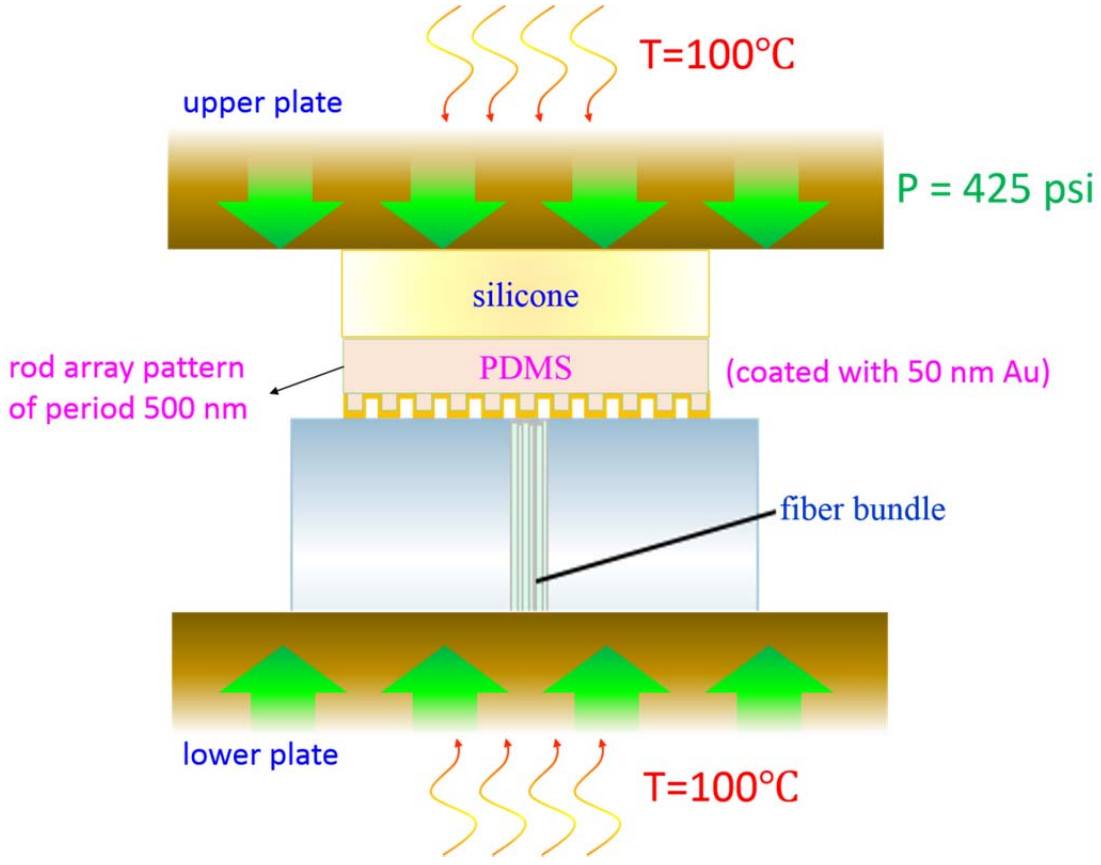

Fig. 2-23 Schematic set-up of the nTP process for fiber bundle.

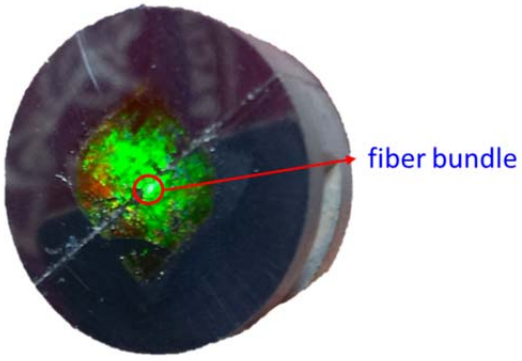

Fig. 2-24 Picture of a fiber bundle after nTP process with the diffraction light.

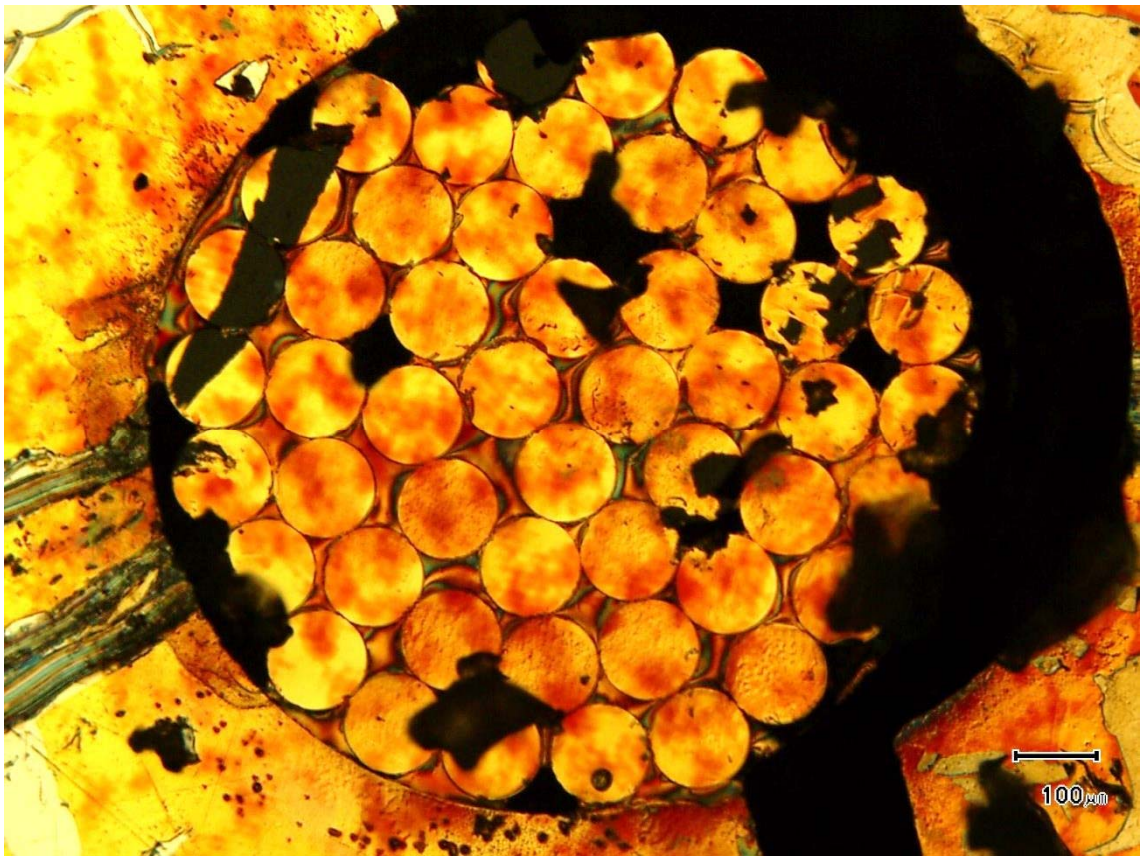

Fig. 2-25 OM photo of the fiber bundle with transferred hole array pattern.

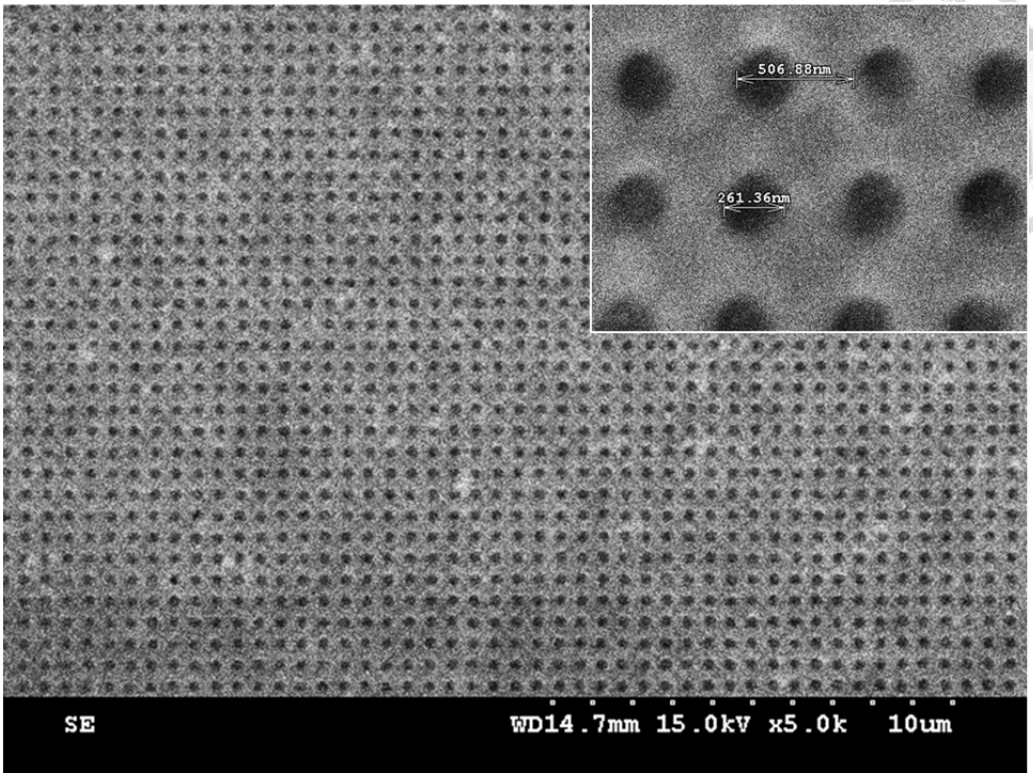

Fig. 2-26 SEM photo of the transferred hole array pattern near the center of a fiber core. The inset shows the 506 nm period and the 261 nm diameter of the holes.

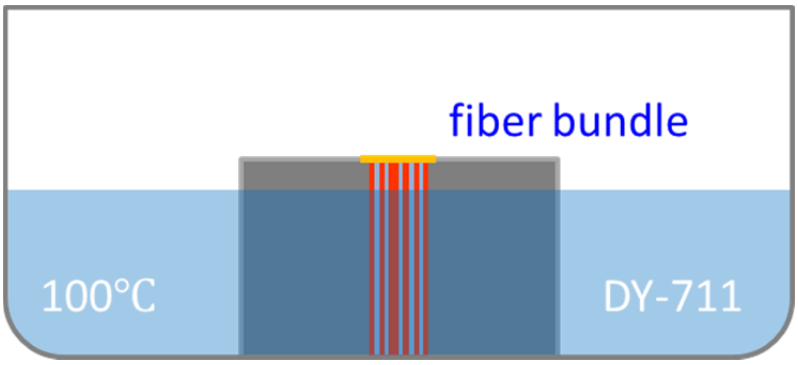

Fig. 2-27 Schematic diagram of the separating process.

Chapter 3 Simulation of 3D Metallic Gratings on Optical Fiber Ends

3.1 The dielectric function of metals

Before we start to explain the theory of SPPs, we introduce the dielectric function of metals, which mainly describes the optical properties of metals. First we introduce the classical Drude model. The model is based on the assumption that the metal can be described as plasma, namely, a gas of electrons with a number density, *n*. Details of the lattice potential and electron-electron interaction are not taken into account. Instead, the effective optical mass of the electron is considered [36].

We can write the equation of motion for an electron of plasma forced by an external time harmonic electric field $\mathbf{E}=E_0 e^{-i\omega t}$:

$$m\ddot{\boldsymbol{x}} + m\gamma\dot{\boldsymbol{x}} = -\mathrm{e}\mathbf{E} \tag{3.1}$$

where m is the effective optical mass, γ is the characteristic collision frequency. The solution solved from Eq. (3.1) is:

$$\boldsymbol{x} = \frac{\mathrm{e}}{m(\omega^2 + i\gamma\omega)}\mathbf{E} \tag{3.2}$$

Then, by inserting the polarization $\mathbf{P}=-ne\boldsymbol{x}$ into the electric displacement $\mathbf{D}=\varepsilon_0\mathbf{E}+\mathbf{P}$, we get the dispersive complex dielectric function $\varepsilon_m(\omega)$ of the free electron gas:

$$\varepsilon_m = 1 - \frac{\omega_p^2}{\omega^2 + i\gamma\omega} \tag{3.3}$$

where $\omega_p = \sqrt{\frac{ne^2}{\varepsilon_0 m}}$ is the plasma frequency. Fig. 3-1 and Fig. 3-2 show the real and imaginary part of $\varepsilon_m(\omega)$ for gold by Rakic et al. and a Drude model fit to the data. In this case, this model gives a relatively good fit in the infrared. However, the validity

breaks down at the near-infrared, the visible and higher frequencies.

Actually, the interband transitions occur at the visible for noble metals. The electrons below the Fermi level are excited to higher band by the efficient photons. This effect can be overcome by assuming that electrons in the metal are bound to the ionic atomic core and oscillate about it. Now we add a bound force to Eq. (3.1):

$$m\ddot{\boldsymbol{x}} + m\gamma\dot{\boldsymbol{x}} + m\omega_0^2\boldsymbol{x} = -\mathrm{e}\mathbf{E} \tag{3.4}$$

where ω_0 is the resonance frequency of a bound electron, which describes the interband transitions. In order to model the metals accurately, several equations of this form have to be solved. Finally, each critical equation leads to an oscillator term in the Lorentz model:

$$\varepsilon_m = \sum_{k=1}^{n} \frac{f_k\omega_p^2}{(\omega_k^2-\omega^2)-i\gamma_k\omega} \tag{3.5}$$

where k is the number of oscillators with frequency ω_k, strength f_k, and damping constant γ_k. In general, the combined Lorentz-Drude model is used to get an excellent fit to the experimental data:

$$\varepsilon_m = \varepsilon_\infty + \sum_{k=0}^{n} \frac{f_k\omega_p^2}{(\omega_k^2-\omega^2)-i\gamma_k\omega} \tag{3.5}$$

where ε_∞ is the optical dielectric constant at infinite frequency. For isotropic plasma-like metals, ε_∞ equals to 1. The Lorentz-Drude model parameters for gold and silver are listed below in Table 3-1. As shown in Fig. 3-3 and Fig. 3-4, the hybrid model closely meets with the experimental data at the visible and the near-UV.

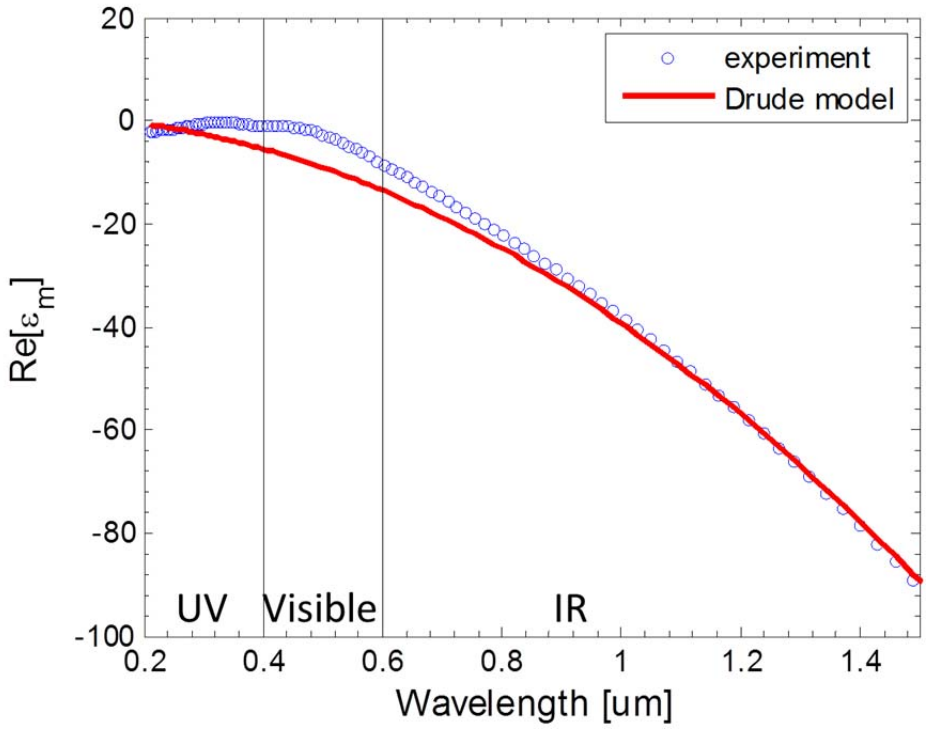

Fig. 3-1 The real part of ε(ω) for gold by Rakic et al. [37] and a Drude model fit.

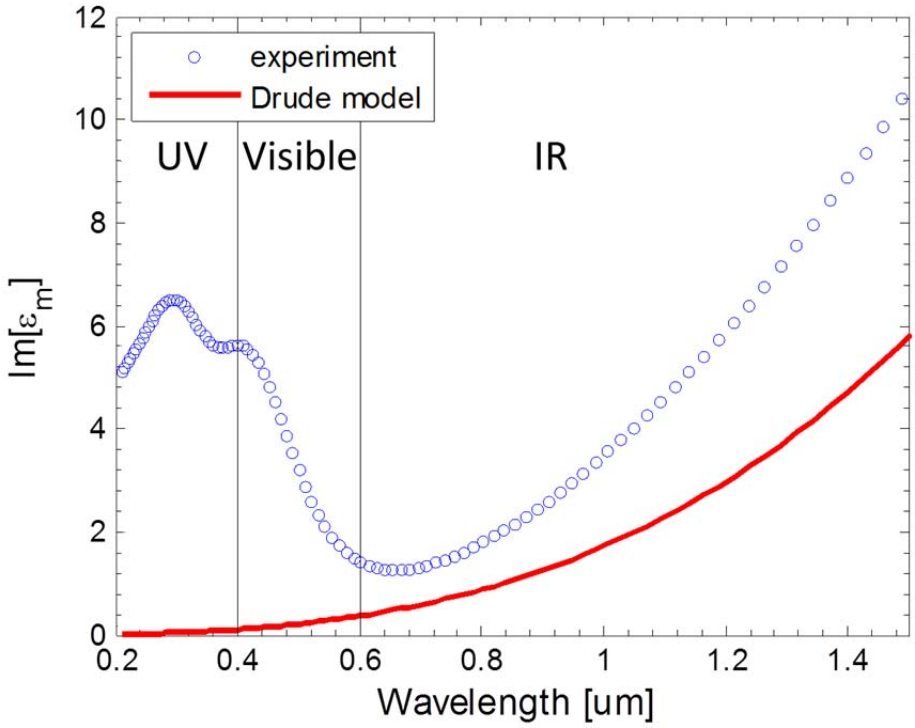

Fig. 3-2 The imaginary part of ε(ω) for gold by Rakic et al. [37] and a Drude model fit.

Parameters	Au	Ag
ω_p	9.03	9.01
$f_0 / \gamma_0 / \omega_0$	0.760 / 0.053 / 0.000	0.845 / 0.048 / 0.000
$f_1 / \gamma_1 / \omega_1$	0.024 / 0.241 / 0.415	0.065 / 3.886 / 0.816
$f_2 / \gamma_2 / \omega_2$	0.010 / 0.345 / 0.830	0.124 / 0.452 / 4.481
$f_3 / \gamma_3 / \omega_3$	0.071 / 0.870 / 2.969	0.011 / 0.065 / 8.185
$f_4 / \gamma_4 / \omega_4$	0.601 / 2.494 / 4.304	0.840 / 0.916 / 9.083
$f_5 / \gamma_5 / \omega_5$	4.384 / 2.214 / 13.32	5.646 / 2.419 / 20.29

Table 3-1 Lorentz-Drude model parameters for Au (gold) and Ag (silver) [37].

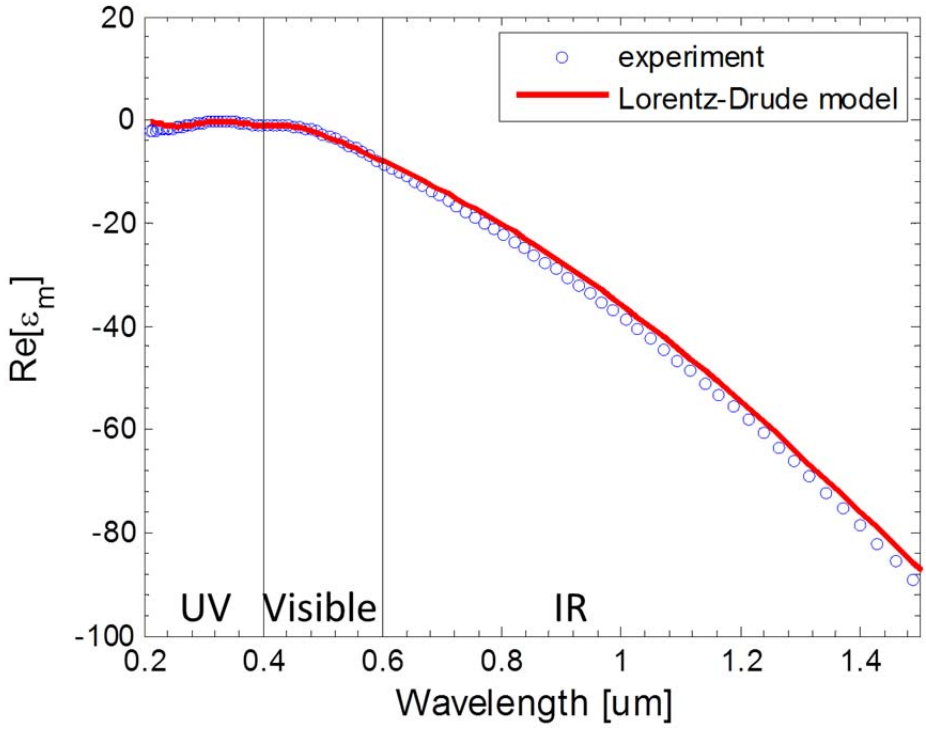

Fig. 3-3 The real part of ε(ω) for gold by Rakic et al. [37] and a Lorentz-Drude model fit.

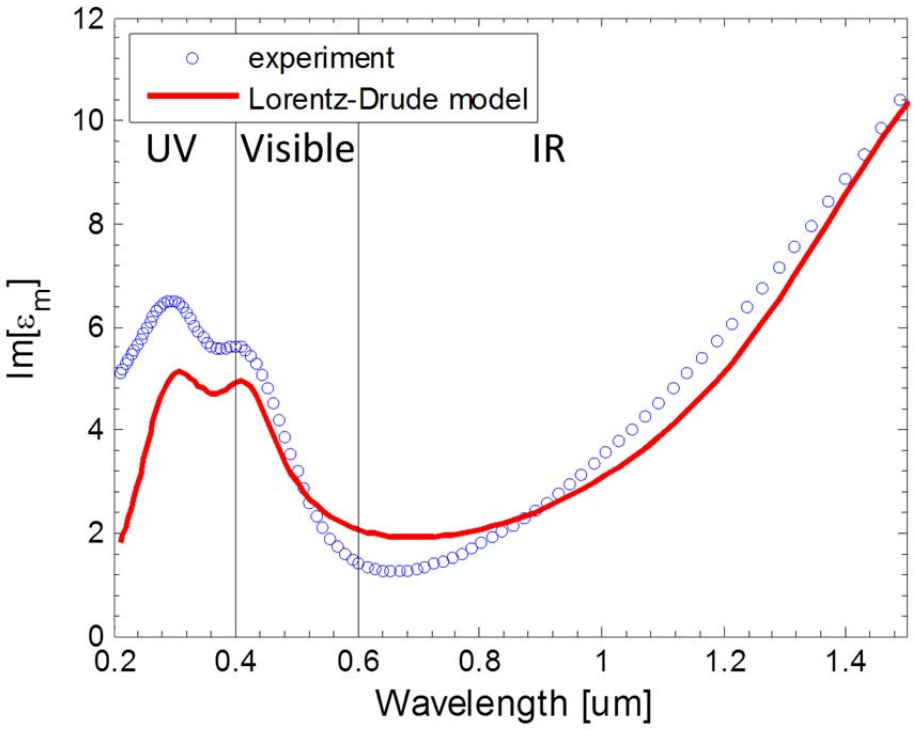

Fig. 3-4 The imaginary part of ε(ω) for gold by Rakic et al. [37] and a Lorentz-Drude model fit.

3.2 The theory of surface plasmon polaritons

One can consider a flat metal/dielectric interface as depicted in Fig. 3-5. The material for z > 0 is a non-absorbing dielectric with dielectric constant ε_d and the material for z < 0 is a metal with dielectric function $\varepsilon_m(\omega)$. For a transverse magnetic (TM) wave propagating along x-direction, the solutions of Maxwell's equations can be written as:

$$\begin{aligned} H_y(z) &= A_1 e^{i\beta x} e^{-k_1 z} \\ E_x(z) &= iA_1 \frac{1}{\omega \varepsilon_0 \varepsilon_d} k_1 e^{i\beta x} e^{-k_1 z} \\ E_z(z) &= -A_1 \frac{\beta}{\omega \varepsilon_0 \varepsilon_d} e^{i\beta x} e^{-k_1 z} \end{aligned} \tag{3.6}$$

for z > 0 and

$$\begin{aligned} H_y(z) &= A_2 e^{i\beta x} e^{k_2 z} \\ E_x(z) &= -iA_2 \frac{1}{\omega \varepsilon_0 \varepsilon_m} k_2 e^{i\beta x} e^{k_2 z} \\ E_z(z) &= -A_2 \frac{\beta}{\omega \varepsilon_0 \varepsilon_m} e^{i\beta x} e^{k_2 z} \end{aligned} \tag{3.7}$$

for z < 0. Continuity of H_y and E_x at z = 0 requires that $A_1 = A_2$ and

$$\frac{k_1}{k_2} = -\frac{\varepsilon_d}{\varepsilon_m} \tag{3.8}$$

For the both regions, Hy has to fulfill the wave equation:

$$\begin{aligned} k_1^2 &= \beta^2 - k_0^2 \varepsilon_d \\ k_2^2 &= \beta^2 - k_0^2 \varepsilon_m \end{aligned} \tag{3.9}$$

By combining Eq. (3.8) and (3.9), we obtain the dispersion relation of SPP propagating at the interface:

$$\beta = k_0 \sqrt{\frac{\varepsilon_d \varepsilon_m}{\varepsilon_d + \varepsilon_m}} \tag{3.10}$$

As for transverse electric (TE) modes, Continuity of H_x and E_y at z = 0 leads to the condition:

$$A_1(k_1 + k_2) = 0 \tag{3.11}$$

We know that $A_1 = 0$ because both Re [k_1] and Re [k_2] have to be positive. That is to say, no SPP exist for TE waves.

However, SPPs cannot be directly excited by the incident light on a flat metal/dielectric interface since the in-plane momentum of light on the dielectric side is always smaller than the propagation constant of SPPs. This fact can be clearly realized from Eq. (3.10) and Fig. 3-6. Actually, some designed arrangements as depicted in Fig. 3-7 can provide the adequate momentum of light for phase-matching to SPPs. Here we only explain about the principle of the popular Kretschmann configuration and the excitation by diffraction on gratings.

As shown in Fig. 3-7 (a), the Kretschmann configuration is a three-layer system in air. Usually, the incident light with wave vector k through the prism with higher dielectric constant ε reflects at the metal/prism interface at an angle θ larger than the critical angle for total internal reflection. This way, the in-plane momentum of incident light is enhanced by a factor of $\sqrt{\varepsilon}$:

$$k_x = k\sqrt{\varepsilon}\, sin\theta \tag{3.12}$$

Next, the attenuated fields tunnel through the metal film to the metal/air interface and is coupled to SPPs. As shown in Fig 3-6, the SPPs with propagation constants between the light lines of air and the prism can be excited.

Another familiar and unique method to achieve phase-matching to SPPs is to use diffraction on gratings as depicted in Fig. 3-7 (e). The condition of the phase-matching can be written as:

$$\boldsymbol{k_{sp}} = \boldsymbol{k}\, sin\theta \pm i\boldsymbol{P_x} \pm j\boldsymbol{P_y} \tag{3.13}$$

where $\boldsymbol{k_{sp}}$ is the wave vector of SPPs, $\boldsymbol{k}\ sin\theta$ is the in-plane component of the wave vector of the incident light, $\boldsymbol{P_x}$ and $\boldsymbol{P_y}$ are the reciprocal vectors of the gratings in the x- and y-direction restricted to integer multiples *i* and *j*, respectively. In the case of normal incidence, the in-plane momentum of light is equal to zero. And further, we assume that the periodic structures are spaced equally in the both directions with period *p*. By combining Eq. (10) and Eq. (3.13), we find the expression for the estimated resonant wavelength of SPPs:

$$\lambda = \frac{p}{\sqrt{i^2 + j^2}} \sqrt{\frac{\varepsilon_d \varepsilon_m}{\varepsilon_d + \varepsilon_m}} \tag{3.14}$$

Interestingly, the process can also reverse. SPPs propagating along the metal surface can be decoupled into radiate light by the gratings [9, 36].

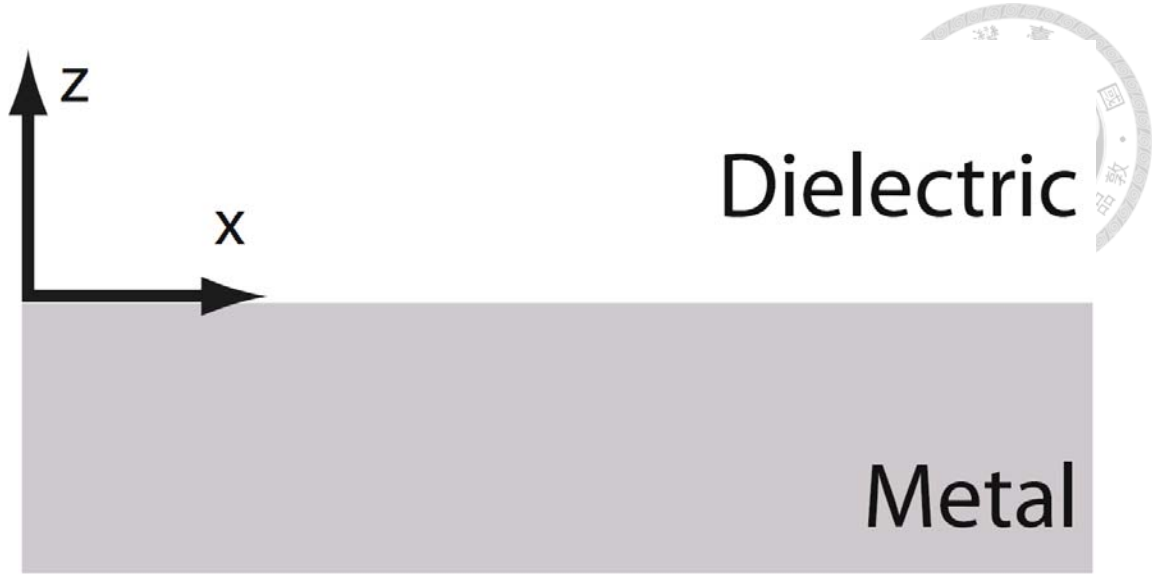

Fig. 3-5 Geometry for SPP propagation at the interface between a metal and a dielectric [36].

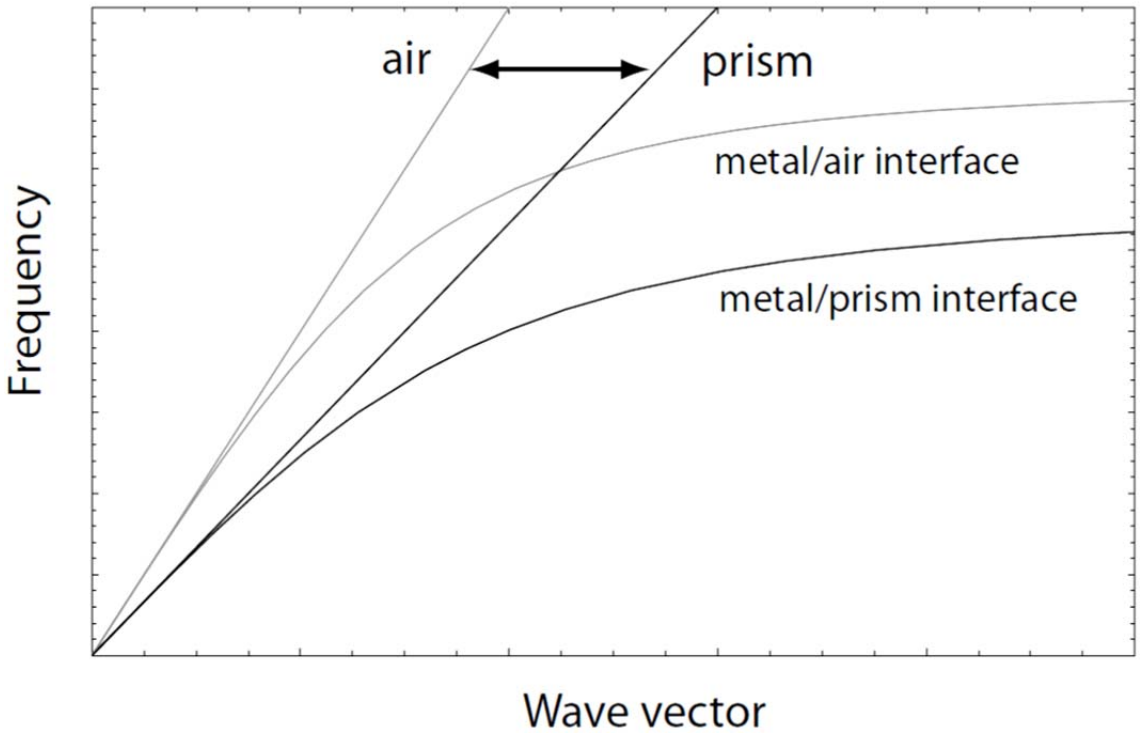

Fig. 3-6 Dispersion of SPPs at a metal/air interface and a metal/prism interface [36].

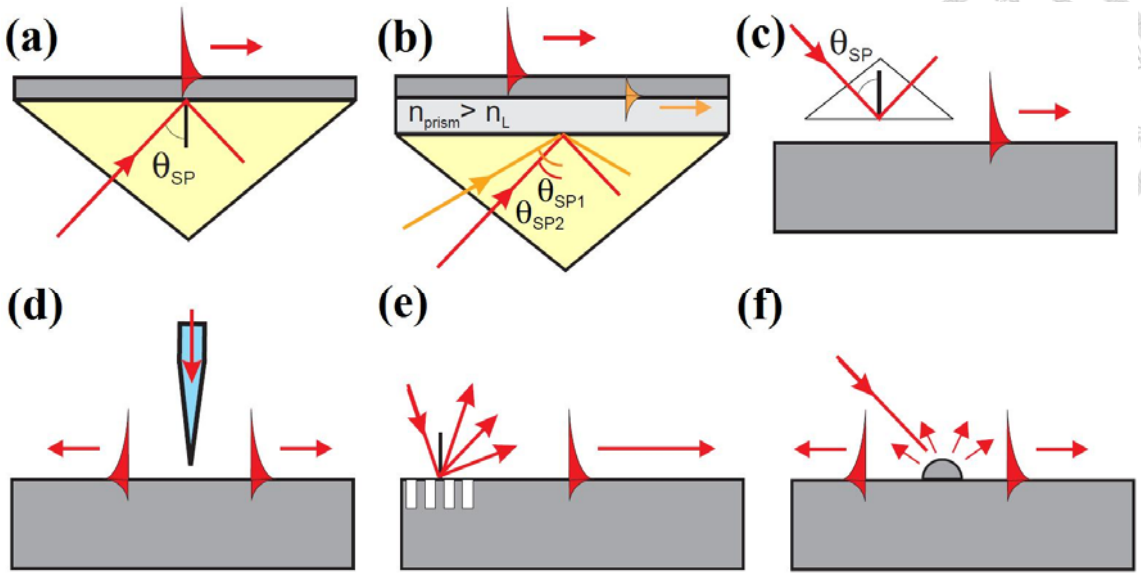

Fig. 3-7 SPP excitation configurations: (a) Kretschmann geometry, (b) two-layer Kretschmann geometry, (c) Otto geometry, (d)excitation with a SNOM probe, (e) diffraction on a grating, and (f) diffraction on surface features [6].

3.3 Finite-difference time-domain

In order to study the characteristics of the complex nanostructures on the SPR fiber probes, we need some numerical modeling methods to solve the complicated problems. We will introduce the basic theory of the FDTD method and how to build a model for our case by the software (FDTD solutions, ©Lumerical Solutions).

3.3.1 Introduction

The FDTD method was first proposed in 1966 by Yee for the analysis of the scattering of an electromagnetic pulse by a perfectly conducting cylinder [38]. It has become a useful tool in many problems such as electromagnetic waves, interference, radiation and surface plasmon modeling.

The basic theory of the FDTD method is based on the approximation of spatial and temporal derivatives by finite differences. For example, Eq. (3.15) is the central difference scheme of the derivative of function $f(x_0)$:

$$f'(x_0) = \frac{df(x_0)}{dx} \approx \frac{f(x_0 + \frac{\Delta x}{2}) - f(x_0 - \frac{\Delta x}{2})}{\Delta x} \tag{3.15}$$

Now we consider the Taylor series expansions of $f(x + \frac{\Delta x}{2})$ and $f(x - \frac{\Delta x}{2})$ at $x = 0$:

$$f(x + \frac{\Delta x}{2}) = f(x) + \frac{\Delta x}{2} f'(x) + \frac{1}{2}\left(\frac{\Delta x}{2}\right)^2 f''(x) + \cdots \tag{3.16}$$

$$f(x - \frac{\Delta x}{2}) = f(x) - \frac{\Delta x}{2} f'(x) + \frac{1}{2}\left(\frac{\Delta x}{2}\right)^2 f''(x) + \cdots \tag{3.17}$$

and take the difference of Eq. (3.16) and Eq. (3.17). By arranging the result, we obtain:

$$f'(x)=\frac{f(x+\frac{\Delta x}{2})-f(x-\frac{\Delta x}{2})}{\Delta x}-\frac{1}{6}\left(\frac{\Delta x}{2}\right)^2 f'''(x)+\cdots \quad (3.18)$$

The first term on the right side of Eq. (3.18) is the central difference approximation to $f'(x)$ and the other terms are the error between the approximation and the exact value. The error is proportional to the square of the finite difference Δx so the central difference scheme is considered second order accurate, which is sufficiently accurate to use in most of the practical electromagnetic modeling.

In the FDTD method, Yee just converted Maxwell's time-dependent equations into finite-difference equations. Fig. 3-8 shows the Yee cell, which definite the positions of the electric and magnetic field vector components on a cubic unit cell. The E-components are in the middle of the edges and the H-components are in the middle of the faces. This special configuration depicts Faraday's Law and Ampere's Law. It should be noticed that the components are also offset in time. Then, the equations are solved in a time-marching sequence by alternately calculating the electric and the magnetic fields in an interlaced spatial grid. Six new values of the components are calculated at every cell as time iterates.

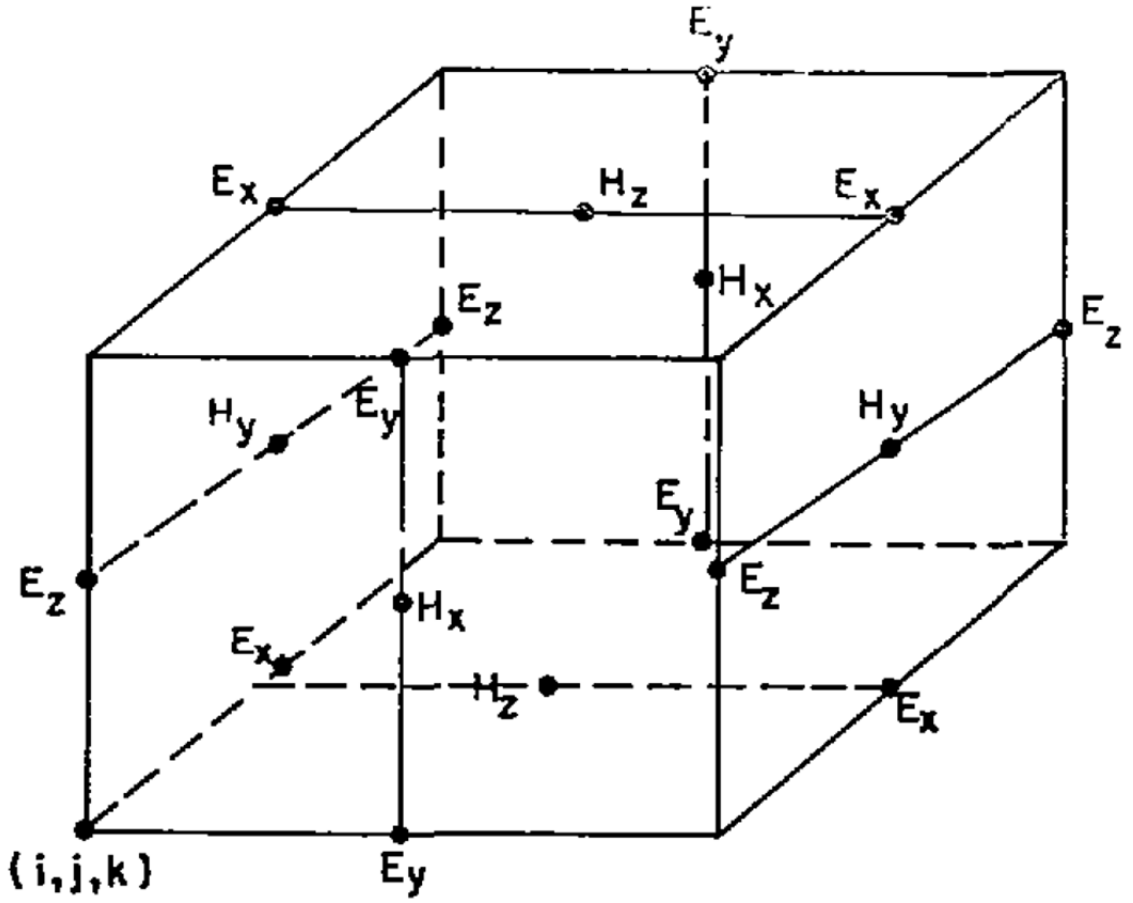

Fig. 3-8 Positions of the electric and magnetic field vector components on a cubic unit cell of the Yee space lattice.

3.3.2 Model building by the FDTD Solutions of Lumerical Solutions

The FDTD Solutions is a commercially available software. It provides a simple operation for model building and a fast and state-of-the-art method for solving 3D Maxwell's equations.

First we have to define the geometries of the nanostructures for modeling. In Section 2.5, the period and the diameter of the holes were measured to be 506 nm and 261 nm, but the information of the depth of the holes was not acquired yet. The 3D information of the nanohole array was acquired by the atomic force microscope (AFM) in a 3 μm × 3 μm area as shown in Fig. 3-9 (a) and the profile was shown in Fig. 3-9

(b), which showed a vertical distance of about 100 nm between the top and the bottom of the hole. Therefore, we use the structures designed with the parameters shown in Fig. 3-10. The thickness of the structures is assumed to be uniform in the gold deposition process.

For time-effectiveness and economization on the computer memory, the complete structures are not used for modeling so the simplification of the model for simulation by some assumptions and conditions is needed. Fortunately, the periodicity of the structures helps us reduce the complete structures to only a repeatable unit cell. Fig. 3-11 shows the concept of the model for the simulation of periodic structures. Periodic boundary conditions are applied on the sides of the model. The normal incident light is assumed as a plane wave to approximate the light propagating in MMF [39-41]. Detector 1 and detector 2 are placed to record the reflection spectrum and the transmission spectrum, respectively.

The finished model built by FDTD Solutions is shown in Fig. 3-12. Firstly, the geometries of the structures can be built according to Fig. 3-10. The structure of the 3D nanohole is established by a slab (area $P \times P$, thickness t) and a cylinder (diameter $d + 2 \times t$, height h) and the two objects are then etched by a smaller cylinder (diameter d, height h) offset by t. Suitable materials are chose for the substrate (n = 1.45) and the 3D nanohole (CRC gold [42]). Secondly, an appropriate region for FDTD simulation is defined and the background index is chose to be 1 for the air surroundings. As mentioned, periodic boundary conditions are applied on the sides of the region and perfect match layers (PML) are applied on the top and the bottom for absorptions of the reflection at the boundaries [43]. The mesh size of the model is set 1 nm in the three directions. Thirdly, a source is put at the bottom of the simulated region. The source is a normal incident plane wave and the wavelength is swept from 400 nm to 1000 nm with

step 5 nm, which is sufficient to analyze the spectrum. Detectors are also put at the top and the bottom.

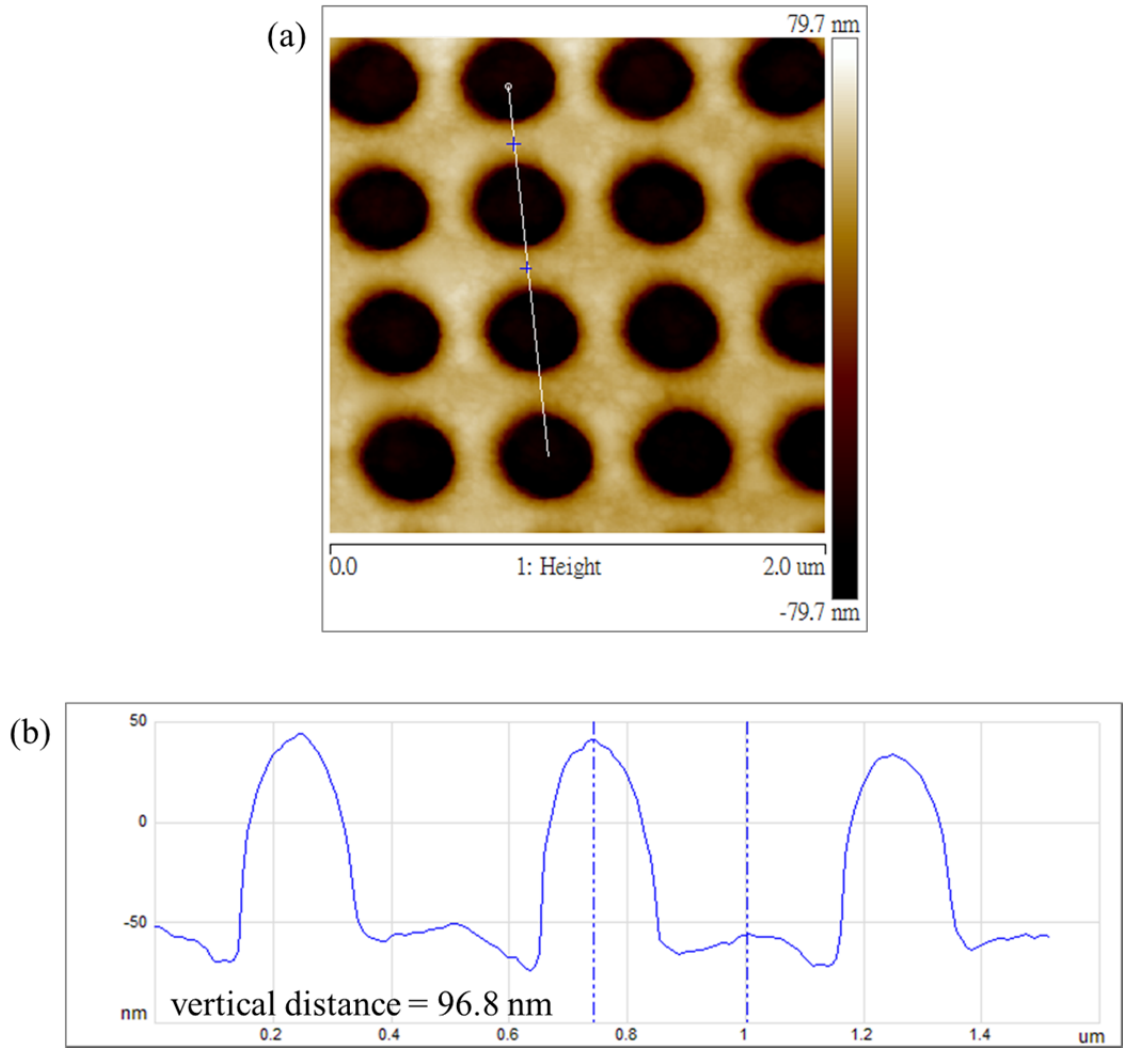

Fig. 3-9 (a) AFM photo of the nanohole array fabricated by nTP on glass substrate; (b) the profile data of the section cut in (a) and the vertical distance between the section is 96.8 nm.

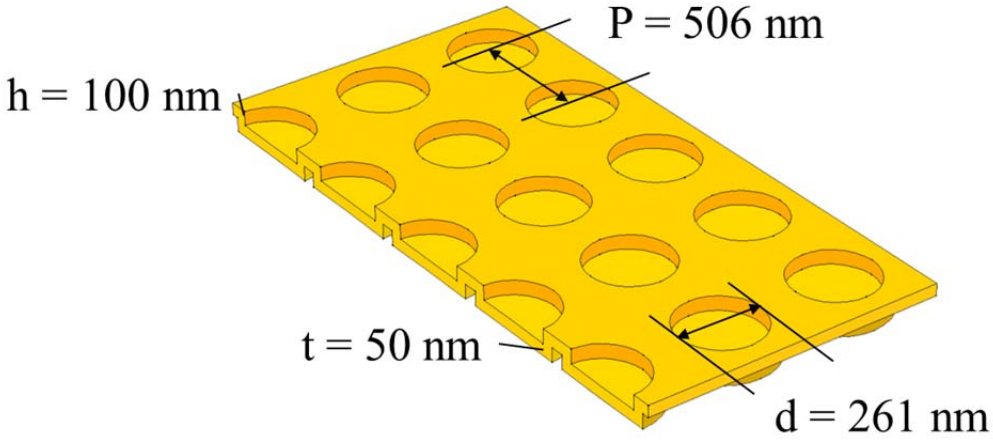

Fig. 3-10 Illustration of the 3D nanohole array. The parameters are: Period P = 506nm, diameter d = 261 nm, depth h = 100 nm and film thickness t = 50 nm.

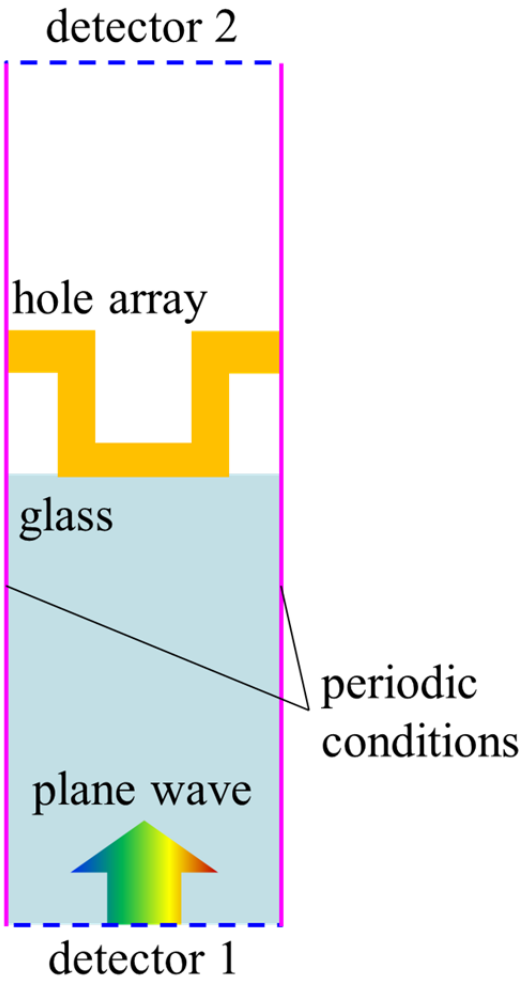

Fig. 3-11 Schematic diagram of a unit cell for the simulation of periodic structures.

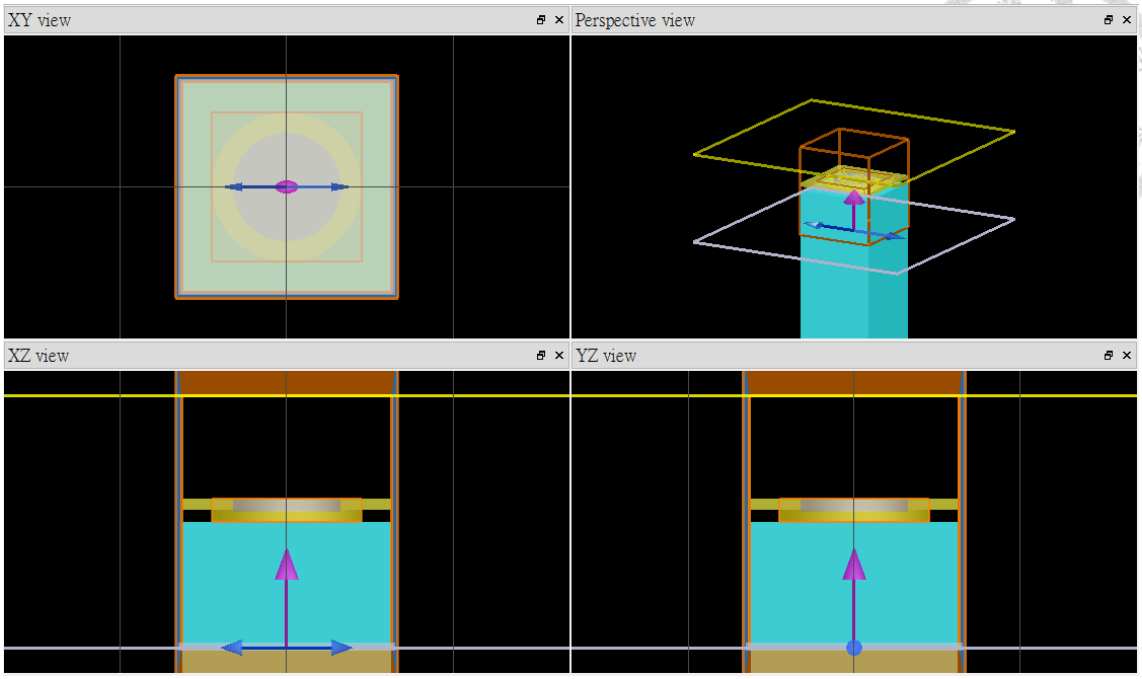

Fig. 3-12 Screenshot of the model built by FDTD Solutions.

3.4 Finite element method

We have introduced the FDTD method in the last section. However, the method shows bad performance in the mesh of the structure. That is, the cubic unit cells in the FDTD method cannot represent the original structures and the calculated fields perfectly. Here we will introduce the concept of the FEM method and how to build a model for our case by the powerful software (RF Module, ©Comsol Multiphysics).

3.4.1 Introduction

The finite element method (FEM) or called finite element analysis (FEA) is a method for obtaining a numeric approximation to a governing differential equation. Actually, many researchers developed the method in different period. In 1965, Feng proposed a systematic numerical method for solving partial differential equations. [44]. It is believed that he established the basis. Since then, driven by increasingly powerful computers, FEM has been continually developed for a broad range of scientific and engineering problems.

Each element contains some number of points referred to as nodes. For example, a 3D problem may use tetrahedrons as elements, and each element will have at least four nodes, which are the vertex points of the tetrahedron. Other geometric figures such as hexahedrons are adoptable at the same time if necessary. Therefore, one can write down the governing differential equations for each element. According to the theory of FEM, the differential equations can be converted into a set of finite linear algebraic equations. One gets the solutions from the model approximated to the original structure if the set of the equations are solved.

3.4.2 Model building by the RF Module of Comsol Multiphysics

Comsol Multiphysics is also a commercially available software. It provides a capability of complex mesh generation, and a wide array of numeric solvers and post-processing tools. We used Radio Frequency (RF) Module in this study for electromagnetic simulations. The parameters of the structure and the concept of the model are the same as those described in section 3.3.2.

The finished model built by Comsol Multiphysics is shown in Fig. 3-13. Firstly, the geometries of the structures can be built according to the steps in section 3.3.2. Different from the FDTD Solutions, the geometries of the structures define the region of the simulation so the blocks should be built for the surroundings and PMLs. Suitable materials are chose for the substrate ($\varepsilon = 1.45^2$) and the surroundings ($\varepsilon = 1^2$). Secondly, another wave equation has to be established in order to set the Lorentz-Drude model parameters for the gold nanohole. Periodic boundary conditions are applied on the sides of the region and PMLs are applied on the top and the bottom blocks. The maximum and minimum mesh sizes are set 53 nm and 1.6 nm. Thirdly, Port 1 is put at the substrate/PML interface. The port serves as a source and a detector for reflection spectrum at the same time. The source is a normal incident plane wave and the wavelength is swept from 400 nm to 1000 nm with step 5 nm. Port 2 is put at the surroundings/PML interface for transmission spectrum only.

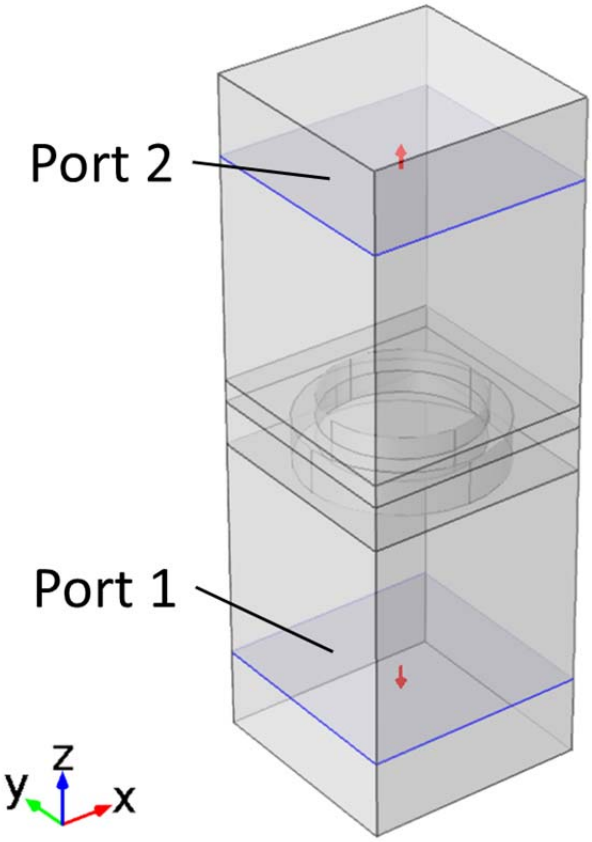

Fig. 3-13 Screenshot of the model built by Comsol Multiphysics 5.1.

3.5 Results and discussions of the simulation

The spectra simulated by FEM and FDTD method are shown in Fig. 3-14. The trends of the spectra obtained by using the both methods look similar. However, there are some slight differences between the profiles of the spectra, which may be caused from the different methods, the settings of the models and the gold model used. It can be obviously seen that there is a sharp dip in the reflection spectra and two peaks in the transmission spectra. The sharp dip results from the coupling of the incident light to the surface plasmons excited at the substrate side. In the transmission spectra, it should be noticed that the peak near 500 nm in the transmission spectra is the characteristic of the gold film, and is not related to any nanostructure or surface plasmons properties [9, 45]. The other peak results from the decoupling of the surface plasmons excited at the surroundings side, which can be predicted by Eq. (3.14). Nevertheless, we can just estimate the positions where SPRs take place roughly because of the complex nanostructures. For example, the peak near 600 nm in the transmission spectra can be attributed to the (1, 0) scattering order with air as the medium but Eq. (3.14) predicts that the resonance will take place at about 550 nm. To further check the resonant positions more accurately, some parameters are tested for the spectra and the electric field distributions near the gold nanohole are examined. The spectra are simulated by FDTD method for time-effectiveness, and the electric field distributions are simulated by FEM for finer display.

The parameter, period, is first tested. According to Eq. (3.14), the resonant wavelength shifts to the red as the period extend. Fig. 3-15 shows the simulated spectra of the model with two different periods. Only the dip at 865 nm in the reflection spectrum and the peak at 580 nm shift to 940 nm and 660 nm respectively as period

extends from 507 nm to 600 nm. The electric field distributions near the gold structure can also verify the resonant wavelengths. In Fig. 3-16, the intensity of the electric field is greater and more concentrated at the dip (890 nm) than at other wavelengths in the reflection spectrum. The resonant wavelength in the transmission spectrum is verified as shown in Fig. 3-17. Similarly, the electric fields concentrate at the peak (595 nm) rather than other wavelengths. A much larger difference can be observed in Fig. 3-17 (b). As mentioned, Fig. 3-18 reveals that the peak near 500 nm does not have any surface plasmons properties.

Next, the parameter, refractive index (RI) of the surroundings, n_s, is tested. Actually, there is an issue, which should be noticed and is depicted in Fig. 3-19. Due to the 3D gold structures, gaps exist between the structures and the substrate. Therefore, water or other solutions cannot flow into the gaps unless the structures are leaky. To study the situation, RI of the gap region, n_{gap}, is set to be 1 for the intact structures or n_s for the leaky structures, and the simulated spectra are shown in Fig. 3-20 and Fig. 3-21. In the both cases, the transmission peak shifts to the red. In contrast, the reflection spectrum almost remains the same as the surroundings changed from $n_s = 1$ to $n_s = 1.33$ in the former case. That is, if the 3D gold structures on the fiber are intact, the reflection based SPR fiber probe is not suitable for sensing. In the latter case, the reflection dip shows only an about 30 nm shift. The shift is much smaller than that in the transmission spectrum because of the smaller gap region relative to the surroundings. Fig. 3-22 and Fig. 3-23 show the reflection and the transmission spectra as n_s extends further. The sensitivities are roughly estimated to be ~ 160 nm/RIU and ~ 400 nm/RIU in the range, $n_s = 1.33 - 1.39$, respectively.

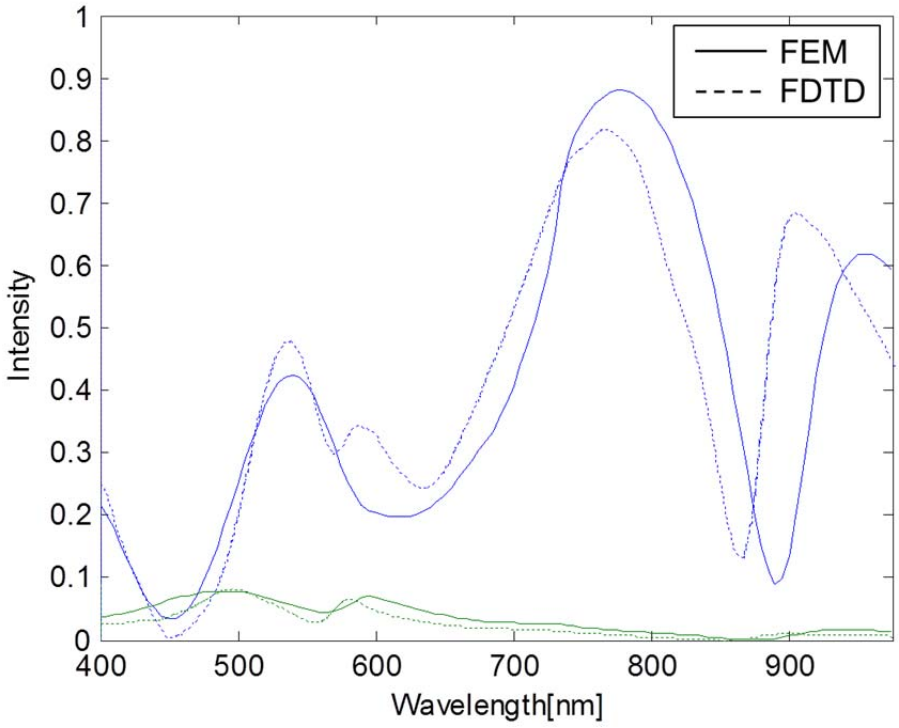

Fig. 3-14 Simulated reflection (blue lines) and transmission (green lines) spectra by FEM and FDTD method.

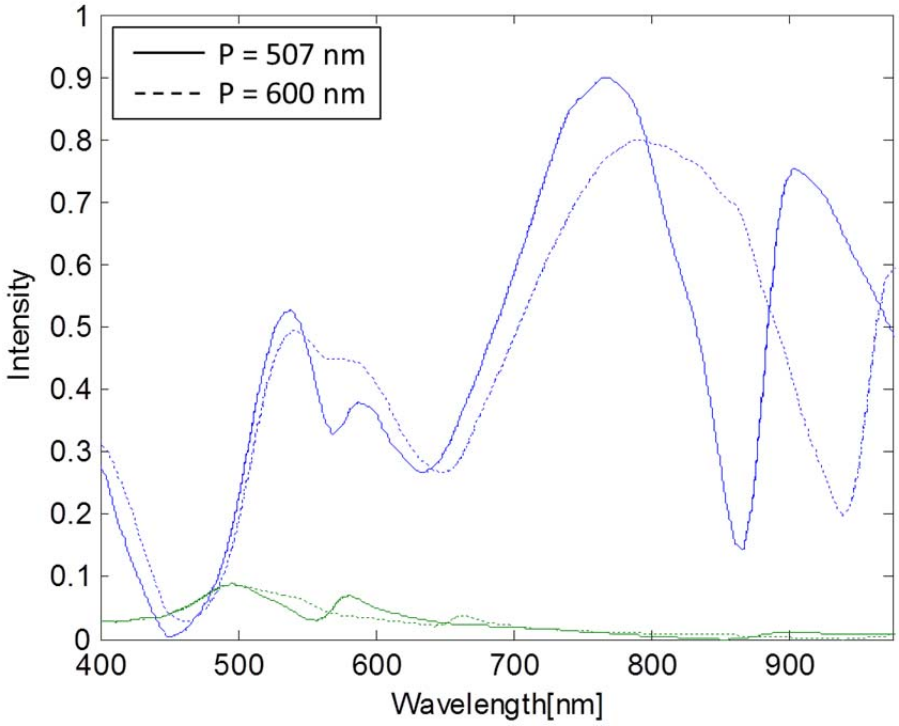

Fig. 3-15 Simulated spectra of the model with period P = 507 nm and P = 600 nm.

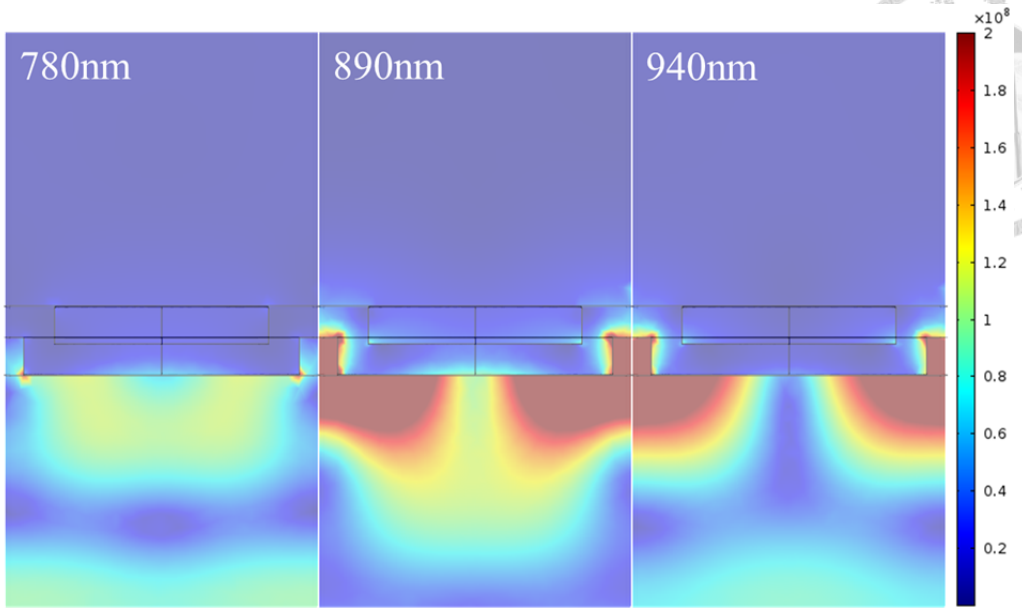

Fig. 3-16 Simulated electric field distributions at the peaks (780 nm and 940 nm) and the dip (890 nm) in the reflection spectrum of the model with surroundings of $n_s = 1$.

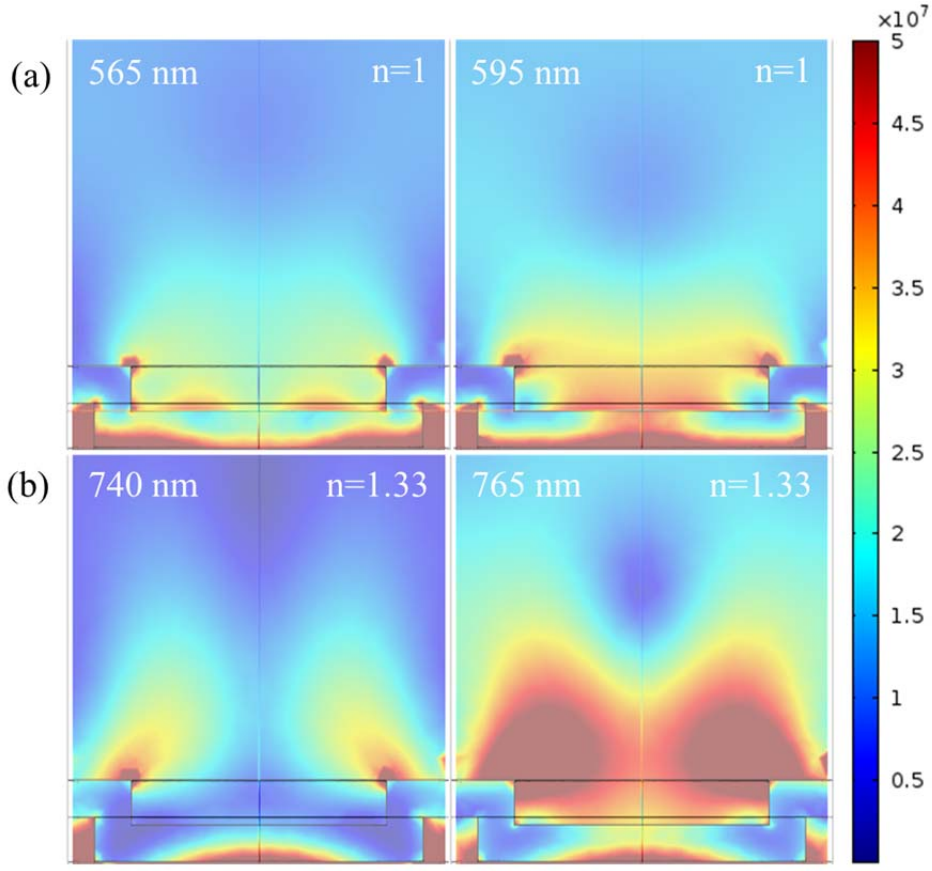

Fig. 3-17 Simulated electric field distributions at the dip and the peak in the transmission spectrum of the model with surroundings of (a) $n_s = 1$ and (b) $n_s = 1.33$.

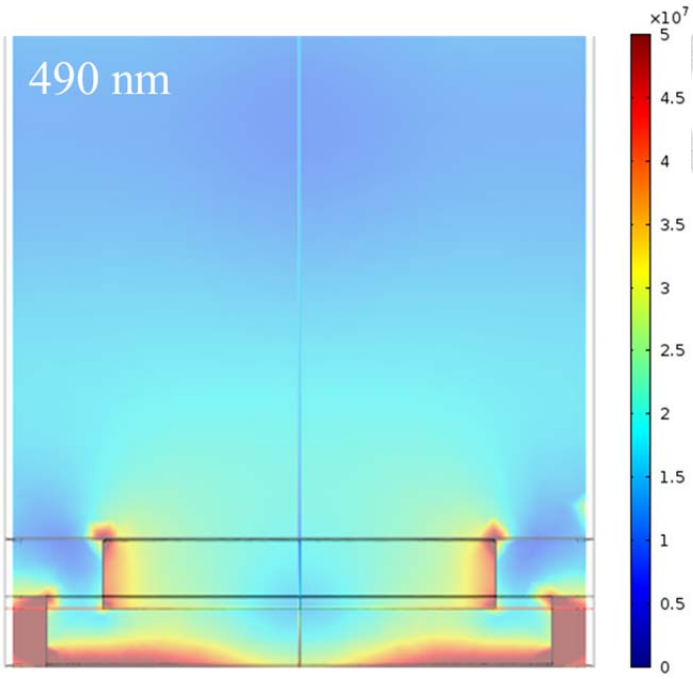

Fig. 3-18 Simulated electric field distribution at the peak (490 nm).

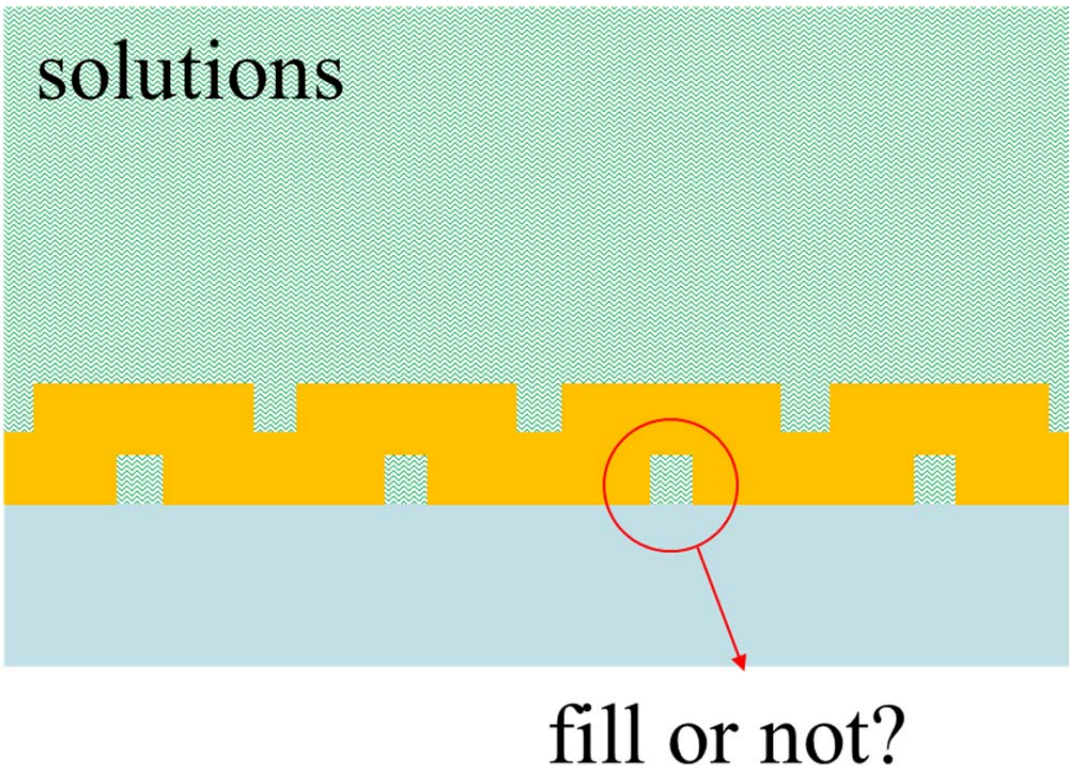

Fig. 3-19 Illustration of the issue of filling the gaps between the nanostructures and the substrate in the case of solution surroundings.

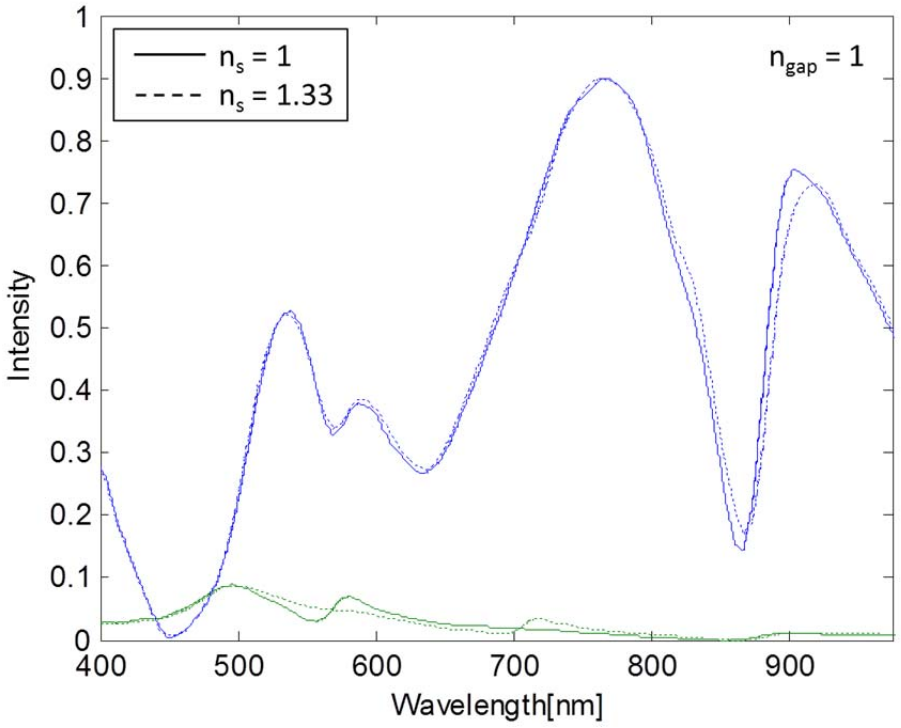

Fig. 3-20 Simulated spectra of the model with surroundings of n_s and $n_{gap} = 1$.

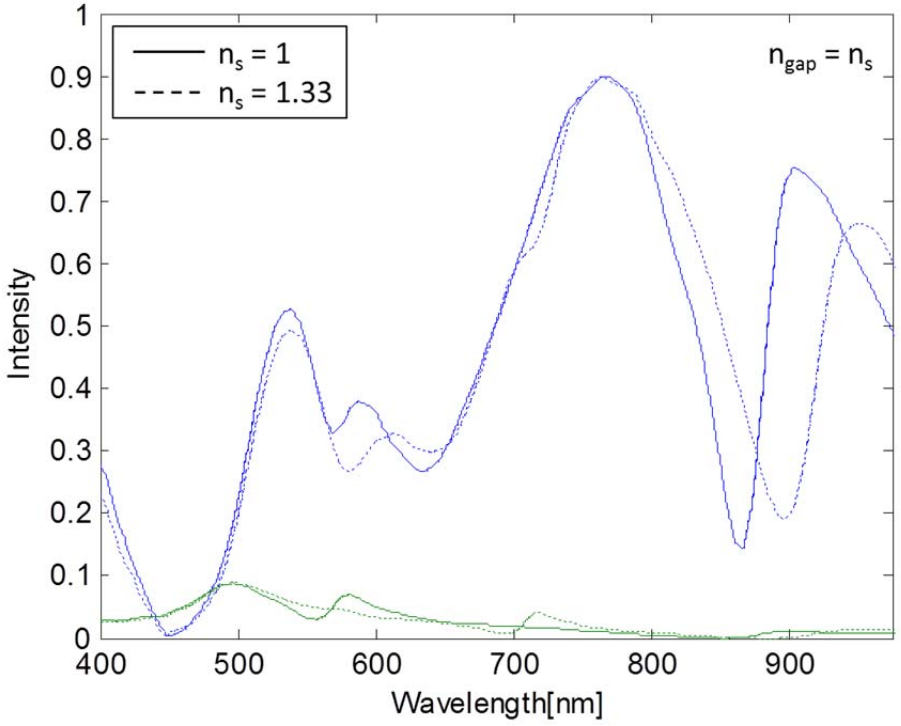

Fig. 3-21 Simulated spectra of the model with surroundings of n_s and $n_{gap} = n_s$.

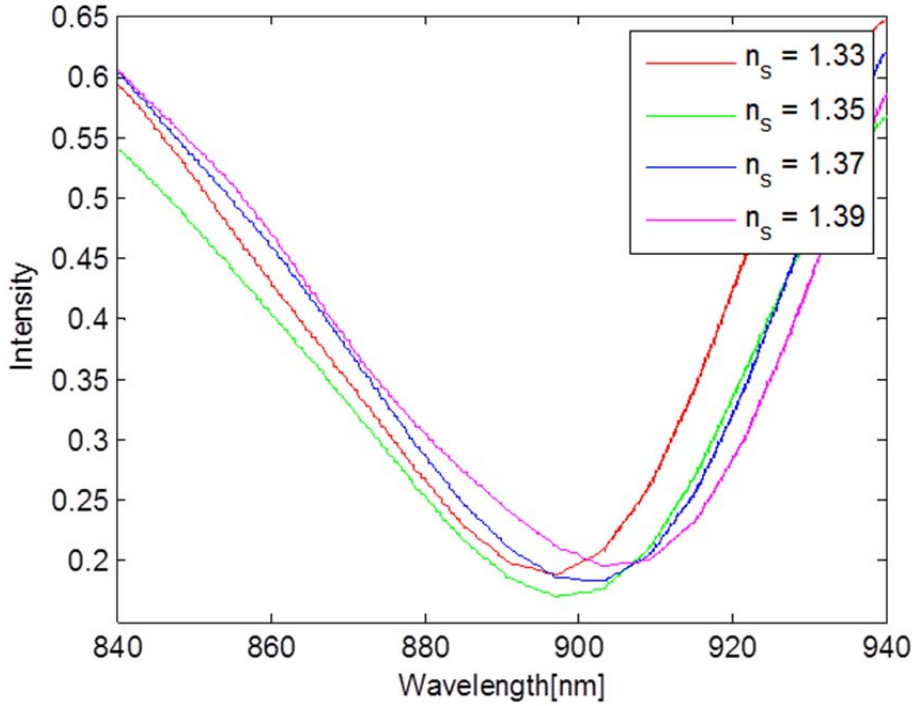

Fig. 3-22 Simulated reflection spectra of the model with surroundings of n_s = 1.33 to 1.39 for the leaky gold structures.

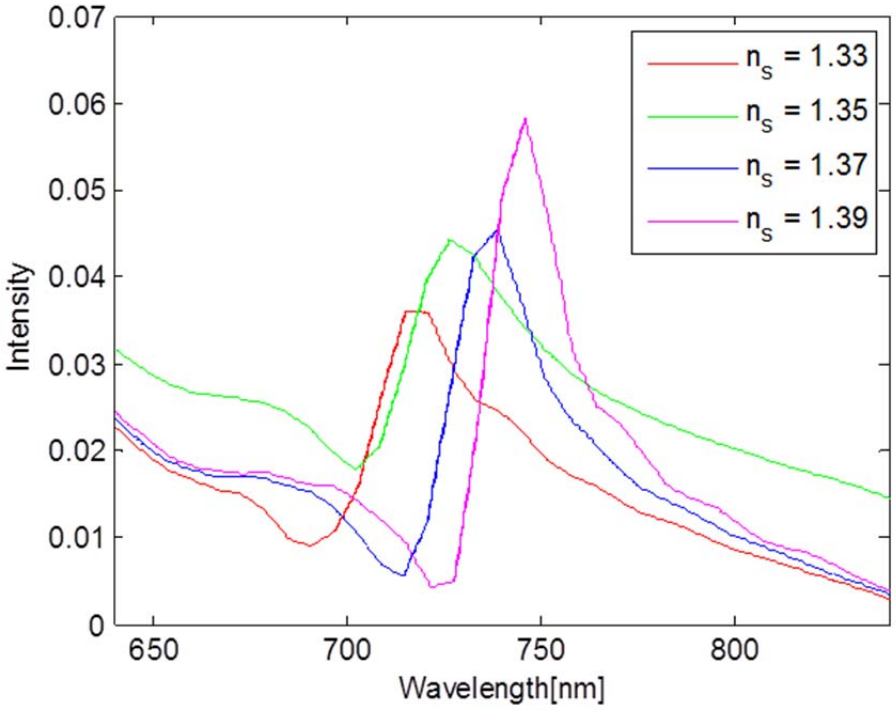

Fig. 3-23 Simulated transmission spectra of the model with surroundings of n_s = 1.33 to 1.39.

Chapter 4 Measurement of SPR Fiber Probes with 3D Metallic Gratings

4.1 Basic experimental set-up

To measure the optical characteristics of the SPR fiber probes, the measurement system was set up as shown in Fig. 4-1. First the diffuse light emitted from a white light source was coupled into a 62.5/125 μm MMF at end A by a lens. In the reflection type configuration (see Fig. 4-1 (a)), the input fiber at end A and a SPR fiber probe at end B were connected to the input port (Port 1) and the output port (Port 2) of a 50/50 ratio 1×2 coupler. A part of the transmitted light would reflect back to Port 3 and the reflection spectrum was analyzed by the optical spectrum analyzer (OSA), which had a wavelength resolution of 0.5 nm in the measurement wavelength range, 350-1750 nm. As for the transmission type configuration (see Fig. 4-1 (b)), the input fiber at end A was directly connected to a SPR fiber probe at end B, and the emergent light was collected by a MMF with a 400 core at end C and analyzed by OSA.

For the experiment of refractive index (RI) sensing, the glucose solutions with different concentrations were used as the surroundings in order to get a wide range of RIs from 1.33 to 1.39. Table 4-1 shows the concentrations expressed in mass fraction and the corresponding RIs, which are measured ten times for each concentration, and then averaged. The averaged results show small standard deviations.

To show the capability to do biosensing with the SPR fiber probes, the immobilization of bovine serum albumin (BSA) with the concentration of 5 μg/ml and the measurement of the corresponding wavelength shifts of the SPR positions were

demonstrated. The information of the materials used in biosensing is listed in Table 4-2. Phosphate-buffered saline (PBS) solutions were used as the buffer solutions for the preparation and washing of the materials except 11-mercaptoundecanoic acid (11-MUA).

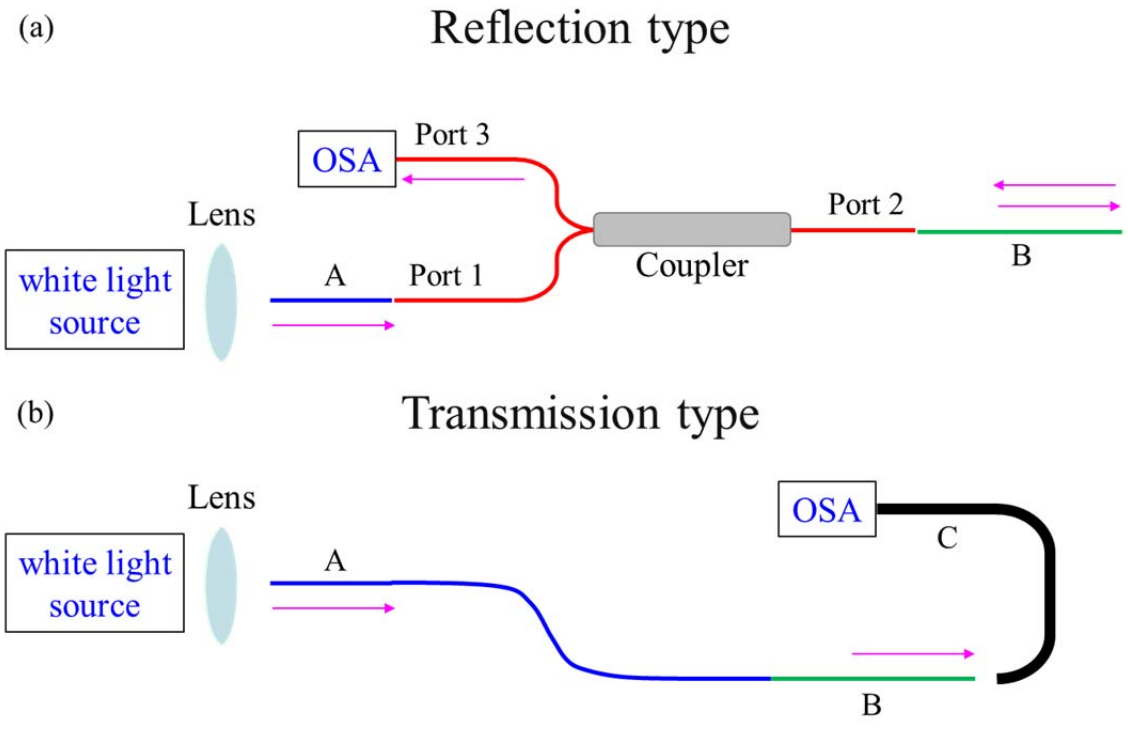

Fig. 4-1 Schematic diagram of the measurement set-up in (a) reflection type and (b) transmission type configuration. The set-up included an input 62.5/125 μm MMF at end A, a SPR fiber probe at end B, and a 400 μm core MMF at end C.

Concentration (w/w %)	Refractive Index (avg.)	Standard Deviation
0	1.3332	0.000050
5	1.3407	0.000504
11	1.3491	0.000393
18	1.3605	0.000497
24	1.3703	0.000438
30	1.3803	0.000354
35	1.3897	0.000467

Table 4-1 Information of the refractive indices for the glucose solutions with different concentrations.

Materials	Concentration	Prescription
11-mercaptoundecanoic acid (11-MUA)	2.18 mg/ml	0.01 g in 4.58 ml ethanol
1-(3-dimethylaminopropyl)-3-ethylcarbodiimide hydrochloride (EDC)	19.2 mg/ml	0.05 g in 2.6 ml PBS
N-hydroxysuccinimide (NHS)	2.87 mg/ml	7.5 mg in 2.6 ml PBS
bovine serum albumin (BSA)	5 μg/ml	2 mg in 40 ml PBS (1), then take 200 μl of (1) and add it into 2 ml PBS

Table 4-2 Information of the materials used in biosensing.

4.2 Optical characteristics of the SPR fiber probes

The comparisons between the simulated and the experimental results are shown in Fig. 4-2 and Fig. 4-3. The experimental spectra quite match the simulated spectra especially in the transmission and the last half of the reflection results. The small difference between the simulated and the experimental results and an about 10 nm deviation of the resonant positions may be caused from the imperfections in the gold nanohole array structures on the SPR fiber probes. Reflection and transmission spectra of the five fabricated SPR fiber probes are shown in Fig. 4-4 and Fig. 4-5 to display their repeatability. Some probes show relatively more noise and weaker intensity in the spectra. Nevertheless, the trends are similar, and all the resonant dips and the resonant peaks in the spectra can be identified clearly. The results indicate the quite good repeatability of the SPR fiber probes and show the potential for mass production.

Next, for the experiment of RI sensing, the probes were directly immersed in the glucose solutions with different concentrations listed in Table 4-1. After each measurement, the probes were flushed gently. The spectra near the resonant positions were fit by triangular moving average (TMA) method to remove the noise and smooth the curves, then the peak or dip values were picked out. TMA is simply a double-smoothed simple moving average (SMA) and usually used to get a trend of the data. To be closed to the original data and avoid serious signal distortion, the window size, the number of the data points for averaging every time, was chosen to be 20 for TMA. The smoothed reflection spectra of the probes exposed in air and immersed in the glucose solutions are shown in Fig. 4-6. As predicted in Section 3.5, because of the intact structures, the change of the surroundings could not be sensed by the field of the surface plasmons. Therefore, the resonant dip kept still even if the large difference

between the RIs of air and the solutions. However, it was also found that the small shifts of the dip occurred due to few leaky structures on some probes as shown in Fig. 4-7. The obvious shifts of the resonant peak in the transmission spectra are shown in Fig. 4-8. The spectrum of the probe exposed in air is not shown in the figure for the clear display of the peaks in the range of 720-790 nm. By picking out the peak values, the total shift was calculated to be about 17 nm. To estimate the sensitivity of the probe, the peaks in Fig. 4-8 were recorded and well fit by a straight line plotted in Fig. 4-9. The slope of the linear fit is 265.71 nm/RIU and it corresponds to the sensitivity of the probe. Though the sensitivity was not as high as that expected value in Section 3.5, the two values were in the same order. The reason of the big difference between the sensitivities estimated by the simulation and the experiment was owing to the difference between the parameters used in the model and the real conditions. For the specific sharp edges in the simulated models, strong electric fields or localized surface plasmon resonance (LSPR), which was not introduced here, could take place. In addition, the solutions might fill the nanoholes imperfectly in the experiment and then the local RI was lowered. Interestingly, we discovered that the dip beside the resonant peak also shifted to the red and the larger total shift of the dip was about 27 nm as shown in Fig. 4-10. In the same way, the obtained sensitivity of the dip was 388.57 nm/RIU. The data points and the linear fit are plotted in Fig. 4-11.

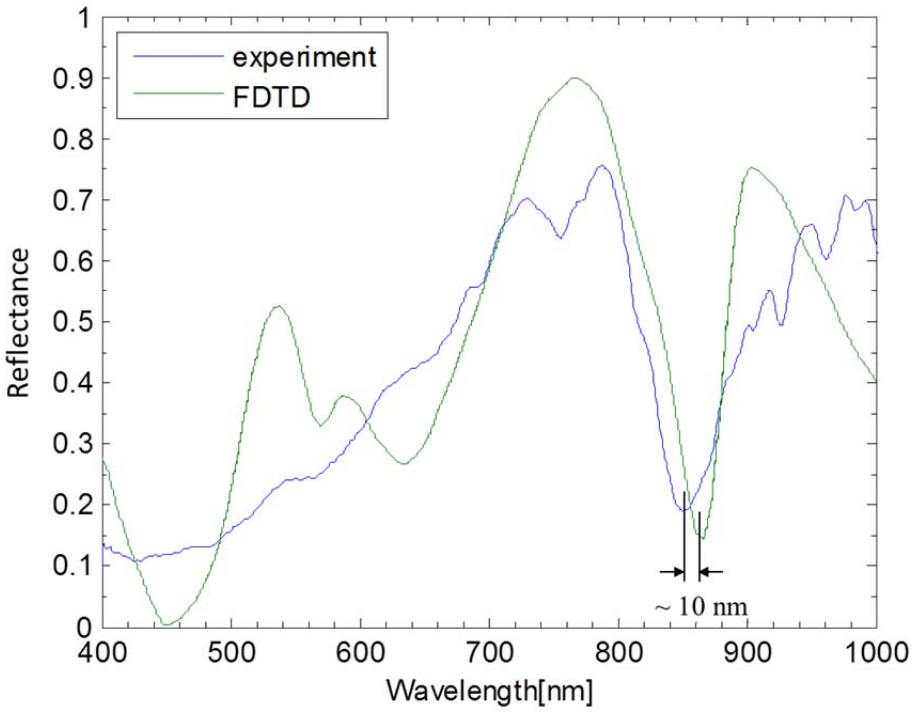

Fig. 4-2 FDTD simulated (green line) and experimental (blue line) reflection spectra of the SPR fiber probe in air.

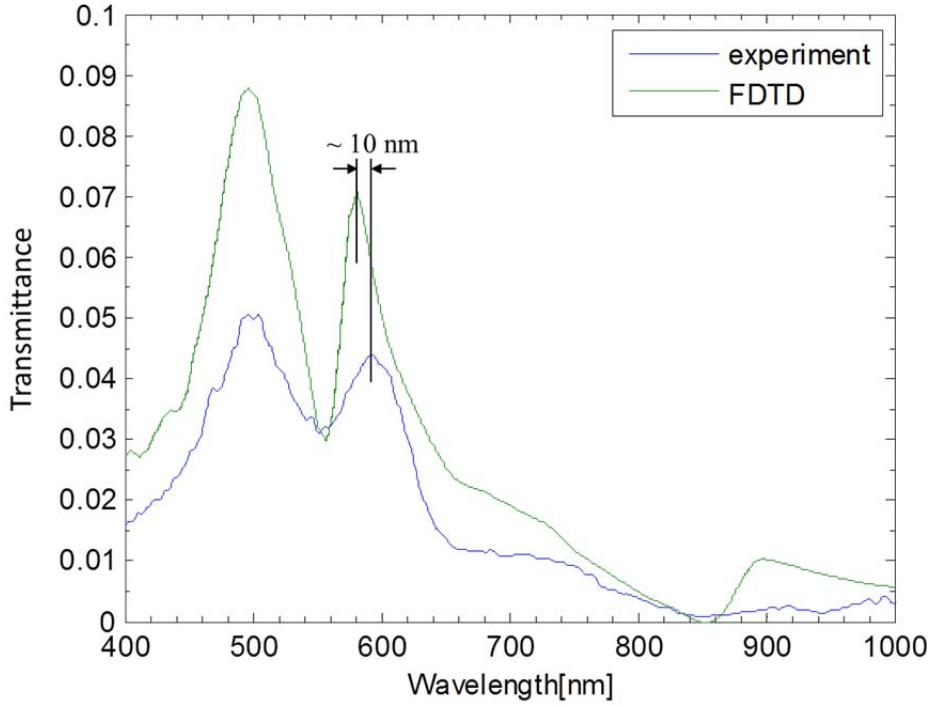

Fig. 4-3 FDTD simulated (green line) and experimental (blue line) transmission spectra of the SPR fiber probe in air.

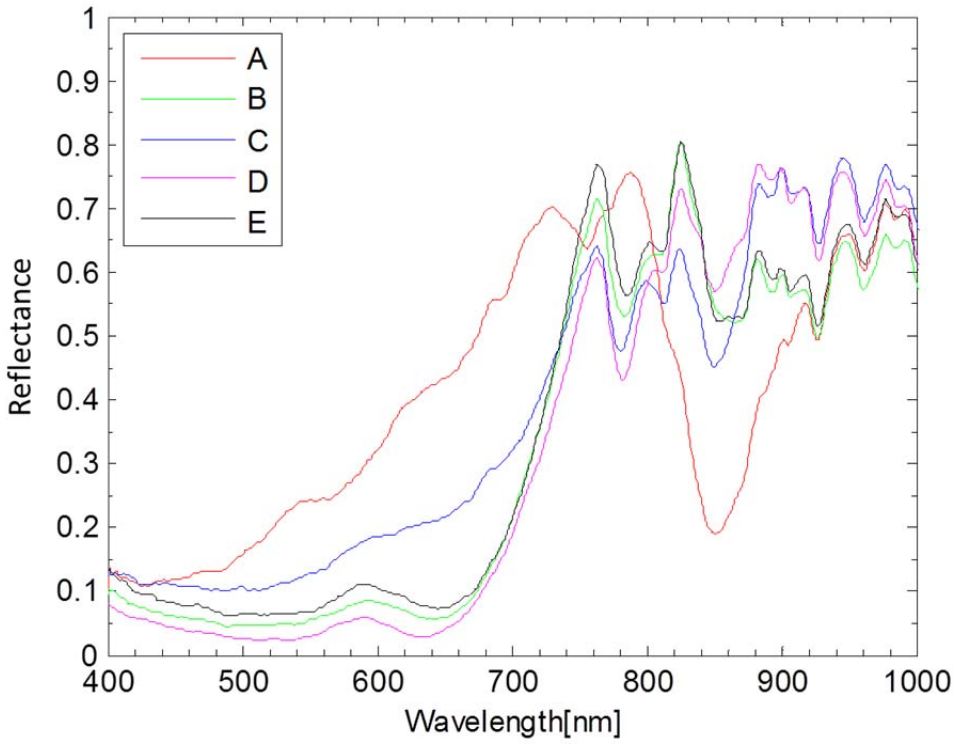

Fig. 4-4　Five reflection spectra of the fabricated SPR fiber probes in air.

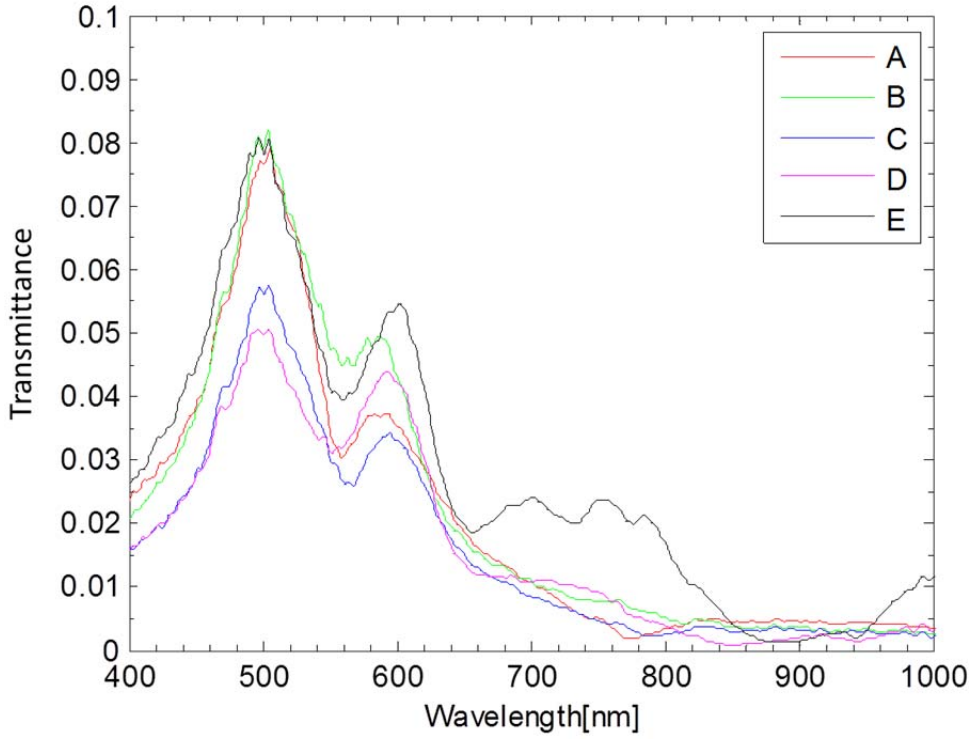

Fig. 4-5　Five transmission spectra of the fabricated SPR fiber probes in air. The probes are the same as those shown in Fig. 4-4.

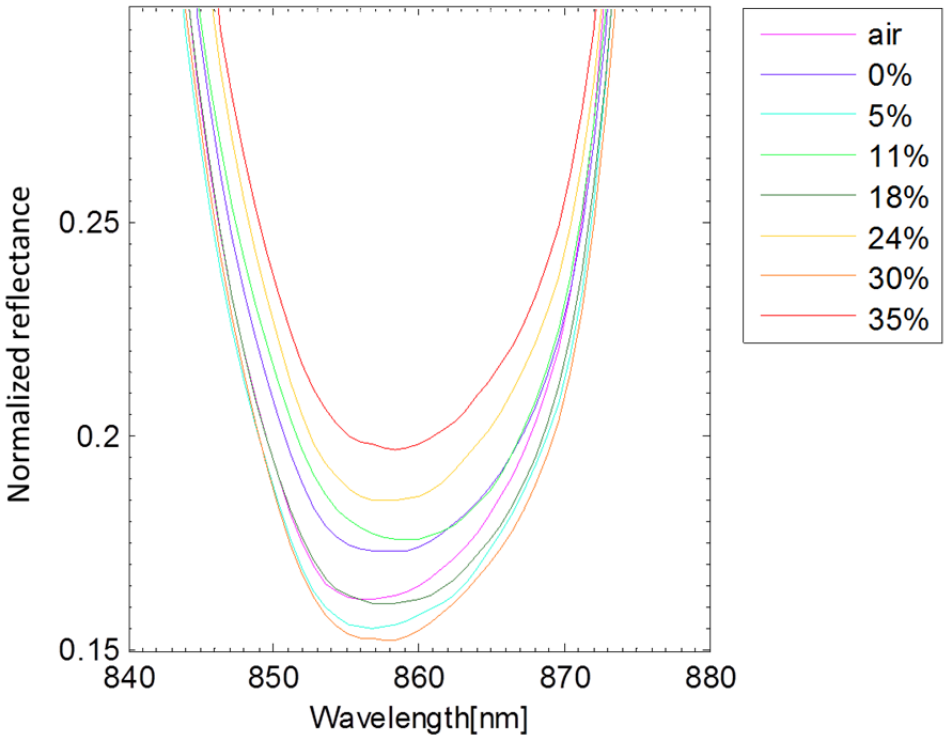

Fig. 4-6 Experimental reflection spectra of the SPR fiber probe A at the resonant dips in air and glucose solutions with concentrations of 0%-35%.

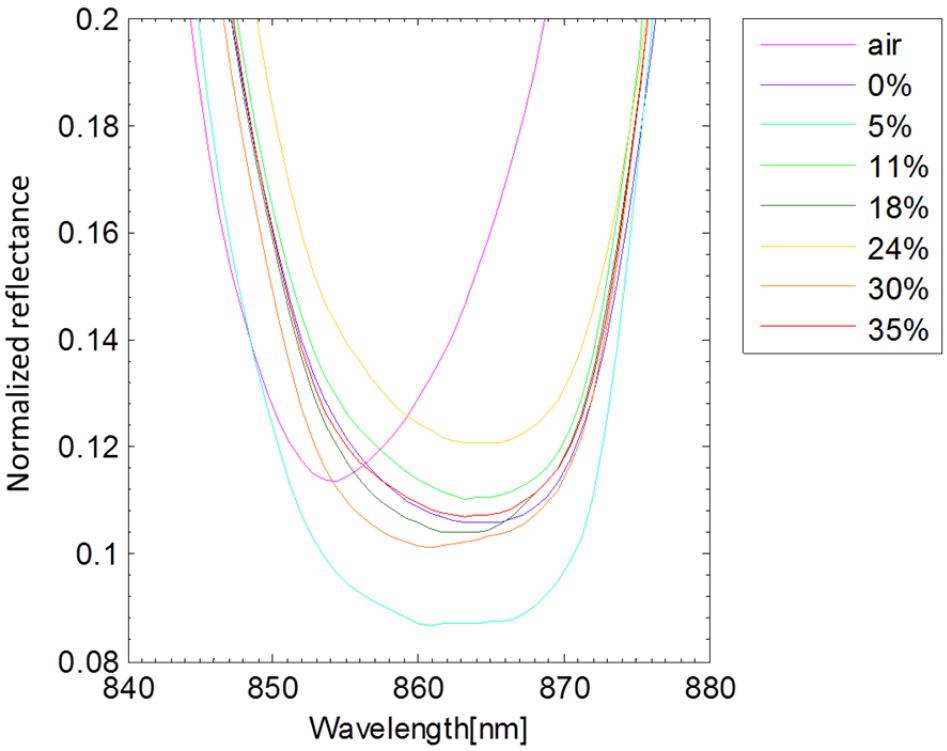

Fig. 4-7 Experimental reflection spectra of the SPR fiber probe C with leaky structures at the resonant dips in air and glucose solutions with concentrations of 0%-35%.

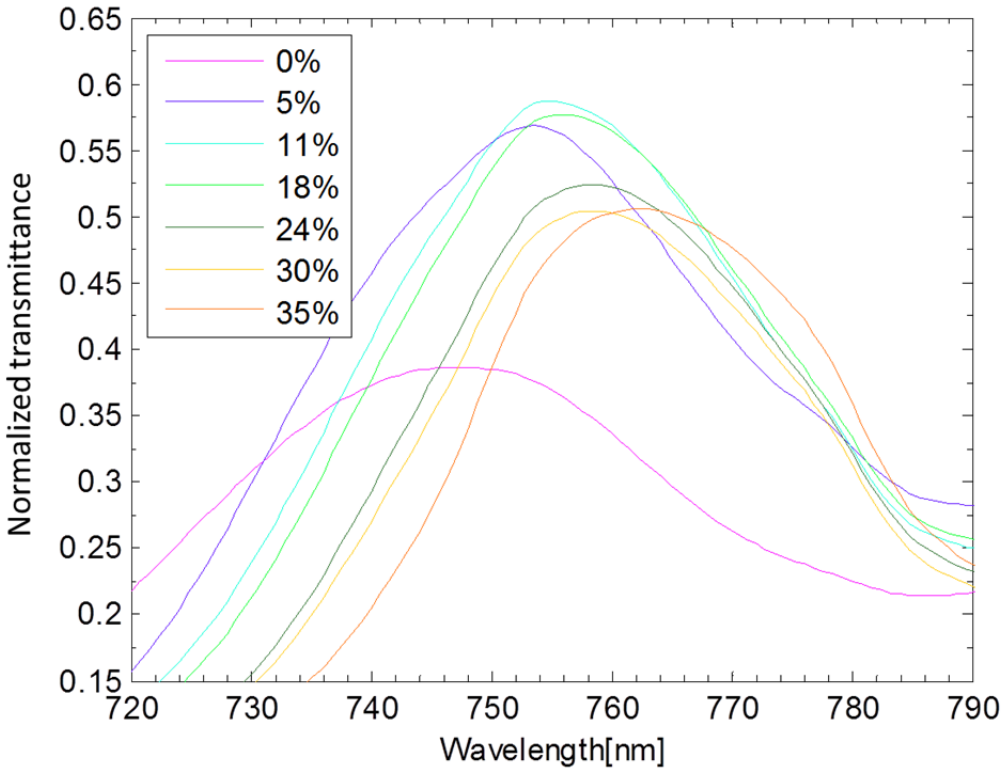

Fig. 4-8 Experimental transmission spectra of the SPR fiber probe D at the resonant peaks in glucose solutions with concentrations of 0%-35%.

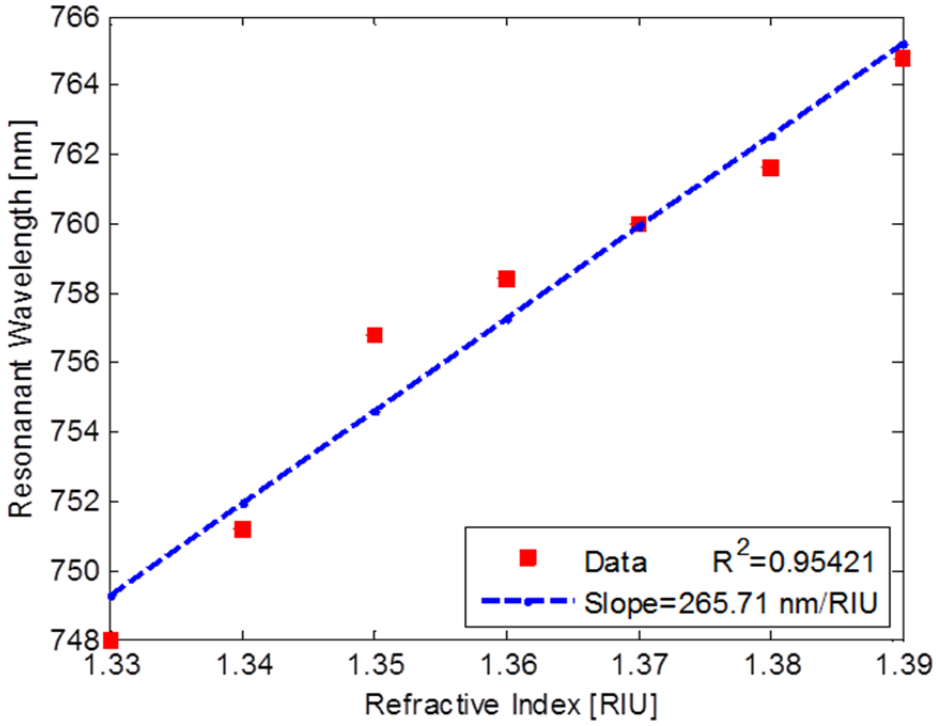

Fig. 4-9 Experimental data of the positions of the resonant peaks in the transmission spectra and a linear fit to the data.

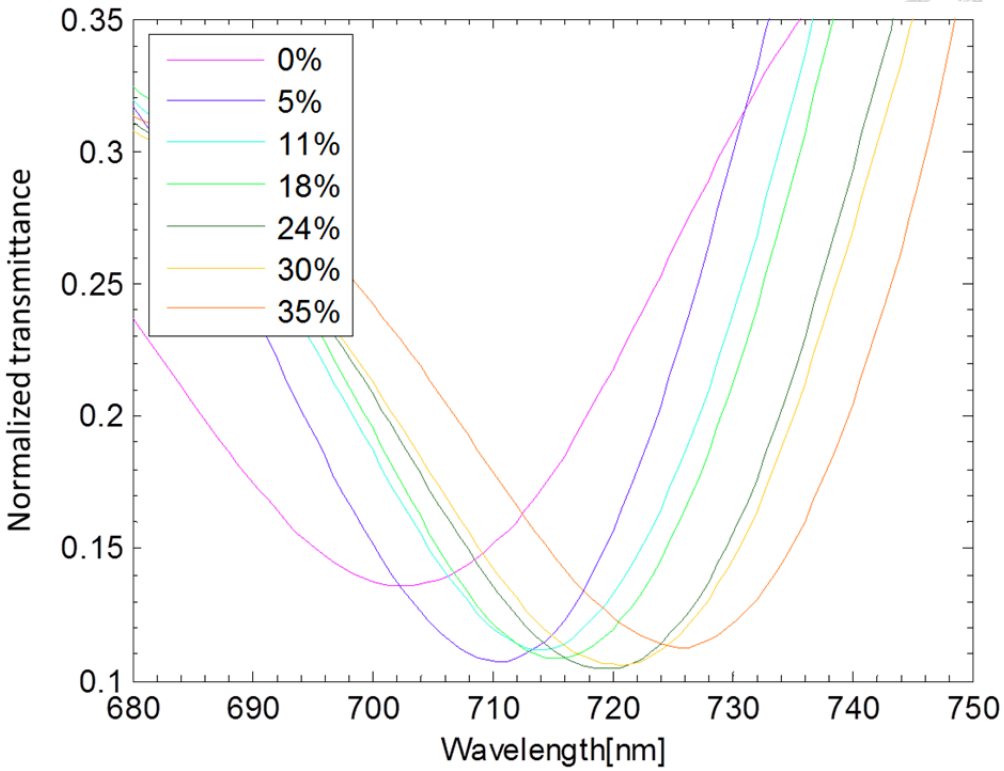

Fig. 4-10 Experimental transmission spectra of the SPR fiber probe D at the dips next to the resonant peaks in glucose solutions with concentrations of 0%-35%.

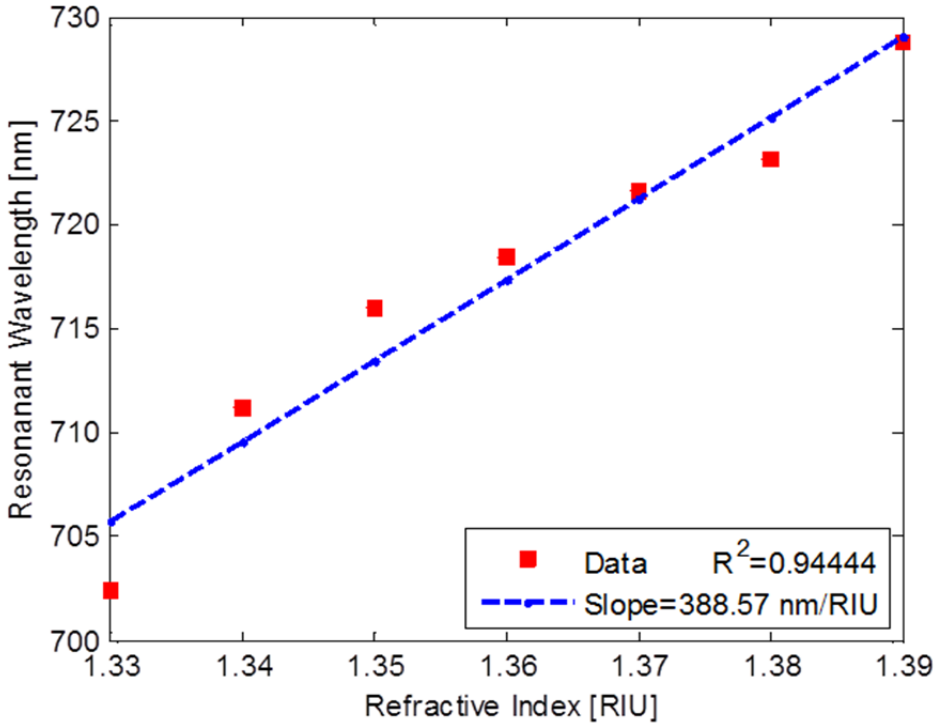

Fig. 4-11 Experimental data of the positions of the dips next to the resonant peaks in the transmission spectra and a linear fit to the data.

4.3 Biosensing with SPR fiber probes

First of all, the gold surface has to be functionalized with linkers and bioreceptors. The protocol of the functionalization and immobilization is shown below and depicted in Fig. 4-12:

(a) The SPR fiber probes are incubated in 11-MUA solutions for 90 minutes to form 11-MUA self-assembled monolayers (SAMs) on the gold surfaces. Then the probes are washed with ethanol.

(b) Prepare a 1:1 mixture of EDC solutions with NHS solutions by volume and incubate the probes in the mixture for 30 minutes. The carboxyl groups of the 11-MUA are activated with NHS in the presence of EDC. Then the probes are washed with PBS solutions.

(c) Finally, the probes are incubated in BSA solutions for 30 minutes. Then the probes are washed with PBS solutions.

The spectrum of each step was recorded and is shown in Fig. 4-13. All the spectra were measured in PBS solutions. The first spectrum from the left showed the resonant peak due to the nanostructures with bare gold surfaces. As the gold surfaces were functionalized with 11-MUA and NHS, the resonant position was shifted to the red. In the end, relative to the spectrum of NHS, a shift of about 0.75 nm caused by the immobilization of BSA was measured.

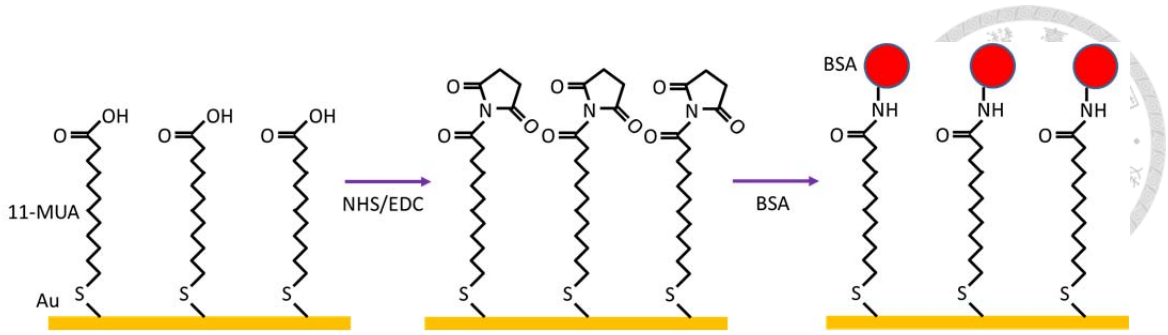

Fig. 4-12 Diagram of the protocol of the functionalization and immobilization.

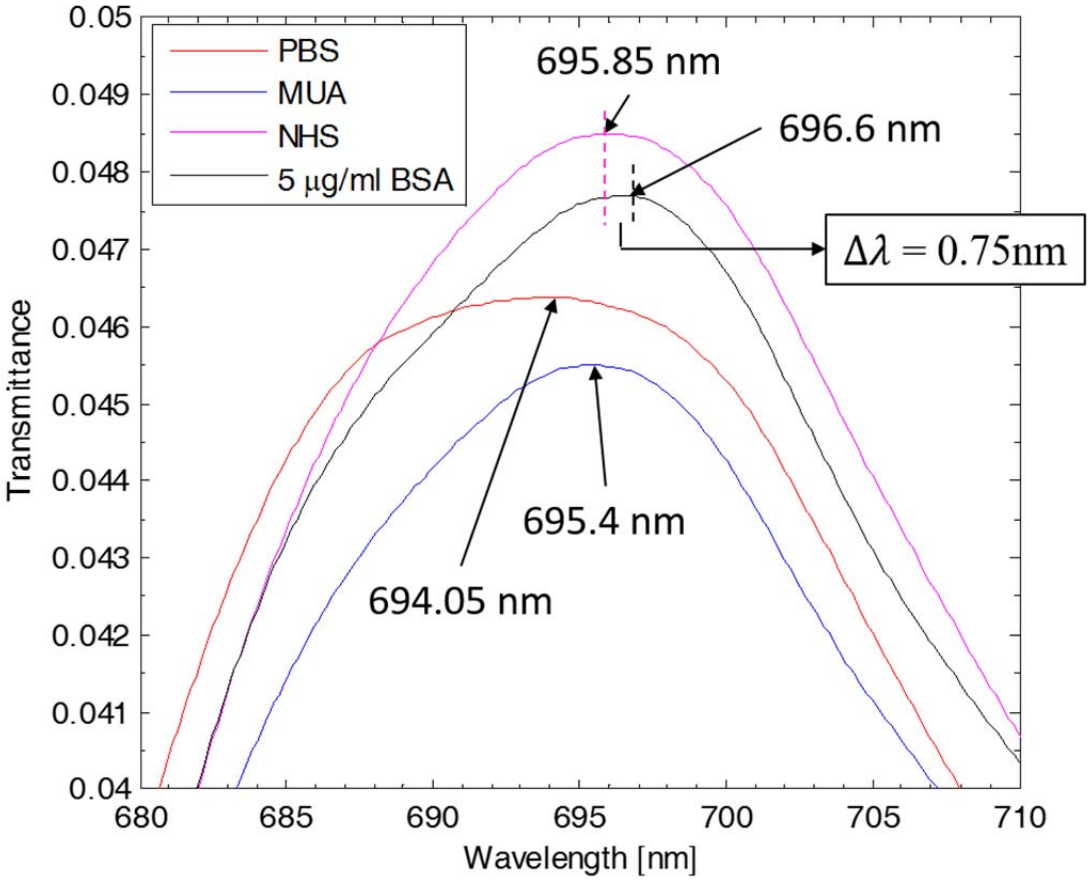

Fig. 4-13 Wavelength shifts of the transmission spectra according to each functionalization or immobilization step.

Chapter 5 Conclusions and Future Work

5.1 Conclusions

In this work, the potential of fast and mass production of SPR fiber probes by applying nTP on a fiber bundle has been demonstrated. The fibers were inserted into an aluminum cylinder to increase the surface area for processing. The nanostructures on the PDMS stamps for nTP were replicated from the PR mold and the original patterns on the mold were defined by two-beam IL. It was found that the nanostructures on the stamps would be unstable if there were some uncured LMW PDMS chains, which were resulted from the insufficient curing time. To extract the LMW chains, two effective methods have been introduced and tested. Although the two methods absolutely removed the LMW chains, the conditions looked not good on the stamps extracted by the hexane solutions. As for the results of extraction by thermal aging, the conditions looked good but the method took a long time. We introduced a skill to accelerate the thermal aging process. Few PDMS was first spin coated on the mold, and then baked. The thin PDMS could absorb the thermal energy more efficiently. Next, the extracted stamps were used in the nTP process on the glass substrates for optimization of the parameters. To lower the surface energy of the stamps, and obtain larger and finer transferred patterns, the pressure, the temperature and the time for imprinting were optimized to be 425 psi, 100℃ and 55 seconds, respectively. The unique 3D structures were verified by SEM. Finally, the optimized nTP was applied on the fiber bundle and we got the gold nanohole array structures with period 506 nm, diameter 261 nm, depth 100 nm and thickness 50 nm.

To study the optical properties of the SPR fiber probes, the simplified model was

simulated by the commercial software, FDTD Solutions and Comsol Multiphysics, which were based on FDTD method and FEM, respectively. The simulated results indicated a sharp resonant dip at about 865 nm in the reflection spectrum and a resonant peak at 580 nm in the transmission spectrum. The electric fields were further examined to prove that the resonant positions were where SPR took place exactly. In the simulation of the performance of the probes in different surroundings, it was found that the resonant dip in the reflection spectrum shifted only if the structures were leak. However, the resonant peak in the transmission spectrum showed a good response to the variations of the surroundings, whether the structures were leak or not.

In the experimental measurements of the characteristics of the fabricated SPR fiber probes, both the measured reflection and transmission spectra quite matched with the simulated results. Repeatability of the spectra of the probes was also presented and the resonant positions could be identified clearly even though there were variations in intensity responses from probe to probe. To study the shift responses to the bulk surroundings, the glucose solutions were used for different RIs and the spectra were smoothed by TMA method. It was found that the resonant dip in the reflection spectrum kept still as predicted in the simulation due to the intact structures. In contrast, the resonant peak in the transmission spectrum shifted to the red obviously and the estimated sensitivity was 265 nm/RIU. In addition, the dip in the transmission spectrum on the left side of the resonant peak was found to be more sensitive and the sensitivity of the dip was estimated to be 388 nm/RIU. As for the biosensing test, the red-shifts of the resonant peaks could be clearly observed during the functionalization and immobilization processes. These results successfully represent the ability to do biosensing researches with the SPR fiber probes.

5.2 Future Work

5.2.1 Fabrication improvement on the fiber bundle

Actually, the replicability of the SPR fiber probes could be improved. The pressure used in the nTP process was still too large and the imprint machine was not stable enough. The pressure should be lowered along with a longer contact time so that the stamp can contact with the substrate gently and uniformly.

As mentioned in Section 3.5 and Section 4.2, the simulated and experimental results showed that the resonant dip in the reflection spectrum could not sense the changes of the surroundings due to the intact structures. However, for practicality, reflection-based system is preferred. Launch of incident light and collection of signals can be realized with only one optical fiber. Therefore, one should put effort into the fabrication of leak 3D or 2D structures. Relatively, it is easier to fabricate 2D structures as depicted in Fig. 1-2 (a). Thus the sidewalls of the stamps should be vertical and the vapor beam should be collimated during the metal deposition process. Grating structures are taken as an example and the simulated spectra for the structures are shown below. In Fig. 5-1, the two resonant positions near 560 nm and 780 nm both can be observed in the reflection and transmission spectra clearly. However, only the resonant position near 560 nm can sense the surroundings as shown in Fig. 5-2 and Fig. 5-3, and an estimated sensitivity is about 435 nm/RIU.

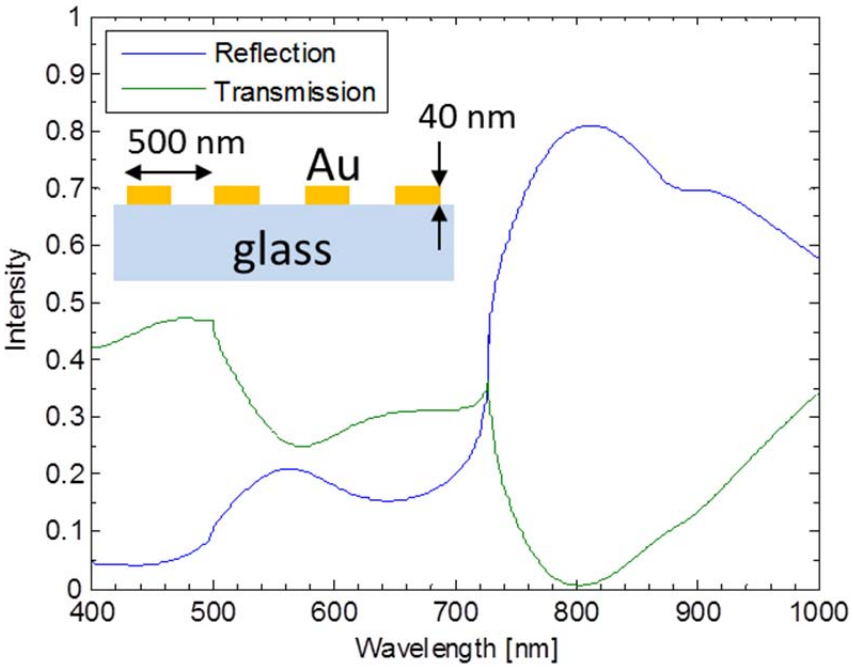

Fig. 5-1 Simulated reflection and transmission spectra for the grating structures of period 500 nm and grating height 40 nm in air as shown in the inset.

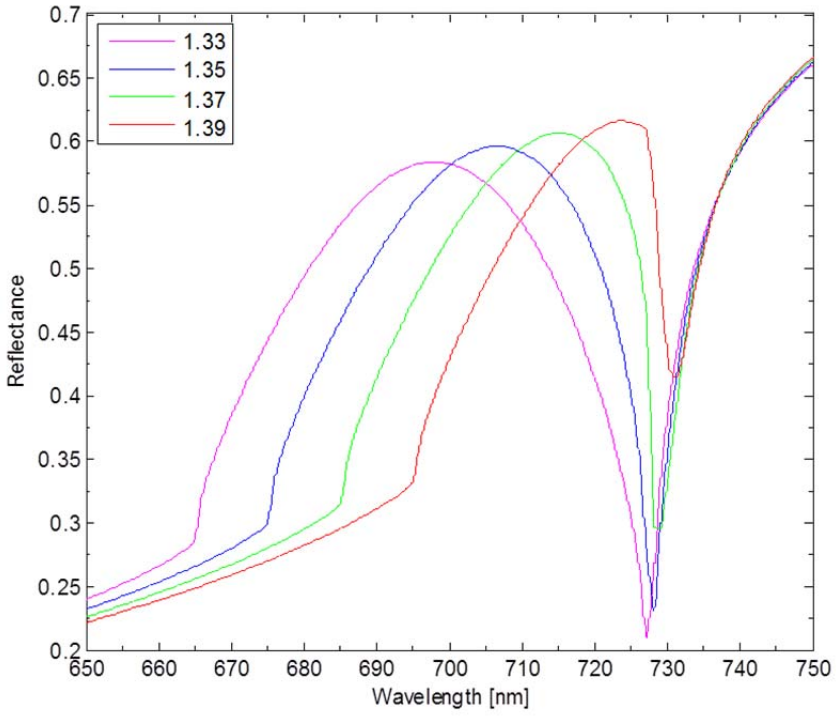

Fig. 5-2 Simulated reflection spectra of the model with surroundings of n_s = 1.33 to 1.39.

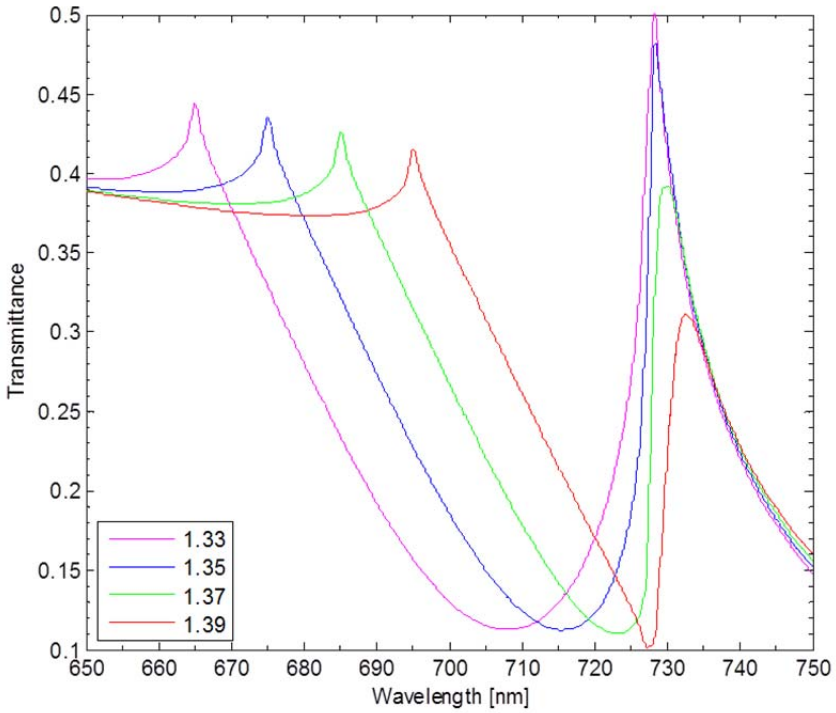

Fig. 5-3 Simulated transmission spectra of the model with surroundings of n_s = 1.33 to 1.39.

5.2.2 Silicon-cored fiber based SPR fiber sensors

Recently, the combination of semiconductor materials with fiber optics has become one of the emerging research topics. We have the ability to produce silicon-cored fibers with high quality by vertical-drawing [46]. Therefore, SPR sensors based on the silicon-cored fibers operating in the IR range can be realized. Actually, such silicon-based schemes have the advantages of sensor miniaturization and integration, which are attributed to the well-developed semiconductor fabrication processes [47-49]. On the other hand, silicon is transparent in the range, 1.2-10 μm, and it shows an essentially different behavior of dispersion compared with that of glass [47, 48]. As shown in Fig. 5-4, silicon prisms provide narrower reflectivity curves and a reverse

behavior in wavelengths for its high RI and unique dispersion. Besides, the probe depth can reach 1-2 μm while operating in IR so relatively large objects can be sensed [47]. According to those described above, it is believed that the silicon-cored fiber based SPR sensors with IR light can be a novel device for the improvement of current visible based SPR sensors.

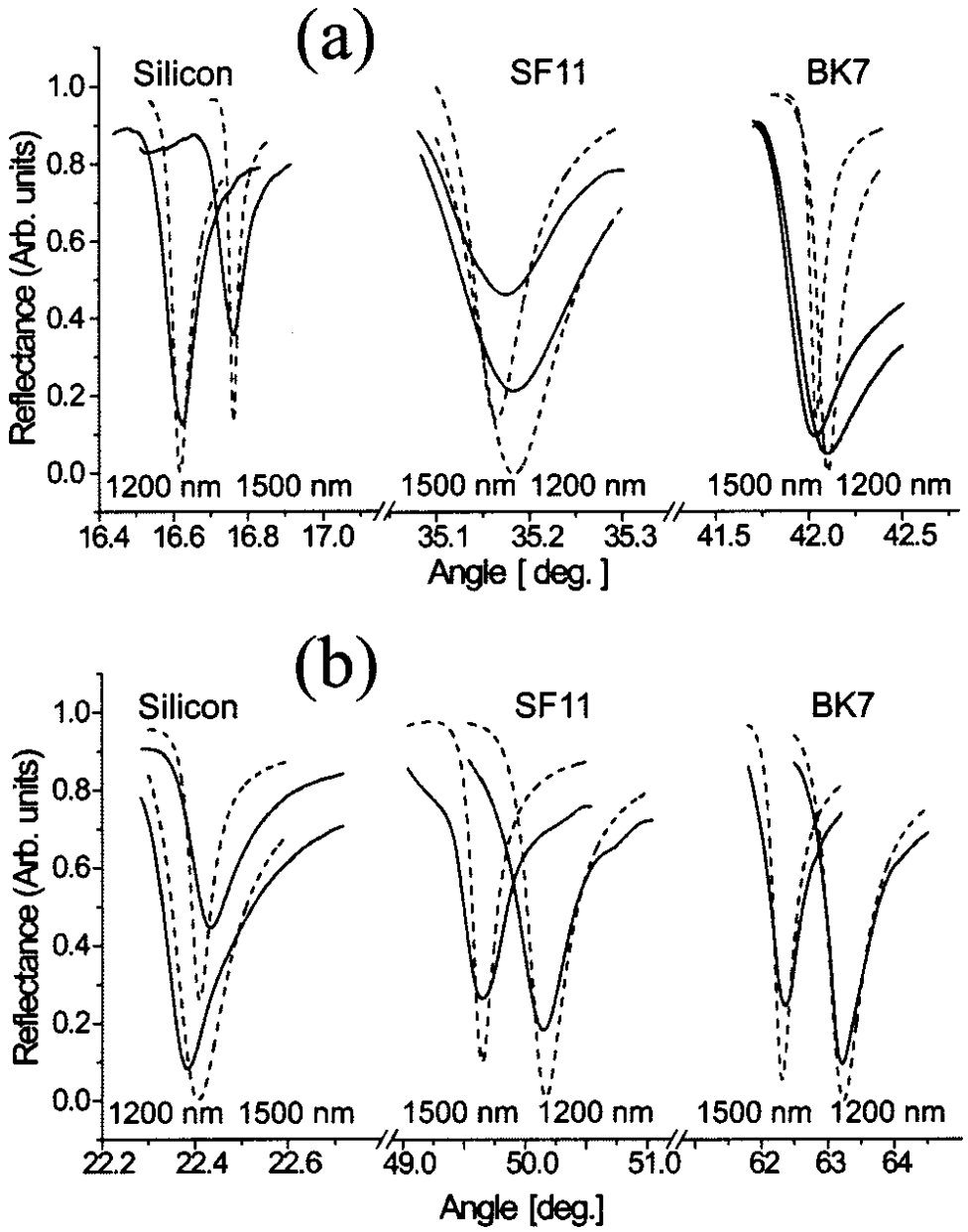

Fig. 5-4 The calculated (dashed lines) and experimental (solid lines) angular reflectivity curves for prisms from BK7 and SF11 glasses and silicon in the configuration of (a) gases and (b) aqueous sensing medium [47].

References

1. J. Homola, S. S. Yee, and G. Gauglitz, *Surface plasmon resonance sensors: review.* Sensors and Actuators B: Chemical, 1999. **54**(1-2): p. 3-15.
2. A. K. Sharma, R. Jha, and B. D. Gupta, *Fiber-optic sensors based on surface plasmon resonance: a comprehensive review.* IEEE Sensors Journal, 2007. 7(8): p. 1118-1129.
3. G. Kostovski, P. Stoddart, and A. Mitchell, *The optical fiber tip: an inherently light-coupled microscopic platform for micro- and nanotechnologies.* Advanced Materials, 2014. **26**(23): p. 3798-3820.
4. X. Yang, N. Ileri, C. C. Larson, T. C. Carlson, J. A. Britten, A. S. P. Chang, C. Gu, and T. C. Bond, *Nanopillar array on a fiber facet for highly sensitive surface-enhanced Raman scattering.* Optics Express, 2012. **20**(22): p. 24819-24826.
5. R. C. Jorgenson, and S. S. Yee, *A fiber-optic chemical sensor based on surface plasmon resonance.* Sensors and Actuators B: Chemical, 1993. **12**(3): p. 213-220.
6. A. V. Sayats, I. I. Smolyaninov, and A. A. Maradudin, *Nano-optics of surface plasmon polaritons.* Physics Reports, 2005. **408**(3-4): p. 131-314.
7. Z. Chen, Z. Dai, N. Chen, S. Liu, F. Pang, B. Lu, and T. Wang, *Gold nanoparticles-modified tapered fiber nanoprobe for remote SERS detection.* IEEE Photonics Technology Letters, 2014. **26**(8): p. 777-780.
8. W. Ding, S. R. Andrews, T. A. Berks, and S. A. Maier, *Modal coupling in fiber tapers decorated with metallic surface gratings.* Optics Letters, 2006. **31**(17): p. 2556-2558.

9. A. Dhawan, M. D. Gerhold, and J. F. Muth, *Plasmonic structures based on subwavelength apertures for chemical and biological sensing applications*. IEEE Sensors Journal, 2008. **8**(6): p. 942-950.

10. A. Dhawan, J. F. Muth, D. N. Leonard, M. D. Gerhold, J. Gleeson, T. Vol-Dinh, and P. E. Russell, *Focused ion beam fabrication of metallic nanostructures on end faces of optical fibers for chemical sensing applications.* Journal of Vacuum Science & Technology B, 2008. **26**(6): p. 2168-2173.

11. S. Scheerlinck, D. Taillaert, D. V. Thourhout, and R. Baets, *Flexible metal grating based optical fiber probe for photonic integrated circuits.* Applied Physics Letters, 2008. **92**(3): p. 031104.

12. E. G. Johnson, J. Stack, T. J. Suleski, C. Koehler, and W. Delaney, *Fabrication of micro optics on coreless fiber segments.* Applied Optics, 2003. **42**(5): p. 785-791.

13. C. T. Tseng, *Fabrication and application of binary phase grating on a fiber end by utilizing interference lithography*, in Graduate Institute of Photonics and Optoelectronics2011, National Taiwan University: Taipei.

14. S. J. Lin, *Building up two exposure systems of optical fiber interference lithography to make micro polarizers*, in Graduate Institute of Photonics and Optoelectronics2013, National Taiwan University: Taipei.

15. J. W. Jeong, S. R. Yang, Y. H. Hur, S. W. Kim, K. M. Baek, S. Yim, H. I. Jang, J. H. Park, S. Y. Lee, C. O. Park, and Y. S. Jung, *High-resolution nanotransfer printing applicable to diverse surfaces via interface-targeted adhesion switching.* Nature Communications, 2014. **5**(11): p. 5387.

16. J. Zaumseil, M. A. Meitl, J. W. P. Hsu, B. R. Acharya, K. W. Baldwin, Y. L. Loo, and J. A. Rogers, *Three-dimensional and multilayer nanostructures formed by*

nanotransfer printing. Nano Letters, 2003. **3**(9): 1223-1227.

17. E. Menard, L. Bilhaut, J. Zaumseil, and J. A. Rogers, *Improved surface chemistries, thin film deposition techniques, and stamp designs for nanotransfer printing*. Langmuir, 2004. **20**(16): 6871-6878.

18. A. R. Camara, P. M. P. Gouvêa, A. C. M. S. Dias, A. M. B. Braga, R. F. Dutra, R. E. de Araujo, and I. C. S. Carvalho, *Dengue immunoassay with an LSPR fiber optic sensor.* Optics Express, 2013. **21**(22): p. 27023-27031.

19. Y. Lin, Y. Zou, and R. G. Lindquist, *A reflection-based localized surface plasmon resonance fiber-optic probe for biochemical sensing.* Biomedical Optics Express, 2011. **2**(3): p. 478-484.

20. S. Choi, K. R. Kim, K. Oh, C. M. Chun, M. J. Kim, S. J. Yoo, and D. Y. Kim, *Interferometric inscription of surface relief gratings on optical fiber using azo polymer film*. Applied Physics Letters, 2003. **83**(6): p. 1080-1082.

21. S. Kuwayama, and Y. Harada, *Acid-soluble glass for making flexible optical fiber bundle*, U.S. Patent 4 460 696, July 17,1984.

22. C. H. Chiang, *Fabrication of subwavelength dual structures on silicon substrates with anti-reflection and low sliding angles*, in Graduate Institute of Photonics and Optoelectronics2010, National Taiwan University: Taipei.

23. Y. P. Chen, *Stitching submicron periodic patterns over a planar substrate and a roller by utilizing step-and-align interference lithography*, in Graduate Institute of Photonics and Optoelectronics2011, National Taiwan University: Taipei.

24. X. Fang, *Fabrication of nano metal meshes by nanoimprint lithography for organic electronics device applications*, in Graduate Institute of Photonics and Optoelectronics2015, National Taiwan University: Taipei.

25. E. Delamarche, H. Schmid, B. Michel, and H. Biebuyck, *Stability of molded*

polydimethylsiloxane microstructures. Advanced Materials, 1997. **9**(9): p. 741-746.

26. A. Galliano, S. Bistac, and J. Schultz, *Adhesion and friction of PDMS networks: molecular weight effects*. Journal of Colloid and Interface Science, 2003. **265**(2): p. 372-379.

27. D. J. Graham, D. D. Price, and B. D. Ratner, *Solution assembled and microcontact printed monolayers of dodecanethiol on gold: a multivariate exploration of chemistry and contamination*. Langmuir, 2002. **18**(5): p. 1518-1527.

28. Y. Meng, Z. B. Li, X. Chen, J. P. Chen, *Reducing wrinkles and cracks of metal films on PDMS substrate by hexane extraction and oxygen plasma etching.* Microelectronic Engineering, 2014. **130**: p. 8-12.

29. J. A. Vickers, M. M. Caulum, and C. S. Henry, *Generation of hydrophilic poly(dimethylsiloxane) for high-performance microchip electrophoresis*. Analytical Chemistry, 2006. **78**(21): p. 7446-7452.

30. J. N. Lee, C. Park, and G. M. Whitesides, *Solvent compatibility of poly(dimethylsiloxane)-based microfluidic devices.* Analytical Chemistry, 2003. **75**(23): p. 6544-6554.

31. D. T. Eddington, J. P. Puccinelli, and D. J. Beebe, *Thermal aging and reduced hydrophobic recovery of polydimethylsiloxane.* Sensors and Actuators B: Chemical, 2006. **114**(1): p. 170-172.

32. B. B. Sauer, and G. T. Dee, *Molecular weight and temperature dependence of polymer surface tension: comparison of experiment with theory.* Macromolecules, 1991. **24**(8): p. 2124-2126.

33. K. D. Bartle, B. W. Wright, and M. L. Lee, *Characterization of glass, quartz,*

and fused silica capillary column surfaces from contact-angle measurements. Chromatographia, 1981. **14**(7): p. 387-397.

34. G. L. Sma, *Surface-energy determinations of tin oxide-coated soda-lime-silica glass.* Journal of the American Ceramic Society, 1988. **71**(4): C-217-C-219.

35. Y. C. Yang, and P. R. Yoon, *Determination of dispersive properties of silicas by inverse gas chromatography: variation with surface treatment.* Materials Transactions, 2007. **48**(6): p. 1548-1553.

36. S. A. Maier, *Plasmonics: fundamentals and applications.* Springer, 2007.

37. A. D. Rakić, A. B. Djurišić, J. M. Elazar, and M. L. Majewski, *Optical properties of metallic films for vertical-cavity optoelectronic devices.* Applied Optics, 1998. **37**(22): p. 5271-5283.

38. K. S. Yee, *Numerical solution of initial boundary value problems involving maxwell's equations in isotropic media.* IEEE Transactions on Antennas and Propagation, 1966. **14**(3): p. 302-307.

39. H. Nguyen, G. W. Baxter, S. F. Collins, F. Sidiroglou, A. Roberts, and T. J. Davis, *Modeling of gold circular sub-wavelength apertures on a fiber endface for refractive index sensing.* Photonic Sensors, 2012. **2**(3): p. 271-276.

40. J. Martin, J. Proust, D. Gérard, J. L. Bijeon, J. Plain, and P. Royer, *Ultra-sensitive plasmonic nanosensors for biochemical detection.* Proc. of SPIE, 2011. **12**(29): p. 79110T-1-79110T-6.

41. Y. Lin, Y. Zou, and R. G. Lindquist, *A reflection-based localized surface plasmon resonance fiber-optic probe for biochemical sensing.* Biomedical Optics Express, 2011. **2**(3): p. 478-484.

42. D. R. Lide, *CRC handbook of chemistry and physics.* CRC Press, 2005.

43. J. P. Berenger, *A perfectly matched layer for the absorption of electromagnetic waves.* Journal of Computational Physics, 1994. **144**(2): p. 185-200.

44. K. Feng, *Difference scheme based on variational principle.* Journal of applied and computational Mathematics,1965. **2**(4): p. 238-262.

45. J. M. McMahon, J. Henzie, T. W. Odom, G. C. Schatz, and S. K. Gray, *Tailoring the sensing capabilities of nanohole arrays in gold films with Rayleigh anomalysurface plasmon polaritons.* Optics Express, 2007. **15**(26): p. 18119-18129.

46. Y. B. Huang, *Fabrication of Schottky photodetector by using Si-cored fibers*, in Graduate Institute of Photonics and Optoelectronics2015, National Taiwan University: Taipei.

47. S. Patskovsky, A. V. Kabashin, and M. Meunier, *Properties and sensing characteristics of surfaceplasmon resonance in infrared light.* Journal of the Optical Society of America A, 2003. **20**(8): p. 1644-1650.

48. S. Patskovsky, A. V. Kabashin, M. Meunier, and J. H. T. Luong, *Silicon-based surface plasmon resonance sensing with two surface plasmon polariton modes.* Applied Optics, 2003. **42**(34): p. 6905-6909.

49. T. Kan, N. Tsujiuchi, E. Iwase, K. Matsumoto, and I. Shimoyama, *Planar near-infrared surface plasmon resonance sensor with Si prism and grating coupler.* Sensors and Actuators B: Chemical, 2010. **144**(1): p. 295-300.